Collisional Properties of Metastable Calcium Atoms in a Miniaturized Ioffe Trap

DISSERTATION
zur Erlangung des Doktorgrades
des Fachbereichs Physik
der Universität Hamburg

vorgelegt von
Dirk Hansen
aus Bad Dürkheim

Hamburg
2006

Gutachter der Dissertation	Prof. Dr. Andreas Hemmerich
	Prof. Dr. Fritz Riehle
Gutachter der Disputation	Prof. Dr. Andreas Hemmerich
	Prof. Dr. Werner Neuhauser
Datum der Disputation	24. Februar 2006
Vorsitzender des Prüfungsausschusses	Dr. Klaus Petermann
Vorsitzender des Promotionsausschusses	Prof. Dr. Günther Huber
Dekan des Fachbereichs Physik	Prof. Dr. Günther Huber

Abstract

This thesis presents experiments examining the collisional properties of cold metastable calcium atoms in a miniaturized magnetic trap. The elastic and inelastic collision rates are measured and compared to recent theoretical predictions [56]. According to the theory, the collisions between metastable alkaline-earth atoms in a magnetic field are dominated by partial waves with large angular momenta even at low temperatures. Inelastic collision rates are predicted to be unusually large, even exceeding the elastic rates below 10 µK. The experiments clearly confirm the general character of the theory and inelastic rates were found to be even one order of magnitude above the theory. As a consequence, evaporative cooling can be ruled out as a means to reach Bose-Einstein condensation of metastable Ca in a magnetic trap. In the experiment, atoms from a calcium oven are precooled in a Zeeman slower and loaded into a magneto-optical trap (MOT) operating on the ground state transition $^1S_0 \rightarrow {}^1P_1$ at 423 nm. The metastable (4s4p) $^3P_2$ level is populated through a decay channel originating from $^1P_1$ and captured in a second MOT at 1978 nm. Subsequently, the atoms are magnetically stored and transfered to a miniaturized Ioffe trap. Trap loss and reequilibration measurements of the aspect ratio of the sample yield the inelastic and elastic collision rates.

Zusammenfassung

In dieser Dissertation werden Experimente vorgestellt, die die Eigenschaften von kalten Stößen zwischen metastabilen Kalziumatomen untersuchen, die in einer miniaturisierten Magnetfalle gespeichert sind. Die elastischen und inelastischen Stoßraten wurden gemessen und mit neuen theoretischen Vorhersagen verglichen [56]. Laut Theorie werden die Stöße zwischen metastabilen Erdalkaliatomen in Magnetfeldern bei tiefen Temperaturen durch Partialwellen dominiert, die große Drehimpulse besitzen. Es werden ungewöhnlich große inelastische Streuraten vorhergesagt, die bei Temperaturen unter 10 µK die elastischen Streuraten sogar übertreffen. Die Experimente belegen klar die generelle Vorhersage der Theorie; die gemessenen inelastischen Streuraten liegen sogar noch eine Größenordnung über der Theorie. Die Möglichkeit, in einer Magnetfalle ein Bose-Einstein Kondensat mit metastabilen Kalziumatomen durch evaporatives Kühlen zu erzeugen kann somit ausgeschlossen werden. Im Experiment werden aus einem Kalziumofen kommende Atome in einem Zeeman Kühler abgebremst und in einer magneto-optischen Falle (MOT) gefangen, die den Grundzustandsübergang $^1S_0 \rightarrow {}^1P_1$ bei 423 nm benutzt. Über einen Zerfallskanal aus dem $^1P_1$ Niveau wird das metastabile (4s4p) $^3P_2$ Niveau bevölkert und in einer zweiten MOT gefangen. Danach werden die Atome magnetisch gespeichert und in eine miniaturisierte Ioffe Falle transferiert. Die inelastischen und elastischen Streuraten werden dann über Lebensdauermessungen der Falle bzw. über Relaxationsmessungen des Aspektverhältnisses des Ensembles bestimmt.

Contents

1 Introduction

Thirty years ago, a visionary article by Hänsch and Schawlow first voiced the idea that light alone could be used to cool neutral atomic ensembles to unprecedented temperature ranges [49]. It had been a well established fact that light exerts forces on objects that scatter or reflect it and Ashkin had proposed an apparatus that could trap neutral atoms on stable circular orbits [5]. Hänsch and Schawlow's idea, however, was new and should lead to spectacular new experiments and insight into physics in the decades to come. They realized that with laser light that is slightly red detuned to the optical resonance frequency, atomic gases could be cooled by many orders of magnitude in a matter of milliseconds and within path lengths on the order of centimeters. The idea of laser cooling was introduced independently by Wineland and Dehmelt for ions [98] and the first observations of laser cooling were reported in 1978 [69, 99]. The development of sophisticated laser systems and spectroscopy techniques, along with a technological advancement in ultra high vacuum technology then paved the way for the physics of cold atoms.

Efficient cooling was realized in an optical molasses where counter-propagating laser beams restrict the atoms to diffusive motion. The laser beams can be applied in all three spatial dimensions to generate samples at very low temperatures [19]. Spatial trapping by radiation pressure, however, is impossible because the force does not depend on the position of the atoms. In 1985 then, magnetic trapping of neutral atoms was first reported [65], followed by storing atoms in an optical dipole trap [18]. In an approach to simultaneously cool and trap particles, a configuration was proposed where the optical molasses is superimposed on

a magnetic quadrupole field, thereby creating a force that is both dissipative and dependent upon the position of the atom. This magneto-optic trap (MOT) for neutral particles was first realized in 1987 and used to trap 10^7 Na atoms at a temperature of less than a mK [79].

Doppler cooling relies on the principle that for a red detuned beam, the atoms are more likely to absorb light if they move against the propagation direction of the light; the Doppler effect compensates the difference between the frequency of the light and the resonance frequency of the atom. If the atom moves along the direction of light propagation, the Doppler effect tunes the atom further out of resonance. Hence, momentum transfer occurs primarily opposite to the movement of the atom, slowing it down in the process. Any photon that is absorbed by the atom is reemitted but since the reemission is spatially isotropic, the effect cancels except for a residual temperature, the Doppler temperature, that sets a lower limit to the Doppler cooling process.

The mechanism of Doppler cooling was well understood by then [6, 20] and it came as a surprise when temperatures lower than the Doppler limit [58] were reported. It turned out that for optical transitions where the ground state exhibits a magnetic substructure, sub-Doppler mechanisms exist that could cool atoms down to temperatures associated with the recoil momentum of a single photon [22, 24]. The development of laser cooling and trapping techniques was awarded with the Nobel prize for Chu, Cohen-Tannoudji, and Phillips in 1997 [17, 23, 73].

In 1995, researchers at NIST [2] and MIT [25] succeeded in making a Bose-Einstein condensate (BEC). 70 years earlier, Bose and Einstein [13, 37] had predicted that if a gas of trapped bosonic particles is cooled to low enough temperatures, the energetic ground state should become populated by a macroscopic number of particles. The de Broglie wavelength of a ground state particle can be even larger than the 10 µm scale and condensates can be populated by up to 10^9 atoms such that the quantum behavior and the matter wave character of the atoms can be easily observed in experiments. To reach BEC, though, laser cooling methods are not sufficient, and one had to add evaporative cooling as the final step. In evaporative cooling, the hottest atoms from the sample are selectively removed and the remaining atoms are left to reequilibrate, thereby reducing their temperature. Very similar to the process by which a cup of hot tea cools, this method very efficiently reduces the temperature; typical condensate temperatures are on the order of 100 nK. The achievement of BEC earned the Nobel prize in 2001 for Cornell, Ketterle, and Wieman.

Further developments in laser cooling led to the realization of a number of other interesting systems, of which I shall only mention a few. Fermions were also cooled to the quantum degenerate regime, the "Fermi sea", where they occupy only the lowest lying levels of the trap [28]. A quantum phase transition between a superfluid and a Mott insulator phase was observed in a system of a BEC that is stored in a three-dimensional lattice potential [42] and the crossover between the BCS superfluidity and a BEC of molecules has been explored [40].

Another exciting area is the investigation of quantized vortices as a signature of superfluidity in a BEC [62].

Despite the huge success of laser cooling and trapping experiments in the last two decades, the number of elements that are used is only now more rapidly increasing. The elements that are condensed, e.g., is limited to hydrogen and the alkali elements Li, Na, K, Rb, Cs, and, apart from the first column in the periodic table, *He, Yb, and Cr (cf. [3], and, for more recent developments, [43, 90, 95]). Laser cooling experiments are under way with a number of other species, with considerable attention spent on the alkaline-earths Mg [74], Ca [27, 71], and Sr [60, 89]. One of the reasons for the somewhat slow expansion of the group of laser-cooled atoms is the need for more sophisticated laser systems to drive the optical transitions. The wavelengths for Rb, the most extensively studied element in laser cooling, can mostly be addressed by easy-to-build low-cost diode lasers in the near infrared range, whereas the principal fluorescence lines in the alkaline-earths lie in the blue and UV part of the spectrum and their generation requires more complex laser technology.

There is a lot of exciting new physics to be done with alkaline-earth metals and I want to point out a few lines of research pertaining to calcium. One of the main goals is reaching the quantum degenerate regime [16]. Calcium is a system with the potential of realizing a truly continuous source of coherent matter. Similar to the principle of a laser, it could be used as an inverted medium for matter wave amplification. It possesses two stable energy levels, the singlet $^1S_0$ ground state and the metastable triplet $^3P_2$ state that can both be addressed by laser radiation. The triplet state can be filled by a high flux of precooled atoms, which can then be optically pumped via an intermediate energy level to the ground state. At a sufficiently high flux, it is proposed that a macroscopic $^1S_0$ population emerges in the ground state of, e.g., an optical trap [44, 87]. In addition to the formation of a condensate in the ground state, a BEC in the metastable state with its large magnetic moment would contribute to the study of dilute polar gases in which dipole-dipole interactions between particles become important [33, 88].

A second area of interest is the use of calcium and other alkaline-earths in time metrology [31, 94]. Currently, the second is defined through a hyperfine structure transition in Cs at 9.2 GHz. The transition is probed in a Cs fountain clock on cold ensembles of about 1 µK and the present level of inaccuracy is on the order of 10^{-15}. The accuracy of the clock is mainly limited by uncertainties in the ambient blackbody radiation and the gravitational potential at the location of the clock as well as by frequency changing collisions. Technical advances, as, e.g., placing a clock in orbit might increase the accuracy by another order of magnitude. A bigger potential for improvement, however, lies in switching from microwave frequencies to optical transitions that are typically in the 10^{15} Hz range. Basically, a higher accuracy can be achieved if the smallest unit that is counted (i.e., one oscillation) is made smaller. Measuring optical frequencies, however, is a very difficult task and has only in the past few years become

possible through a series of major technological improvements. Cold atomic ensembles are a prerequisite since the Doppler shift is greatly reduced. The optical transition chosen has to be very narrow to minimize the uncertainty in the oscillation frequency. To probe such a transition, highly refined laser stabilization techniques have to be available to generate laser light with a linewidth smaller than the transition frequency. Finally, the frequency of a laser that is stabilized to an optical transition has to be counted. A major breakthrough came with the development of the femtosecond laser frequency comb, an invention that was honored with the Nobel prize in 2005 for Hänsch and Hall. (The other half of the prize in 2005 went to Glauber for "his contribution to the quantum theory of optical coherence".)

Calcium is a prime candidate for the realization of an optical frequency standard. Due to its two valence electrons, it exhibits singlet and triplet energy levels with strong fluorescence lines among the singlet system and narrow intercombination lines between the singlet and triplet systems. Its ground state transition $^1S_0 \rightarrow {}^1P_1$ is well suited for efficiently slowing and trapping a large number of atoms, whereas the intercombination transition $^1S_0 \rightarrow {}^3P_1$ at 657 nm with a linewidth of 382 Hz (cf. Appendix B) serves as the balance wheel for a clock. Successful implementation of a frequency standard with Ca has been reported by [27, 93]. When performing spectroscopy on the ensemble, the atoms have to be released from the trap because trapping fields can cause undesirable shifts in the measured frequency. This can lead to uncertainties caused by the Doppler effect and also the interaction time between light and atom is reduced. A possible solution to this problem could be trapping the atoms in an optical lattice potential. If the trapping wavelength is wisely chosen ("magic wavelength"), the potential shifts for both energy levels of the transition are equal, thus resulting in an undisturbed transition frequency. Another advantage of using an ensemble of neutral atoms for spectroscopy is the good signal-to-noise ratio. Ions in the ground state of a trap are also potential candidates for a frequency standard, however, the S/N ratio is not as good here.

A third area of research, which is also the topic of this thesis, is the investigation of cold collision processes. Interactions between particles play a major role in the behavior of the cloud and can be a limiting factor in the feasibility of evaporative cooling. The ensembles produced by laser cooling are extremely cold and the traps used for storing the atoms are often not much deeper than the temperature of the atoms at hand. Inelastic collisions can change the internal state of an atom and the energy can be released into an external degree of freedom, thereby heating the ensemble and causing trap loss. Elastic collisions are needed for the rethermalization of the sample during an evaporation process, a high elastic collision rate allows a small evaporation time. Alkaline-earth metals are an ideal test ground for theories on cold collisions. Due to the absence of hyperfine structure, the theoretical description is greatly reduced compared to the alkalis, i.e., the low number of collisional channels allows modelingS the process. The collisional properties of alkaline-earth atoms were recently explored in a few ground-breaking articles [30, 56, 83].

The authors of [56] present a calculation of the elastic and inelastic scattering rates between two cold metastable alkaline-earth atoms in an external magnetic field. They consider the case of low initial relative kinetic energy ($< 100\,\mu K$) and restrict the treatment to the s-wave entrance channel. Higher order partial waves are considered in the description as exit channels. The calculations show that, even at these low energies, the cold collision process is dominated by high order angular momenta with $L > 6$. Adiabatic potential curves for two spin-polarized atoms in the $m_J = +2$ state, e.g., show a pronounced avoided crossing with a potential curve corresponding to two atoms in the $m_J = +2$ and $m_J = +1$ state at an internuclear distance of about 100 Bohr radii. In other words, for two colliding spin-polarized atoms, there is a high transition probability for one atom towards a lower Zeeman sublevel. This behavior can be understood by the strong anisotropy of the interaction potential. As two atoms approach, they experience strong anisotropic forces that can cause one atom to change its state of polarization. Atoms that undergo such a process are eventually lost from the trap.

Apart from a qualitative analysis of the collision process, the authors calculate the elastic and inelastic scattering rates for two spin-polarized atoms in the $m_J = +2$ state. For calcium, the predicted elastic rate exceeds the inelastic rate by almost an order of magnitude at a relative incident energy of 1 mK. Both rates are roughly equal at about $10\,\mu K$ and the elastic rate is even lower than the inelastic one for energies below $10\,\mu K$. As a consequence, it is predicted that evaporative cooling, which requires an elastic rate much larger than the inelastic rate, will not work for magnetically trapped metastable calcium atoms.

In this thesis, I present the first experimental data that can be compared to the theoretical predictions. Metastable calcium atoms in the $^3P_2$ state are loaded into a miniaturized magnetic trap. Spin-polarization in the $m_J = +2$ state is achieved by optical pumping during a 1-dim Doppler cooling stage. If the Doppler cooling stage is omitted, the trapped ensemble contains a residual part of $m_J = +1$ atoms. The inelastic rates are determined by trap loss observations. By disturbing the aspect ratio of the sample and measuring the reequilibration time, the elastic scattering rate can be determined. Experiments were conducted for ensembles between 0.5 mK and 2.5 mK; the temperature was adjusted by 1-dim Doppler cooling in the magnetic trap and by adiabatic variation of the trapping potential. The values for the elastic and inelastic rates were found to be roughly equal to each other at a value around $3 \times 10^{-10}\,cm^3/s$, largely independent of the temperature or the magnetic field in our trap (2-10 G). Figures 7.2 and 7.5 summarize the results of the cold collision experiments.

The measured elastic scattering rates exceed the predictions made in [56] by about a factor of two. They exceed the unitarity limit for s-wave scattering by even a factor of ten, thus clearly confirming the multichannel character of the scattering process. The measured inelastic rates surprisingly exceed the theoretical predictions by about one order of magnitude, a fact that could be attributed to a number of reasons. The theoretical values accessible to

us are calculated for a magnetic field of 100 G and are thus a slightly larger than the fields accessible in the experiment. The theoretical data show an increasing tendency towards smaller values of the magnetic field. Next, the theory gives values only for ensembles with perfect spin polarization. Qualitatively, the authors estimate the inelastic rates to be higher if spin mixtures are involved. In the theoretical description, only long range interactions were considered, whereas collisions between atoms of mixed spin are expected to exhibit short range molecular dynamics, resulting in higher inelastic rates. Finally, the temperature of the ensembles used in the experiments is higher than the range addressed in [56]. As a consequence, the assumption of an entrance channel limited to the s-wave might not be applicable for the present experimental conditions.

An older version of the apparatus that was used for all experiments presented here is extensively described in [45]. The experiment was subsequently moved to a new lab and a number of modifications were introduced during the rebuilding of the setup. I will summarize the complete setup to make this text readable as a consistent unit without focusing on the details and instead concentrate on characterizing the status quo of the experiment.

The thesis is organized as follows: Chapter 2 describes the laser systems that are used in the experiment. Light at three different wavelengths is needed to run the experiment, two of which are in the blue part of the spectrum at 423 nm and 430 nm, the other is in the infrared at 1978 nm. The radiation at 423 nm is used to drive the principal fluorescence line and is generated by a three-stage high-power solid state laser system: A commercial laser system at 532 nm is used to pump a home-made Ti:Sapph laser, which is in turn frequency doubled in an LBO crystal. For detection purposes, we need 430 nm at a low power that can be generated by a frequency doubled diode laser. The light at 1978 nm is used for a second cooling stage and also requires a three-stage solid state system: A second Ti:Sapph, pumped by a second laser at 532 nm, is used to pump a Tm:YAG solid state laser.

Laser cooled atomic samples are very dilute with densities as low as $10^8\,\mathrm{cm}^{-3}$. The experiments therefore need to be conducted in an ultra-high vacuum environment. Pressures below the 10^{-10} mbar mark are desirable. Chapter 3 describes the vacuum chamber, which the experiments were conducted in.

Chapter 4 explains the first cooling and trapping stage in the experiment. Unlike some other elements, Ca cannot be captured from a background vapor at low temperatures and has to be heated in an oven to about 600 °C. Such a high temperature requires the use of a Zeeman slower as a first cooling stage to slow down the atoms enough that they can be captured in a magneto-optical trap. The principal fluorescence line of Ca at 423 nm is especially well suited for use in the Zeeman slower and the MOT because its large natural linewidth of $\Gamma = 2\pi \times 34\,\mathrm{MHz}$ results in a large scattering rate of photons. It does, however, not permit to reach very low temperatures and is limited to the Doppler temperature of $T_D = 0.8\,\mathrm{mK}$. The lack of magnetic sub-structure of the ground state excludes any sub-Doppler cooling

mechanisms. In addition, the transition is not closed and populates the metastable $^3P_2$ stage with a branching ratio of 1:100 000.

The metastable state, which is populated with a high flux of precooled atoms is now cooled in a second MOT at 1978 nm. This transition has a much lower linewidth of $\Gamma = 2\pi \times 130\,\mathrm{kHz}$ and its Doppler temperature is $T_D = 3.1\,\mu\mathrm{K}$. Plus, sub-Doppler temperatures might be achievable because of the magnetic sub-structure of its ground state. Chapter 5 characterizes this infrared trap.

After the initial cooling and trapping stages, the atoms are transferred to a purely magnetic trap. Chapter 6 describes the loading of the trap and the preparation of the samples that the collision experiments are performed with.

The results of the experiments are detailed in Chapter 7 and compared to the theory of [56]. Chapter 8 concludes the main body of the thesis with a summary and gives an outlook on future experiments that could answer new and open questions.

2 Laser Systems

The experiments that are presented in this thesis require laser systems that generate light at three different wavelengths. Light at 423 nm is needed to drive the transition between the singlet $^1S_0$ ground state and the excited singlet $^1P_1$ state of calcium. It is used in the first magneto-optical trap, the Zeeman slower, the optical molasses, and the absorption imaging system. The second magneto-optical trap, building on the metastable $^3P_2$ state, operates at 1978 nm. In addition, this wavelength is used for the 1-dim Doppler cooling stage in the magnetic trap. Finally, for detection purposes, light at 430 nm is used to optically pump the metastable atoms back to the ground state. See Figure 4.2 for a diagram of the relevant energy levels of calcium.

This Chapter describes in brief the laser systems that are used in the experiments. The general setup is identical to the one described in [45], but a number of modifications were introduced to improve the frequency stability and adjustability of the systems. The last part of the Chapter describes the beam transfer system that was developed by C. Zafiu.

Various types of spectroscopy and stabilization techniques are used in the setups. The two most prominent are Doppler-free polarization spectroscopy [97] and frequency modulation (FM) spectroscopy [11,34,76]. A very comprehensive text on laser spectroscopy that describes the methods employed is [29]. A good introduction to the Pound-Drever-Hall stabilization technique is given in [12].

2.1 423 nm

The blue light at 423 nm is generated by a three component laser system: A commercially available laser[1] at 532 nm with an output power of 10 W is used to pump a home-made Ti:Sapph laser [101]. The Ti:Sapph is tuned to yield 1.5 W of light at 845.351 nm[2] in two adjacent resonator modes due to the standing wave design of the resonator. The infrared light is frequency doubled (by sum frequency mixing) in an LBO crystal inside a high-finesse ring resonator (Figure 2.1). The total maximum output power of blue light is 360 mW and is divided into three frequency components that differ by the free spectral range of the Ti:Sapph. The center frequency component contains two thirds of the total power, hence 240 mW of blue light are usable in the experiment.

The LBO cavity is stabilized to the frequency of the infrared light with a Pound-Drever-Hall setup: Sidebands at 40 MHz are modulated onto the infrared light by an EOM (electro-optic modulator, $LiNbO_3$). A photodiode detects the light that is reflected by the LBO cavity and records the beat signal between the main carrier and the sidebands. A mixer[3] compares the phase of the beat signal with the original 40 MHz signal provided by a VCO[4] (voltage controlled oscillator) and generates a dispersive error signal. An integrator (I-controller) feeds the signal to an intra-cavity piezo ceramic with a small mirror fixed to it that adjusts the length of the cavity to keep it commensurate with the incoming infrared wavelength.

For stabilization of the frequency to the atomic transition, a part of the blue light is directed to a polarization spectroscopy setup. The integrated error signal is used to keep the resonator length of the Ti:Sapph at a fixed value. The active element is again a small resonator mirror that is attached to a piezo ceramic. It proved favorable for the stability of the Ti:Sapph laser to have the Ti:Sapph crystal cooled by a solid state chiller providing a thermal stability of $\pm 0.1\,^{\circ}C$[5]. The LBO is Brewster-cut for the infrared radiation because anti-reflective coatings at its ends would not withstand the high light intensities in the resonator. As a consequence, a part of the blue light (about 40 mW), which is polarized perpendicular to the infrared light, is reflected at the crystal end and leaves the crystal through one of its sides. It is divided into two rays of different polarization and can be used for spectroscopy. One of the rays is circularly polarized by a quarter wave plate and serves as pump beam. The other one serves as probe beam and is attenuated to 10% of its power. It is directed through an AOM[6] for frequency tunability. A polarizing beam-splitter cube is used as a polarizer. The counter-propagating pump and probe beams are directed through a glass cell housing a small calcium oven that produces a calcium vapor. Further frequency shifting can be achieved by a magnetic

[1] Verdi V10, Coherent Inc.
[2] Wavemeter reading when in resonance with the atomic transition.
[3] Mini-Circuits RPD-2
[4] Mini-Circuits POS-50
[5] Thermotek T-255P
[6] IntraAction ADM-40, center frequency 40 MHz

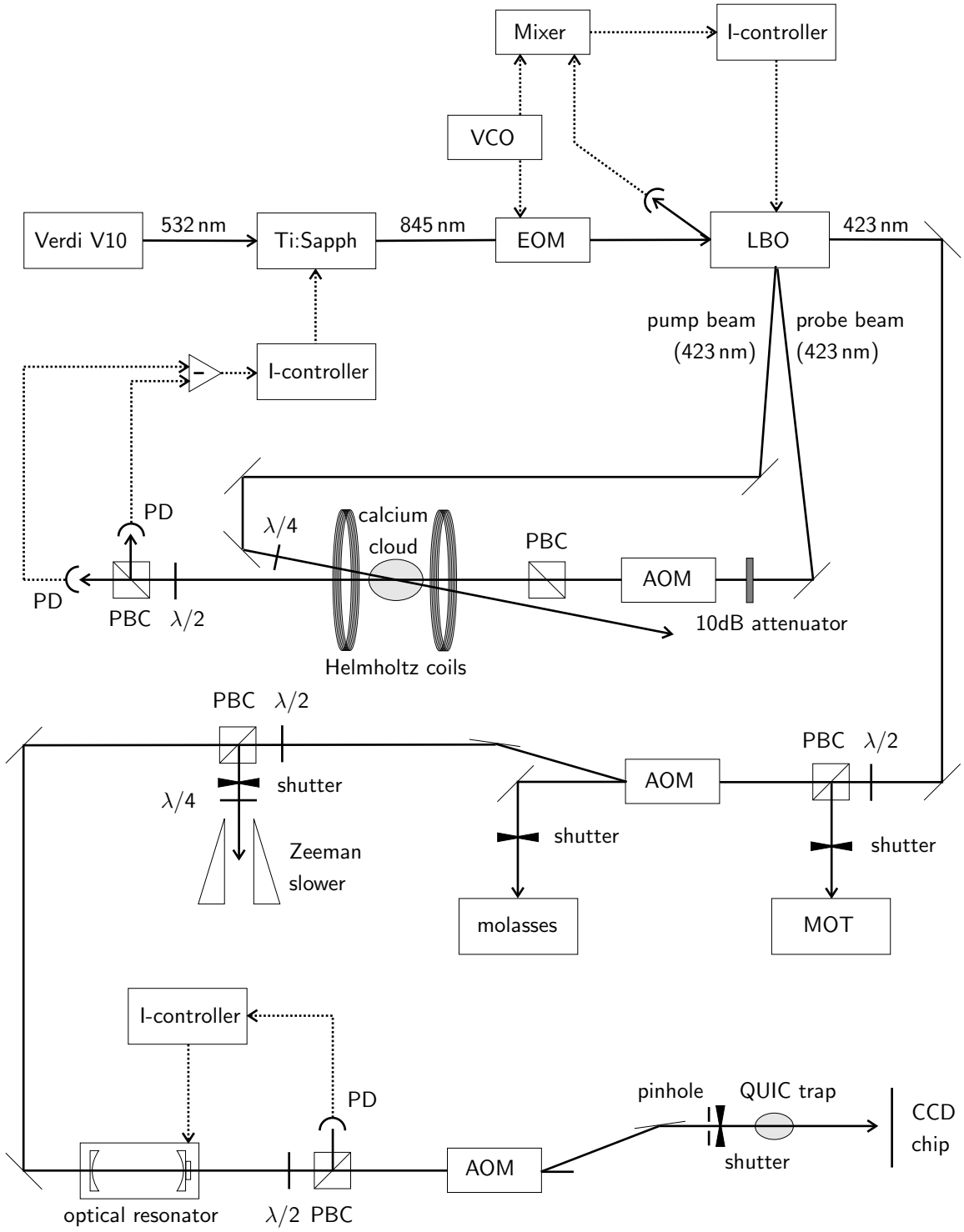

Figure 2.1: 423 nm laser system setup. VCO: voltage controlled oscillator, EOM: electro-optic modulator, LBO: lithium tetraborate frequency doubling crystal, PD: photodiode, PBC: polarizing beamsplitter cube, AOM: acousto-optic modulator, MOT: magneto-optical trap, $\lambda/2$, $\lambda/4$: retardation plates. Solid lines are light beam paths, dashed lines are electronic signal paths. The numerous lenses used in the setup are omitted in this schema. See text for further explanation.

field that is oriented in parallel to the beam propagation direction and that is produced by two coils in Helmholtz configuration. After passing the spectroscopy cell, the probe beam is split in two by a half wave plate and a cube and is recorded by two photodiodes. The induced birefringence in the calcium vapor is detected by taking the difference of the diode signals and the result is fed to the Ti:Sapph intra-cavity piezo by an integrator. When running the experiment, the frequency of the blue light is set to maximize the population of the blue MOT by adjusting the electronic offset of the error signal. For a first rough adjustment of the laser frequency, we use a home-made Michelson-type wavemeter [15, 48].

The main output of the LBO is divided into two parts, one of which is used to set up the magneto-optical trap (cf. Chapter 4), the other one is sent through an AOM[7]. The undetuned zeroth order is used in the optical molasses. The first order is red detuned by 274 MHz and is used for the Zeeman slower. A quarter wave plate just before the slower exit sets the σ^+ polarization of the light. For absorption imaging, a tiny part is split from the slower beam and directed to a small standing wave resonator made of two concave mirrors[8]. One of the mirrors is glued to a piezo ceramic tube to adjust the length of the resonator; part of the transmitted light is recorded by a photodiode and the transmission spectrum is used to lock the resonator to the TEM_{00} mode with a side-of-fringe technique. The resonator serves two purposes: The pointing stability of the beam is significantly improved while the active stabilization ensures a constant light intensity in the beam. The greater part of the transmitted light is directed through another AOM[9] that tunes the light back into resonance. The frequency is set such that we receive a maximum absorption signal for cold atoms that are released from the magnetic trap. (315 MHz, i.e., 41 MHz above the MOT transition.) After the AOM, the beam is sent through a 50 µm pinhole to remove any residual higher order modes from the beam and obtain a Gaussian beam profile. A CCD camera images the beam after having passed the atomic cloud at the site of the QUIC trap.

Mechanical shutter assemblies[10] are used for independent control of the MOT, molasses, slower, and imaging beams. A beam that exhibits a tight focus at the position of the shutter can be switched in about 250 µs. For faster switching times, an AOM is needed. The shutter is then used to block residual light propagating through the AOM while the radio frequency is switched off.

[7] Crystal Technology 3250-190, center frequency 270 MHz
[8] Diameter = 12.5 mm, radius = -100 mm, reflectivity = 80%, distance = 22 mm
[9] IntraAction ATM-2701A1, center frequency 270 MHz
[10] Densitron TK-CMD

2.2 1978 nm

The system that generates light at 1978 nm also consists of three components: A commercially available laser system[11] with an output of 5 W at 532 nm pumps a home-made Ti:Sapph laser similar to the one in the 423 nm setup [101]. The Ti:Sapph crystal is cooled with the same solid state chiller system[12] and the laser is tuned to emit 900 mW at about 785.8 nm. The infrared light is used to pump a home-made Tm:YAG laser [78] that yields 60 mW of light at 1977.677 nm[13] divided into two modes separated by a free spectral range of the resonator (1 GHz). About 20% of the output power is used for spectroscopy, the rest is directed to the experiment for the MOT and the 1-dim Doppler cooling stage. Figure 2.2 shows a schema of the setup.

The narrow linewidth of the infrared transition of 130 kHz requires a high frequency stabilization of the laser. A Pound-Drever-Hall technique was chosen here because of its robustness due to its insensitivity to intensity fluctuations of the laser. An AOM[14] in the spectroscopy branch is used in connection with a second, identical AOM in the MOT and Doppler cooling setup to adjust the frequency of the light over a range of roughly 20 MHz. After passing the AOM, the light is split in a pump and a probe beam; a half wave plate aligns the linear polarization of the pump beam with the probe beam. The intensity in the probe beam can be controlled independently by a polarizing beam-splitter cube and a half-wave plate. For spectroscopy, we use a glass cell similar to the one used in the setup of the 423 nm system (cf. Figure 2.4). The cell is filled with 2 torr of neon; an electric discharge running at 500 V is used to populate the metastable state. Helmholtz coils around the cell generate a magnetic field along the propagation direction of the beams that is used to tune the transition frequency by varying the Zeeman shift. Sidebands at 36 MHz are modulated onto the probe beam by an EOM ($LiNbO_3$) before passing through the calcium vapor. A fast InGaAs photodiode[15] monitors the absorption of the probe beam. The signal is demodulated by mixing[16] it with the original frequency of the VCO[17]. A PI-controller (with proportional and integral transfer characteristic) is used to feed the error signal to an intra-cavity piezo ceramic that adjusts the length of the Tm:YAG resonator. Details on our particular spectroscopy setup are published in [51].

The second AOM sets the detuning for the MOT and the 1-dim Doppler cooling stage. Since these two parts do not operate simultaneously, the beam is split after the AOM; for 1-dim Doppler cooling, the frequency is set 15 MHz below the MOT frequency. The larger

[11] Verdi V5, Coherent Inc.
[12] See footnote 5.
[13] See footnote 2.
[14] IntraAction ACD 402AA3, center frequency 40 MHz
[15] Hamamatsu G8422-03
[16] See footnote 3.
[17] See footnote 4.

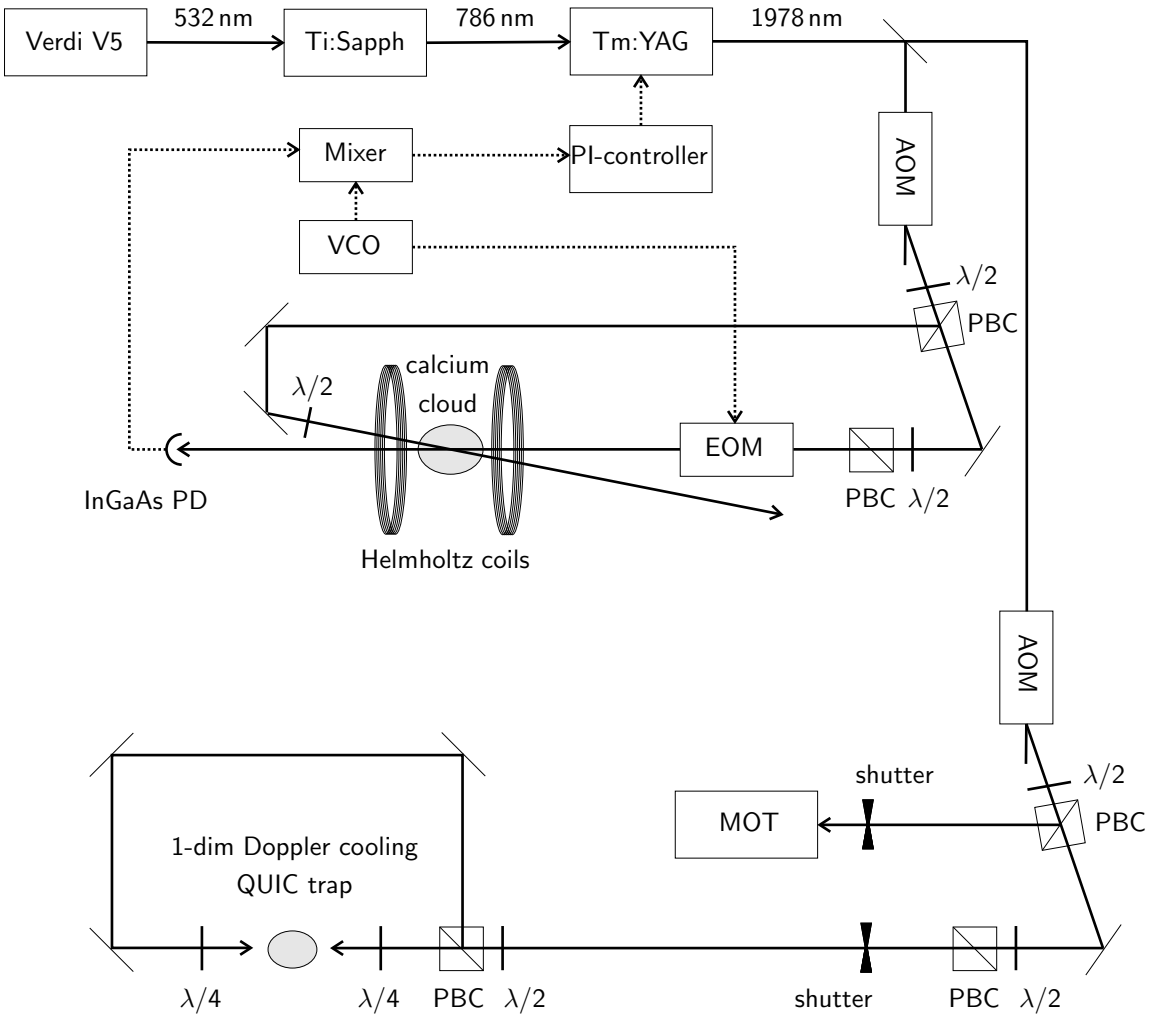

Figure 2.2: 1978 nm laser system. VCO: voltage controlled oscillator, AOM: acousto-optic modulator, EOM: electro-optic modulator, PBC: polarizing beam-splitter cube, PD: photodiode, $\lambda/2$, $\lambda/4$: retardation plates, MOT: magneto-optical trap. Lenses used in the system are not shown in the figure. See text for further explanation.

part is directed to the MOT, the smaller part is again divided in two. Quarter-wave plates in each beam set the σ^+/σ^+ polarization for the Doppler cooling. The intensity and the balance in the Doppler cooling beams can be controlled independently by two pairs of polarizing beam-splitter cubes and half-wave plates. When running the experiment, the laser frequency is fine tuned by adjusting the electronic offset of the error signal to minimize the sample temperature (i.e., the sample radius).

2.3 430 nm

We generate about 6 mW of light at 430 nm with a frequency doubled diode laser system. A diode laser [82] at 860.512 nm[18] emits about 30 mW of infrared radiation. This setup permits the use of a $KNbO_3$ crystal for frequency doubling [75] because the involved intensities are comparatively small. The high conversion efficiency of $KNbO_3$ lets us use a cavity of lower finesse than in the case of LBO and, hence, eases the stabilization of the resonator to the incoming light. The cavity is stabilized to the infrared light by a Pound-Drever-Hall setup just as described in Section 2.1, the only difference is that no EOM is required because sidebands can directly be generated by modulating the current of the laser diode. See Figure 2.3 for a sketch of the setup.

The blue light is split in a part that is directed to the experiment and a second part for spectroscopy. For fast switching of the light, an AOM[19] is introduced into the branch serving the experiment; a second identical AOM in the spectroscopy setup is needed to compensate the frequency shift in the first diffraction order. Higher order modes are removed by directing the beam through a 100 µm pinhole; the beam is subsequently split in a part that pumps the MOT volume and a second part serving the QUIC trap. We employ again Dopper-free polarization spectroscopy, just as described in Section 2.1. For clean linear polarization in the probe beam, we here employ a calcite polarizer. Spectroscopy is performed on the same discharge cell that is also used in the 1978 nm setup; to avoid cross interactions between the two wavelengths, we were careful to minimize the overlap of the beams in the calcium vapor. The integrated dispersive error signal is used to control the current of the laser diode. A detailed account of the spectroscopy on the $^3P_2$ (4s4p) $\rightarrow$ $^3P_2$ (4p4p) transition is published in [51]. Figure 2.4 shows a photograph of the discharge cell in operation. The orange background is the fluorescence of neon, the thin blue thread at the center is the fluorescence at 430 nm. The calcium oven is located just below the beams for spectroscopy, it serves also as the anode of the discharge. Just above the beam, the ring that serves as cathode is visible.

[18] See footnote 2.

[19] Crystal Technology 3080-120, center frequency 80 MHz

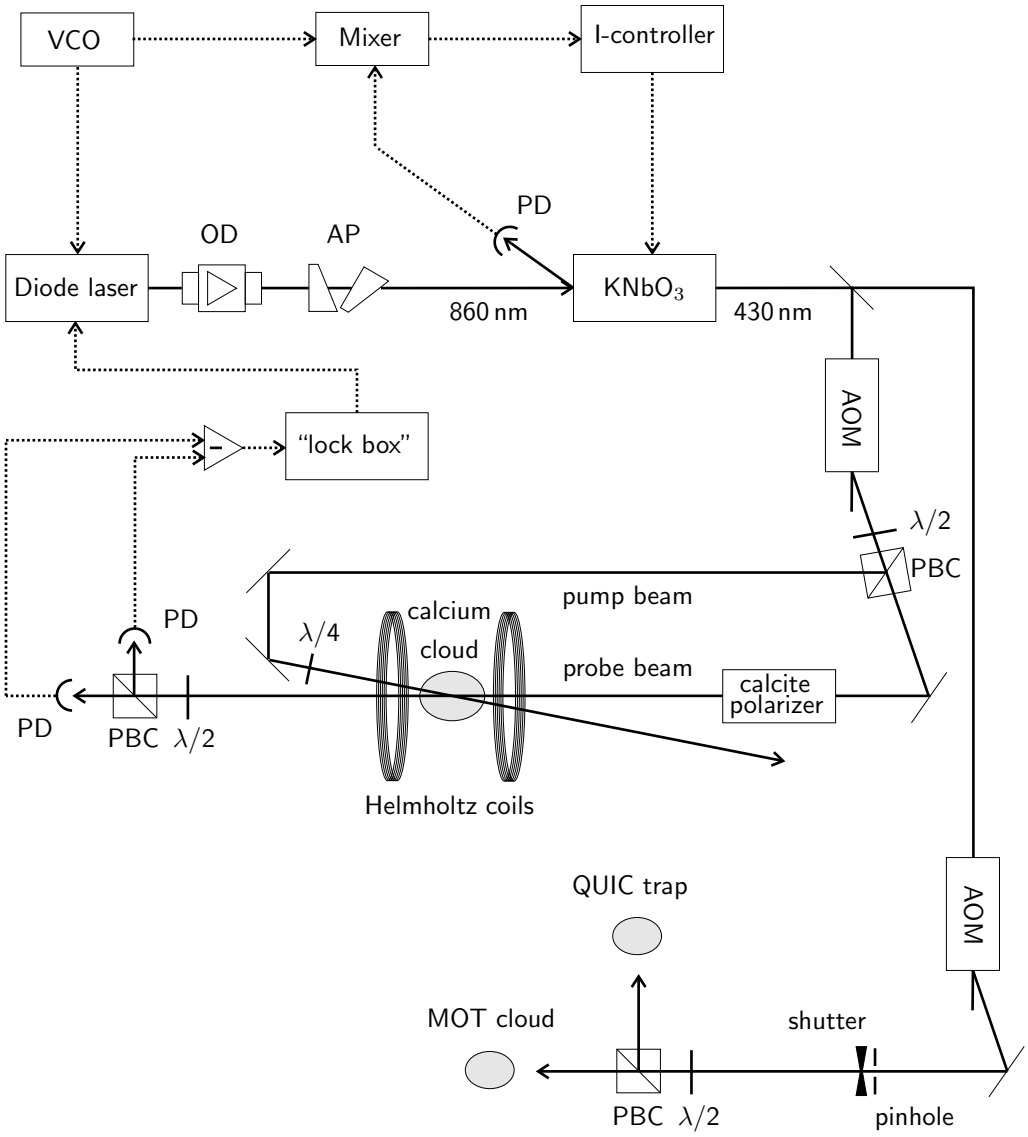

Figure 2.3: 430 nm laser system. VCO: voltage controlled oscillator, OD: optical diode (Faraday isolator, 60dB), AD: anamorphic prism pair, PD: photodiode, $KNbO_3$: potassium niobate crystal for frequency doubling, AOM: acousto-optic modulator, PBC: polarizing beam-splitter cube. Lenses used in the setup are not shown in the figure. See text for further explanation.

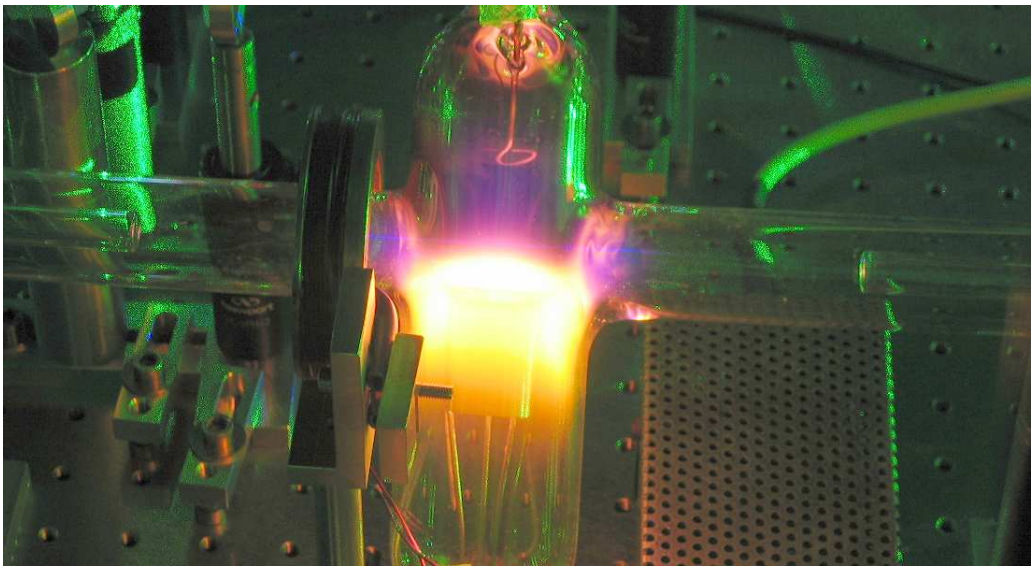

Figure 2.4: Calcium discharge cell. The lower part of the cell houses the calcium oven, which, in this picture, is surrounded by a bright neon discharge. This discharge populates the metastable state for spectroscopy; the thin blue horizontal thread just above the oven exit is the fluorescence induced by laser light at 430 nm. The small ring in the upper part of the cell is the cathode, the oven serves as the anode of the discharge. To the left of the discharge, one of the Helmholtz coils can be seen; the other coil was added after the picture was taken.

2.4 Beam transfer between optical tables

The experimental setup is divided between two optical tables (3.5×1.5 m^2 each) that are roughly 4 m apart. The vacuum chamber and surrounding optics for the magneto-optical traps etc. rests on one of them (henceforth called "vacuum table"); the other one is used for the installation of the laser systems and spectroscopy setups ("laser table"). Both optical tables rest on concrete blocks weighing several tons that are decoupled from the ground by a set of massive iron springs. As a consequence, the tables can change their position with respect to each other by distances on the order of a mm, thereby destroying any potential optical alignment between them. Hence, a beam transfer system is needed, compensating the mechanical drifts between the tables by ensuring that the laser beams always enter the optical setups on the vacuum table under the same angle and at the same position. Optical fibers, unfortunately, cannot be employed here because the cutoff frequencies of currently available products lie in the blue range of the optical spectrum and would cause unacceptably high losses.

The system that was developed for the experiment by C. Zafiu consists of a computer controlled active stabilization system (Figure 2.5). For each laser beam there is a set of

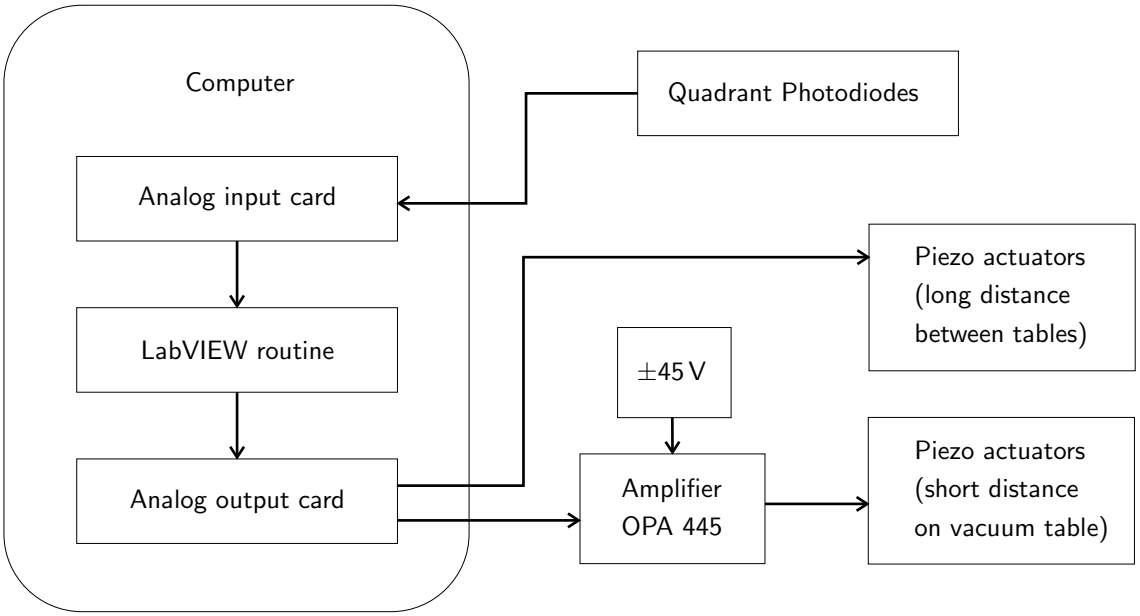

Figure 2.5: Beam stabilization setup for transferring the laser beams between the laser table and the vacuum table.

two quadrant photodiodes[20] and two mirrors that are attached to piezo elements[21]. The photodiodes record a deviation of the beam perpendicular to its propagation direction and the mirror can be electronically adjusted to compensate small deviations. The piezo-mirror element is attached to a mechanical mirror mount that allows manual compensation of larger drifts that cannot be compensated by the piezos. Thus, by keeping each beam pointed at the center of two quadrant diodes on the vacuum table, the optical alignment on the vacuum table can be maintained. The lasers are sent through plastic pipes on their way between the two tables to minimize jitter due to fluctuations of the refractive index of the air caused by the air conditioners in the room. The achieved pointing stability is sufficient to run the experiment except in the case of the absorption imaging setup, where we employed an additional optical resonator to enhance the stability (see Section 2.1).

Two analog I/O cards[22] are used to read the signals from the photodiodes and to set the voltages for the piezos. Signal processing is done by a LabVIEW routine (cf. Appendix D). The $\pm 10\,\mathrm{V}$ supplied by the analog output card are sufficient to actuate the piezos directing the beam between the tables; the signal has to be amplified[23], however, to drive the second piezo because the distance to the second diode is less than half the distance between the first piezo-diode pair and, hence, more stroke is needed.

[20] Laser Components, hybrid quadrant photodiode JQI 5P incl. amplifier

[21] Piezomechanik GmbH, bending actuator BM 70/25/200M for 430 nm and 1978 nm, piezo stack PSt 150/2x3/20 for 423 nm

[22] Geitmann GmbH, analog out: ADLINK PCI-6216V, analog in: ADLINK PCI-9113A

[23] Burr-Brown operational amplifier OPA445

3

The Vacuum Setup

The vacuum chamber is the central piece of the setup since it houses the experiments conducted with calcium. The main chamber that contains the magnetic field coils was completely redesigned to accommodate a number of improvements to the previous setup. Specifically, we intended to have more optical access to the trap regions, we wanted a setup that can accommodate magnetic field coils inside the vacuum, and we wanted to improve the vacuum conditions. The chamber housing the calcium oven and the Zeeman slower is, apart from minor changes, identical to the original version. Figure 3.1 shows a schema of the apparatus. A very comprehensive summary containing all aspects of vacuum technology can be found in [100].

The oven section of the chamber can be seen in the far right corner of Figure 3.1. It is constructed with KF flanges; we exchanged all viton gaskets in the oven chamber with aluminum gaskets to reduce outgassing. Aluminum gaskets are a bit more difficult to handle and are more expensive than their viton counterparts, however, the initial charge of calcium now lasts for over 1.5 years and, thus, the gaskets do not have to be replaced frequently. A pneumatic, viton-sealed KF16 valve[1] separates the oven chamber from the slower entrance. An additional atomic beam shutter was constructed such that the beam can be blocked. The beam shutter is located between oven and valve; a thin steel plate is attached to two μ-metal rods that can be moved by switching two electromagnets. Unfortunately, the beam shutter broke down a few months into the experiment; we did not attempt to fix it since we wanted

[1] VAT KF16 mini UHV gate valve with pneumatic actuator, model 01224-KA44-0001/0083

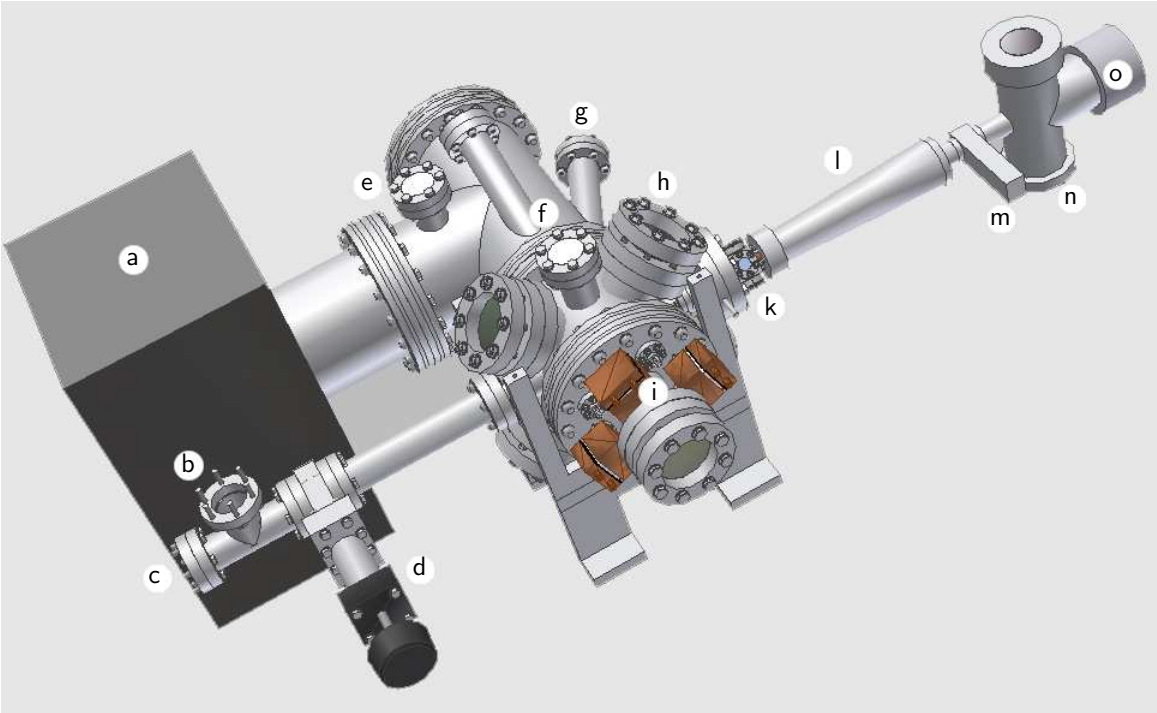

Figure 3.1: Schema of vacuum chamber. a: ion combination pump (titanium sublimation pump on backside), b: CF40 flange for pressure gauge (Leybold ITR100) and turbo-molecular pump, c: CF40 Zeeman slower window, d: gate valve, e: CF40 flange for pressure gauge (Leybold IE514), f: CF40 viewport for 1-dim Doppler cooling, 2nd viewport directly below, g: CF40 viewports for fluorescence measurements, h: CF63 viewports for the MOT, i: CF63-CF150 adaptor flange that holds the magnetic coil setup, 4 CF16 flanges are used for the Peltier cooled copper rods and 4 CF 16 flanges are for the electric feedthroughs, k: optical molasses and atomic beam shutter, the shutter was later mounted at position m, l: Zeeman slower, m: pneumatic valve, n: KF63 flange for turbo-molecular pump, o: calcium oven.

to refrain from reopening the chamber.

The Zeeman slower connects the oven and main chambers. It serves also as a differential pumping stage between the chambers since at a length of about 40 cm and a diameter of 1.6 cm its conductance is rather small. The optical molasses part is implemented as a 6-way CF16 cross at the slower exit.

The main chamber (seen in the center of Figure 3.1) consists of a short CF150 pipe (length 160 mm). Radially attached are 4 CF63 flanges for the MOT viewports, two opposite CF40 flanges for the 1-dim Doppler cooling viewports, and one CF16 flange opposite another CF40 flange for the Zeeman slower entrance and exit. The heart of the chamber is formed by the magnetic coil setup that is mounted on a CF63-CF150 adaptor flange which attaches to one of the main chamber's CF150 ports. The CF63 end of the adaptor flange receives the fifth MOT viewport. A CF150 tee is attached to the other end of the main chamber and accommodates

the ion pump and the sixth MOT viewport. Attached to the tee are three pipes with CF40 viewports whose axes are pointed towards the center of the MOT coils and that can be used for observation of fluorescence. Inside the tee, along the axis of each of the three pipes, lenses are attached[2] that collect the fluorescence light and image the MOT to a point just outside the chamber.

The magnetic coils are mounted on bases of oxygen-free high conductivity (OFHC) copper that rest on 4 copper rods of a diameter of 13 mm (cf. Figure 6.2(b)). The copper rods serve as thermal feedthroughs and are cooled by one peltier element[3] each down to -40 °C at one end to remove the heat dissipated in the coils. The CF63-CF150 adaptor flange contains another 8 CF16 flanges; 4 of which receive the copper rods and thereby fix the assembly to the flange, the other 4 are used for electrical feedthroughs.

All wires used for the magnetic coils are made of copper insulated with polyimid. They were specifically cleaned by the manufacturer to meet the ultra-high vacuum (UHV) requirements (see Appendix A.1 for details). UHV conditions can be maintained up to temperatures of about 120 °C of the wires (temperature determined by a resistance measurement). At higher temperatures the outgassing results in an increase of the pressure in the chamber and some time has to be allowed for the coils to cool down. The effect varies considerably between the large MOT coils and the tiny QUIC coils. At normal MOT operating conditions of 3 A the coil temperature in steady state mode increases relatively slowly and an increase in pressure is seen after about 0.5 h. Since the experiment is usually run in a pulsed mode where the MOT is active for 1-2 s and subsequently inactive for >2 s during the magnetic trapping cycle, heating of the MOT coils is in general unproblematic. Considerable attention, however, has to be directed to the timing when using the QUIC trap. Although very little heat is dissipated in the coils because of their small size, the temperature can rise dramatically (such that the pressure rises by more than 5 orders of magnitude in a few seconds!) if a high current is applied for too long. The reason is probably that the outer windings of the coils are well insulated from the copper base by the inner windings and the rise in temperature is enhanced by the high specific resistance of the thin wires. As an example, at a current of 3 A in the QUIC coils, magnetic trapping time is limited to <500 ms and after each use of the trap an additional dead time of >30 s should be allowed for further cooldown. Conversely, at QUIC currents around 1 A, observation times around 15 s are easily achievable. When operating the experiment, the pressure can easily be monitored by a LabVIEW routine that reads out the pressure gauges and displays the current pressure vs. time trace (see Appendix D).

When conducting laser cooling and trapping experiments, one crucial prerequisite is a good optical quality of the chamber viewports in order not to distort the laser beams that are directed into the chamber or that are used for imaging the atom clouds. Commercial viewports

[2] f = 100 mm, no coatings, visible diameter = 38 mm, distance to MOT = 164 mm ⇒ solid angle = $4\pi \times 3.32 \times 10^{-3}$

[3] $P = 68\,\mathrm{W}, I_{max} = 8.5\,\mathrm{A}, U_{max} = 15.4\,\mathrm{V}, \Delta T_{max} = 80\,^{\circ}\mathrm{C}$

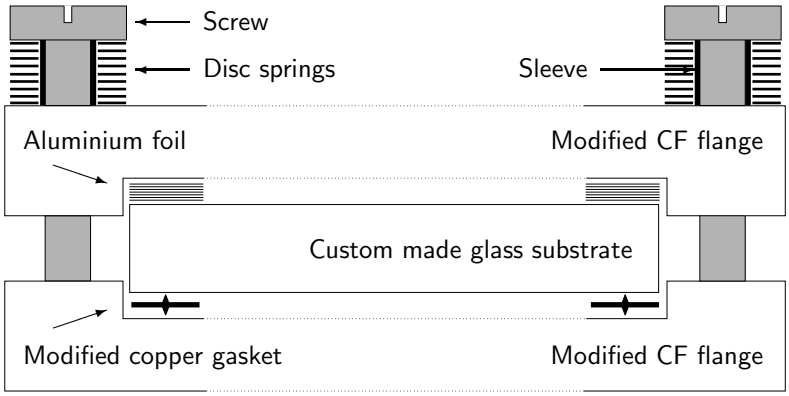

Figure 3.2: High optical quality vacuum viewports. See text for explanation.

are usually not adapted to these requirements and custom made ones are extremely expensive if available at all. Hence, we resorted to a home-made design developed by the Kasevich group [70] and refined by the cold atom group at the PTB[4] (Figure 3.2). We use high optical quality glass substrates that received an anti-reflective coating for both 423 nm and 1978 nm. Two sharp circular ridges are lathed from a commercial CF copper gasket that is used between the glass and the UHV flange. The usual knife edge is removed from the UHV flange and the seal is established by the two ridges of the copper gasket. A second flange is used to apply pressure to the seal, some aluminum foil between the steel of the flange and the glass cushions the pressure. A stack of disc springs[5] helps to buffer the expansion of the assembly during the heating and cooldown period when baking the chamber.

Several vacuum pumps are employed to maintain the vacuum conditions. A 200 l/s turbo-molecular pump[6] is used at the oven chamber. The main chamber itself is evacuated by a 300 l/s ion pump[7]. The pumping efficiency at low pressures is enhanced by a titanium sublimation pump[8] that is mounted in a liquid nitrogen cooled cryopanel[8]. An additional turbo-molecular pump[9] is located near the Zeeman slower window. Since the window may become intransparent by being coated with calcium, a CF40 valve[10] allows the separation of that part of the chamber such that the window can be exchanged without having to vent the whole chamber.

Two pressure gauges are installed at the chamber. An extractor type ionization gauge[11] is located at the CF150 tee and can measure pressures below the 10^{-11} mbar level. A second,

[4] Physikalisch-Technische Bundesanstalt
[5] DIN 2093, to be used with a custom made sleeve to prevent shifting
[6] Leybold Hy.Cone 200, with fore-line pump Leybold Trivac D2.5E
[7] Varian Diode 300 combination pump
[8] Varian TSP cartridge with 3 filaments mounted inside Varian TSP cryopanel
[9] Leybold Turbovac TW 70 H, with fore-line pump Leybold Trivac D1.2E
[10] VAT CF40 viton sealed UHV gate valve
[11] Leybold IE514

Bayard-Alpert type, ionization gauge[12] sits at the Zeeman slower window section and measures pressures down to 1×10^{-10} mbar. The lowest pressure we achieved in the chamber is better than 2×10^{-10} mbar, which is the lowest reading measured by the extractor gauge when the oven chamber is separated from the main chamber by the KF16 valve. The actual pressure in the chamber might be still lower than the extractor gauge reading; the Bayard-Alpert gauge reading underruns its minimum range of 10^{-10} mbar.

During the assembly of the chamber, great care was taken to ensure the cleanliness of the components. All parts were cleaned in an ultrasonic bath filled alternately with acetone and ethanol to remove residual oils from the surfaces. To remove oxidized stains from steel and especially from copper surfaces, the parts were submerged in a 5% solution of hydrochloric acid for 1-2 min and subsequently cleaned with a Tickopur solution and then with water. The steel parts of the main chamber were electropolished prior to assembly. We used rubber gloves if any parts needed to be touched that reside inside the vacuum chamber. All scrwes inside the vacuum received slits to prevent the formation of air pockets inside the chamber. After assembly, the chamber was baked at 230 °C for one week; to prevent leaks from forming at the window gaskets, one week was allowed for heating up to and cooling down from the maximum heating temperature.

[12] Leybold ITR100

4

Cooling and Trapping Atoms with Light at 423 nm

This Chapter deals with cooling and trapping calcium atoms with light of the principal fluorescence line at 423 nm. Its large linewidth of $\Gamma = 2\pi \times 34.6\,\mathrm{MHz}$ makes it especially suitable for effectively cooling and trapping a large number of atoms. Due to the absence of a magnetic structure in the ground state, the temperature that can be reached on this transition is Doppler-limited to $T_D = 0.8\,\mathrm{mK}$. In addition, the transition is not closed and exhibits a loss channel into a metastable triplet state, a fact that would normally be considered disadvantageous. Here, we take advantage of it and implement a further cooling stage building on the metastable state (cf. Chapter 5) that uses light at 1978 nm. The Doppler limit of the second cooling stage is almost three orders of magnitude lower at $T_D = 3.1\,\mu\mathrm{K}$, and the presence of polarization gradients promises to achieve sub-Doppler temperatures. The recoil limit of the infrared transition is $T_r = 121\,\mathrm{n}K$.

4.1 Generation of a beam of pre-cooled Ca atoms

The atom source, consisting of the oven, the Zeeman slower, and the optical molasses is essentially identical to the setup that is extensively described in [45, 47]. Hence, I will only briefly outline the main parts of the design and indicate changes and additions to the setup that are not covered in [45, 47].

The oven consists of a small steel cylinder, 60 mm in length and 20 mm in diameter that is filled with a few grams of Ca. It has 45 exit holes evenly distributed over one endcap; the

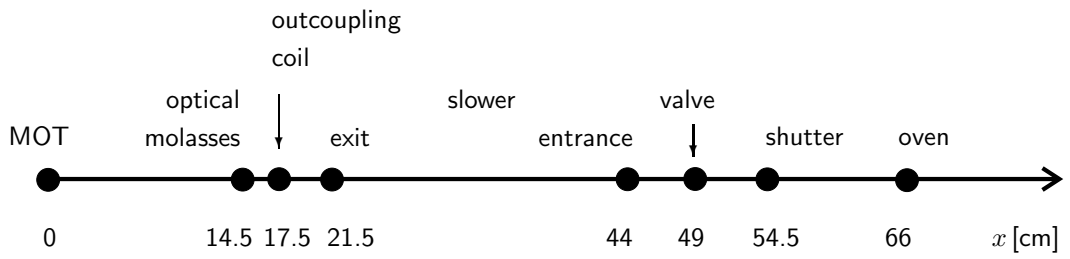

Figure 4.1: Calcium beam components. The beam travels a total distance of 66 cm from the oven exit to the MOT region. It passes an atomic beam shutter and a valve before entering the Zeeman slower. At the exit of the slower, the outcoupling coil tunes the atoms out of resonance. A 2-dim optical molasses that is set up perpendicular to the beam reduces the transverse velocity of the atoms to increase the flux into the MOT region.

exit holes are 10 mm long and 1 mm in diameter and thus serve as initial beam collimators. The oven is heated by a Thermocoax wire that is embedded in several grooves around the cylinder; a water cooled copper shell serves as a heat shield. Applying 19.9 VAC to the wire ($R = 12.5\Omega$ at room temperature) results in a temperature of about 590 °C at the oven, the temperature can be measured with a type K (NiCr-Ni) thermoelement that is attached to the oven. MOT operation can already be observed at temperatures above 570 °C; the atom flux can be varied by adjusting the oven temperature, the temperature of 590 °C was chosen for the data presented in this thesis.

It should be noted that the operating temperature at the current setup is considerably lower than the one previously used in [45, 50], which was about 660 °C. The vapor pressure of Ca in the oven is now about 1×10^{-2} mbar compared to 6×10^{-2} mbar before. To achieve comparable MOT operation at a significantly lower oven temperature is a good indicator that the modifications to the setup indeed yield a better cooling and trapping efficiency of the MOT. Furthermore, the entrance window in the vacuum chamber for the Zeeman slower laser beam is coated with calcium at a much lower rate than previously. Consequently, the window remains transparent for a much longer time and need not be replaced as frequently. In fact, after almost two years of operating the setup, no visible layer of Ca has formed to date. Previously, the window had to be replaced about once a year.

After traveling a distance of 22 cm, the atomic beam enters the Zeeman slower (see Figure 4.1 for the distances involved). The slower consists of a steel tube with an inner diameter of 16 mm; the slower coil is wound around this tube over a length of 22.5 cm. An additional shell of copper tubing is used for water-cooling of the coil. The laser beam entering the slower has a beam waist of 7 mm, such that the cross-sectional area of the slower tube is well covered. The power in the laser beam is adjusted such that the number of atoms in the MOT operating

at 423 nm ("blue MOT") is maximized. Best operation is achieved at a power of 80 mW[1] in the slower beam (measured before entering the vacuum chamber). The beam is red-detuned by 274 MHz with respect to the MOT frequency by an AOM. An additional outcoupling coil after the slower exit reverses the direction of the magnetic field, thereby tuning the atoms out of resonance with the slower laser. Slower and outcoupling coil parameters can be found in Table A.5

An optical molasses is set up at a distance of 70 mm after the slower exit. Since there is no transverse cooling in a Zeeman slower, the atomic beam leaving the slower is divergent to a certain extent. An optical molasses that is set up in 2-dim perpendicular to the slower axis reduces the divergence of the beam and hence increases the flux of atoms into the region of the magneto-optical trap. The molasses is set up with retro-reflected beams with a beam waist of 4 mm and a total power of 5 mW per beam. Anti-reflective coatings on the windows of the vacuum chamber and on the quarter-wave plates minimize the losses in the retro-reflected beam. The magnetic field at the position of the molasses has a small component transverse to the beam propagation with a zero crossing at the beam axis. By using circularly polarized light in the molasses beams, the atomic beam at the slower exit not only gets collimated but also narrowed down by exploiting the magneto-optical force on the atoms.

4.2 MOT at 423 nm

In the previous setup of the experiment [45, 47], the MOT at 423 nm was realized with laser beams with a beam waist of 4 mm. Optical access to the MOT region was limited by CF16 viewports of the vacuum chamber. The laser beams in each of the three MOT branches were retro-reflected to achieve the necessary light configuration of the trap.

The advantage of a setup with retro-reflected beams is that more laser power is available in each MOT branch, compared to a situation where 6 independent laser beams are used. Since the saturation intensity of the fundamental fluorescence line of Ca is quite high at $I_s = 60\,\mathrm{mW/cm^2}$ and the output power of our laser system is limited to about 240 mW at the correct wavelength, retro-reflecting beams is a good way to efficiently use the laser power at hand, thereby establishing a high scattering rate of light and hence effective cooling and trapping.

The disadvantage of such a setup is that the laser power in the reflected beam is lower than in the incident beam, even if care is taken to use optical components with good anti-reflective coatings and mirrors with high reflectivities. Unbalanced laser beam power results in radiation pressure on the atoms; the ensemble is then trapped at a position that might

[1] The actual measured power in the beam is 120 mW but only 2/3 of it are usable in the experiment; the rest is at off-resonant frequencies (cf. Chapter 2.1). Throughout this thesis, laser powers always refer to the usable center frequency component in the beam.

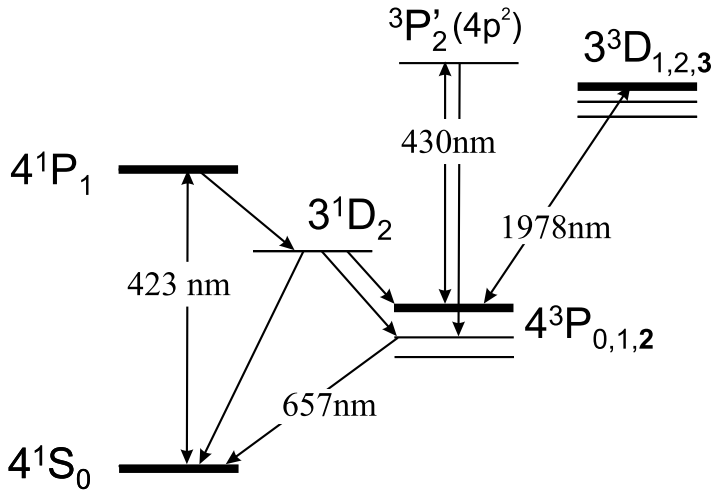

Figure 4.2: Relevant energy levels of calcium (schema taken from [45]). The principal fluorescence line at 423 nm is used for capturing the atoms in a first MOT. MOT operation can be monitored through the intercombination line at 657 nm. A second MOT at 1978 nm captures the metastable $^3P_2$ atoms for further cooling and trapping. $^3P_2$ atoms can be optically pumped to $^3P_1$ with light at 430 nm and the subsequent burst of light at 657 nm can be used for detection purposes.

differ from the center of the magnetic quadrupole that is generated by the MOT coils.

If one were only interested in trapping atoms on the principal fluorescence line, the position of the ensemble might be a minor concern. If, however, subsequent trapping stages are to be implemented, control over the position of the atoms can be of great importance. In this experiment, two MOTs are superimposed; the MOT at 423 nm loads the MOT at 1978 nm. The better the spatial overlap of the two traps, the more efficient the loading of the infrared trap is; hence control over the position of the atomic ensemble is needed. Therefore, a setup with 6 independent laser beams is chosen.

As a second improvement, laser beams with larger waists are used. The beam of atoms exiting the Zeeman slower is of a diameter on the order of the diameter of the slower tube plus any additional increase caused by the transverse velocity of the atoms. Thus, a capturing volume with a diameter roughly the size of the beam diameter is desired to maximize the flux of atoms into the MOT. Another consideration originates from the properties of the cooling transition. The $^1S_0 \rightarrow {}^1P_1$ transition of Ca is not closed; there is a weak decay channel into a $^1D_2$ state (branching ratio 1:10^5, [9]), from which the atoms decay to the metastable $^3P_2$ state, back to the ground state via the $^3P_1$ state, or directly back to the ground state (see Figure 4.2 for a diagram of relevant energy levels of Ca). The decay time from $^1P_1$ back to the ground state via $^1D_2$ and $^3P_1$ is governed by the lifetime of the $^1D_2$ state and amounts to a total of 4 ms; the direct decay to the ground state is much weaker at $\tau = 25$ ms [9]. If, during the time that an atom resides in $^1D_2$, it moves outside of the illuminated volume, it is lost from the trap; thus large laser beams are desirable. A beam waist of $w = 7$ mm was

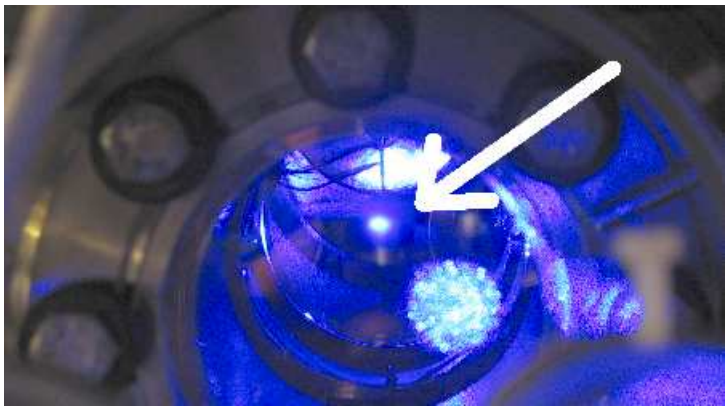

Figure 4.3: MOT at 423 nm during steady state operation. Diameter of the viewport is 68 mm.

chosen as a compromise of a large trapping volume and an acceptable scattering rate. If one assumes the MOT to operate near the Doppler temperature of $T_D = \frac{\hbar\Gamma}{2k_B} = 0.8\,\mathrm{mK}$, where Γ is the natural linewidth of the transition, the thermal velocity of the atoms is about 1 m/s and thus one expects most of the atoms that are not lost to the metastable state to remain in the trap. Indeed, it is shown in [46] that even at a smaller trapping volume nearly all atoms (95%) can be recycled in the trap.

MOT operation can be monitored by two different methods. The straightforward way is to directly observe the blue fluorescence of the MOT transition. A second possibility is to observe the radiation at 657 nm with the help of a photomultiplier[2]. During MOT operation, there is a continuous flux of atoms through the cascade $^1\mathrm{P}_1 \rightarrow {}^1\mathrm{D}_2 \rightarrow {}^3\mathrm{P}_1 \rightarrow {}^1\mathrm{S}_0$ and hence the light at 657 nm is a measure of the number of atoms in the MOT. For calibration purposes the blue fluorescence was directly measured with a power meter[3]; for daily operating purposes, it proved convenient to use the 657 nm light as an indicator of MOT operation. In addition to that, the MOT can be observed by a standard video camera. Figure 4.3 shows a photograph of the MOT during steady state operation.

The number of atoms in the MOT can be deduced from a measurement of the fluorescence of the cloud during steady state operation. The difficulty here consists of estimating the scattering rate per atom; atoms in a MOT experience a light field consisting of 6 independent laser beams with σ^+ and σ^- polarizations. The detuning of the atomic resonance is dependent on the position of the atom in the magnetic field of the trap and on the Doppler shift due to the velocity of the atom. In addition, for samples with a large number of atoms, particles at the center of the trap may experience a lower light intensity because atoms at the outer parts of the cloud scatter away a portion of the light and there may also be the possibility of reabsorption events of scattered photons. One way to address these difficulties in practice is

[2]Hamamatsu R928
[3]LaserMate-Q, Coherent Inc., sensor head “VIS”

to rely on semiempirical models, combining theory and experimental observations [92]. For the purpose of this thesis, an exact calibration of the MOT operation is not necessary and a simple estimate of the atom number is sufficient. Relevant expressions are taken from [63], chapter 2.4.

The scattering rate of photons from the laser beam Γ_{scatt} is equal to the linewidth of the transition times the probability of finding an atom in the excited state ρ_e:

$$\Gamma_{scatt} = \Gamma\rho_e = \Gamma\frac{s_0/2}{1 + s_0 + (2\delta/\Gamma)^2}. \tag{4.1}$$

Here, $s_0 = I/I_s$ denotes the on-resonance saturation parameter and δ is the detuning of the laser. The number of atoms in the excited state N_e can then be calculated from a measurement of the steady state fluorescence of the MOT P_{sf} according to

$$N_e = \frac{P_{sf}}{\hbar\omega_L\Gamma_{scatt}}, \tag{4.2}$$

where ω_L denotes the laser frequency. The probability of finding an atom in the ground state is $\rho_g = 1 - \rho_e$ and the number of atoms in the ground state is given by $N_g = \frac{\rho_g}{\rho_e}N_e$.

During usual MOT operating conditions (oven temperature: 590 °C, $B' = 25\,\mathrm{G/cm}$ along the strong axis), a fluorescence of 600 nW can be observed into a solid angle of $4\pi\times3.32\times10^{-3}$, corresponding to a total fluorescence of the cloud of $P_{sf} = 1.8\times10^{-4}\,\mathrm{W}$ (MOT operation without applying the depumping laser at 423 nm). The laser power in each beam is $P = 6\,\mathrm{mW}$ resulting in a peak intensity of $I = \frac{2P}{\pi w^2} = 7.8\,\mathrm{mW/cm^2}$. The intensity seen by an atom trapped at the center is then six times the intensity of one beam, yielding a saturation parameter $s_0 = 0.78$. The detuning δ of the MOT laser is measured in the following way: A very small part is split from the Zeeman slower beam to be used for absorption imaging (Chapter 6.4). A second AOM blue-detunes this part by 315 MHz to bring it back to resonance. Since the first AOM's detuning for the slower beam is set at 274 MHz, the MOT operates at $\delta = 2\pi\times41\,\mathrm{MHz}$ below resonance. With these parameters, one obtains $\rho_e = 0.053$, $\rho_g = 0.947$, $\Gamma_{scatt} = 11.5\,\mathrm{MHz}$, $N_e = 3.3\times10^7$, $N_g = 6\times10^8$, and a total number of atoms in the MOT of

$$N_{tot} = 6.3\times10^8.$$

The acceleration experienced by an atom in the blue trap can be calculated from the momentum of one photon and the scattering rate. With the above parameters, the acceleration a is given by

$$a = \frac{\hbar k}{m}\Gamma_{scatt} \approx 2.7\times10^5\,\mathrm{m/s^2}. \tag{4.3}$$

It is illustrative to look also at the parameters capture radius r_c and capture velocity v_c of the setup (Figure 4.4). The capture radius is defined as the distance from the center of the trap where for an atom at rest the laser detuning δ is compensated by the Zeeman shift $\omega_Z = \frac{\Delta\mu B}{\hbar}$, with $\Delta\mu = (g_e m_e - g_g m_g)\mu_B$, where $m_{g,e}$ are the magnetic quantum numbers

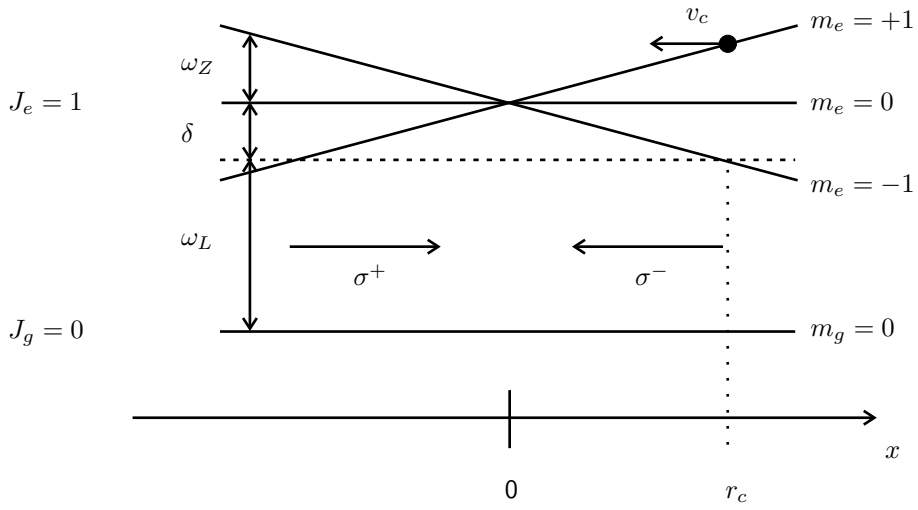

Figure 4.4: Capture radius r_c and capture velocity v_c. ω_L is the laser frequency of the MOT transition. The MOT is located at $x = 0$, the laser beams propagating along the x direction are σ^+/σ^- polarized. See text for further explanation.

and $g_{g,e}$ are the Landé g-factors of the ground and excited state. For the given transition $^1\mathrm{S}_0 \rightarrow {}^1\mathrm{P}_1$, the values are $m_g = 0$, $m_e = 1$, and $g_e = 1$. The capture radius along the weak axis is of interest since this is the direction of incoming atoms from the Zeeman slower. Under standard operating conditions of $I_{MOT} = 3\,\mathrm{A}$ and a corresponding magnetic field gradient $B' = 12.5\,\mathrm{G/cm}$ (Table A.4), the capture radius is given by

$$r_c = \delta \frac{\hbar}{\mu_B} \frac{1}{B'} = 8\,\mathrm{mm}, \tag{4.4}$$

which corresponds roughly to the area illuminated by the laser beams.

The capture velocity is determined by the following consideration: At the edge of the illuminated area the maximum Doppler shift $\omega_D = kv$ of an incoming atom that can be compensated is equal to the sum of the laser detuning δ and the Zeeman detuning ω_Z. Here, $k = 2\pi/\lambda$ denotes the wave number of the laser light and v is the velocity of the atom. Thus, at r_c, $\omega_D = 2\omega_Z$ and

$$v_c = \frac{2\mu_B B' r_c}{\hbar k} \approx 12\,\mathrm{m/s}. \tag{4.5}$$

Loading and decay of the trap is shown in Figure 4.5. The loading of the trap is initiated by simultaneously turning on the Zeeman slower and MOT laser beams at $t = 0$ (Figure 4.5(a) and Figure 4.5(c)). To monitor the decay of the trap, the flux of atoms into the MOT is effectively stopped by blocking the Zeeman slower laser beam; at an average thermal velocity of 670 m/s at 590 °C, only a very tiny fraction of atoms moves slower than the capture velocity v_c and can still be trapped. Figure 4.5(b) and Figure 4.5(d) show measurements of the trap

decay. In (a) and (b), the loading and decay is monitored without applying the depumping laser at 430 nm. (c) and (d) show the corresponding curves while the depumper is turned on. Loading and decay times, as well as atom number in the trap, are significantly increased when adding the light at 430 nm because a part of the atoms lost to the metastable state can be recycled into the MOT. The effective population of the metastable state is illustrated by these measurements.

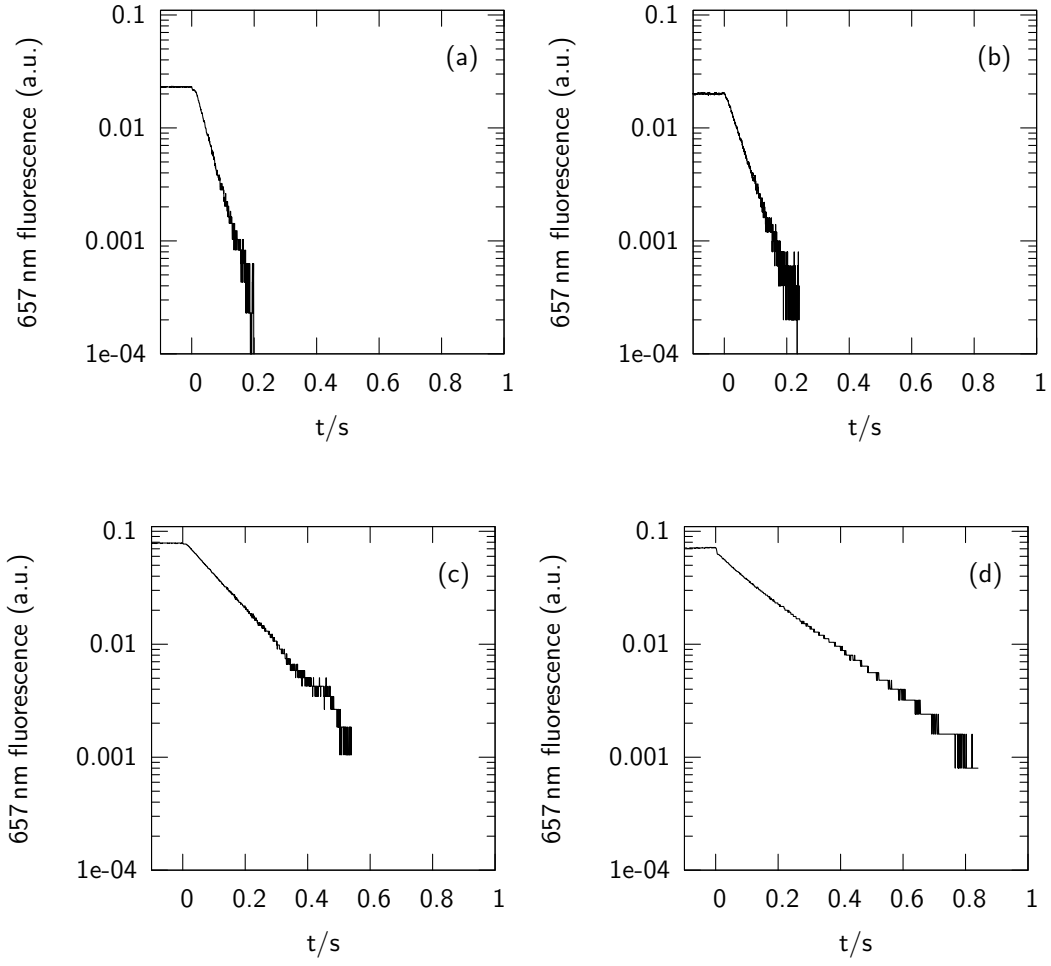

Figure 4.5: Loading and decay of the MOT at 423 nm monitored by the fluorescence at 657 nm. The loading curves (a) and (c) show $N_\infty - N(t)$; the decay curves (b) and (d) display $N(t)$. a) Loading of the trap with time constant $\tau = 47\,\text{ms}$. b) Decay of the trap with $\tau = 53\,\text{ms}$. In c) and d) the depumping beam at 430 nm is continuously applied during operation to transfer the $^3\text{P}_2$ population immediately back to the ground state. The loading time is now $\tau = 144\,\text{ms}$ (c) and the trap lifetime is increased by a factor of four to $\tau = 198\,\text{ms}$ (d). Note the significant increase in trap population by a factor of 3.5 when applying light at 430 nm. The trap lifetime in (d) is still significantly below the vacuum limited lifetime of 4 s (Chapter 6) because applying the laser at 430 nm cannot completely close the loss channel into the metastable state: The time scale for the decay $^1\text{D}_2 \rightarrow {}^3\text{P}_2$ is $\tau = 10\,\text{ms}$ such that a fraction of $^1\text{D}_2$ atoms can escape the volume illuminated by the laser at 430 nm ($1/e^2$ beam radius: $w = 2\,\text{mm}$) before decaying to the metastable state.

5

Magneto-optical Trap at 1978 nm

The setup of the magneto-optical trap at 1978 nm was previously realized and described in [45–47]. This Chapter describes the system as it is set up after the move to the new lab and characterizes the MOT. The MOT is realized, as in the case of the blue MOT and in contrast to the previous setup, with 6 independent laser beams (i.e., no retro-reflected beams are used). Larger optical access than in the previous setup permits the use of larger beams; the maximum beam radius that could be used is, however, limited by the laser power at hand.

The second MOT uses a transition that builds on the metastable $^3\mathrm{P}_2$ state. This transition $^3\mathrm{P}_2 \rightarrow {}^3\mathrm{D}_3$ at 1978 nm has several interesting features that make it well suited for laser cooling and a few drawbacks that are mainly of a technical nature. Among its desirable aspects are its narrow linewidth of $\Gamma = 2\pi \times 130\,\mathrm{kHz}$ [66] and the low photon energy due to its long wavelength. The Doppler temperature for this transition is $T_D = 3.1\,\mu\mathrm{K}$, and the magnetic sub-structure of the ground state could lead to reaching sub-Doppler temperatures by polarization gradient cooling [21, 24, 58]. The recoil limit of this transition is $T_r = 121\,\mathrm{nK}$. In addition, it is a closed transition, so there is no need for any repumping lasers that reinsert lost atoms back into the cooling cycle.

The use of this transition is complicated by the need of a rather sophisticated laser system. The infrared radiation is generated by a series of lasers: A commercially available laser at 532 nm[1] is used to pump a home-made Ti:Sapph laser [101], which in turn is used to pump another home-made Tm:YAG laser [78] (cf. Chapter 2). The Tm:YAG laser needs to be well

[1] Verdi V5, Coherent Inc.

stabilized to an atomic reference. Working with the infrared light is complicated by the fact that there are hardly any appropriate detectors available. InGaAs photodiodes can be used to detect small intensities as in the laser stabilization setup. For higher intensities, we used a PbS photoresistor that is biased with 60 V; light entering the detector needs to be switched with a mechanical chopper[2] to generate an AC readout. For an absolute measurement, this readout needs to be calibrated by comparing it to a known laser power measurement. Measurements of DC powers larger than a few mW were made with a thermal power meter[3]. Thermally sensitive foil that changes its color when heated by infrared radiation can be used to detect laser beams in the mW range but fails when one has to work with minute powers as, e.g., in the setup of 1-dim Doppler cooling (Section 6.5). For beam waist adjustment (e.g. when setting up a telescope) we had to do repeated measurements using the PbS detector and cutting through the beam using a razor blade. The beam waist can then be determined by fitting an integrated Gaussian (i.e., an error function) to the measured beam profile. Beam direction alignment can be done by superimposing a guide beam that is visible to the eye. For this purpose, we used a separate He:Ne laser (632.8 nm) and also a small part of the output of the Verdi V5 (532 nm).

The MOT at 1978 nm operates simultaneously with the MOT at 423 nm since it captures the flux of metastable atoms from the blue MOT. Hence, both traps share the same magnetic field, which is optimized for the blue trap and for capturing atoms from the Zeeman slower. Since the linewidth of the infrared transition is about 260 times narrower than the width of the blue transition, it has to be power broadened to realize an appropriate capture radius and capture velocity (cf. Figure 4.4). r_c can be calculated in analogy to (4.4). An atom at rest at position r_c undergoes primarily σ^- transitions and hence ends up in the state with $m_g = -2$, whereas an atom at r_c moving with a velocity around v_c towards the center is optically pumped towards the $m_g = +2$ state. Figure 5.1 shows the Zeeman levels of the infrared MOT transition and their relative transition strengths. The laser power in each MOT beam is 1.5 mW and the beam waist is 5 mm resulting in a peak intensity of 3.8 mW/cm^2. The saturation intensity of the transition is 2.2 µW/cm^2; the saturation parameter for the given experimental situation is thus $s_0 \approx 1700$ and the power broadened linewidth is $\Gamma' = \Gamma\sqrt{1+s_0} = 2\pi \times 5.4\,\mathrm{Mhz}$. For an atom in the $m_g = -2$ state undergoing a σ^- transition, the Zeeman detuning is $\omega_Z = \frac{\mu_B B}{\hbar}$ and the capture radius is given by the same expression as for the blue MOT (4.4). The detuning of the infrared MOT is estimated to be $\delta = \Gamma'/2$ since we attempt to minimize the temperature of the atoms. The capture radius is then given by

$$r_c = \frac{\Gamma'}{2}\frac{\hbar}{\mu_B}\frac{1}{B'} = 1.5\,\mathrm{mm}. \tag{5.1}$$

The force on the atoms in the infrared MOT is considerably smaller than in the blue MOT because the infrared photons carry only about a fifth of the momentum of the blue

[2]Thorlabs MC1000

[3]Thorlabs D10MM, amplified by Thorlabs Metermate

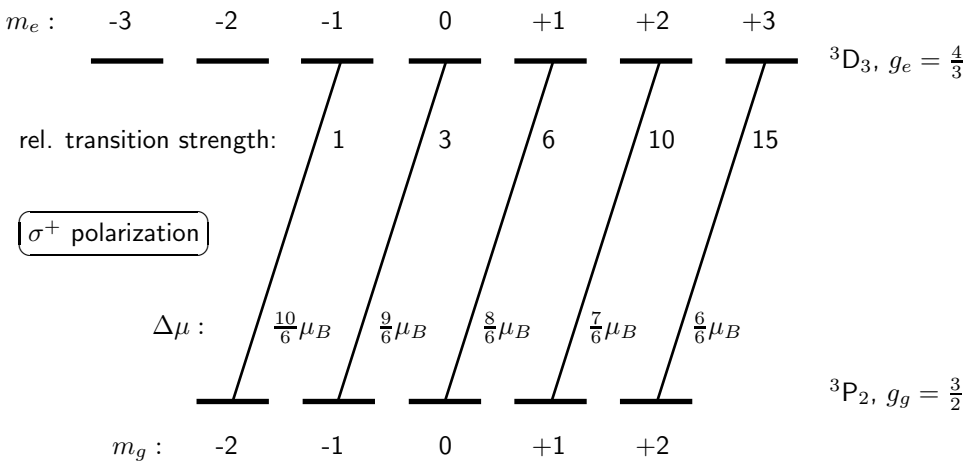

Figure 5.1: Zeeman levels of the $^3\mathrm{P}_2 \rightarrow {}^3\mathrm{D}_3$ transition (1978 nm). $m_{g,e}$ are the magnetic quantum numbers of the ground and excited state; $g_{g,e}$ are their respective Landé g factors. The differences between the magnetic moments of the excited and the ground state are calculated according to $\Delta\mu = (m_e g_e - m_g g_g)\mu_B$. The values for $\Delta\mu$ and the relative transition strengths given are for σ^+ polarized light. The corresponding numbers for σ^- polarization can be obtained by multiplying the magnetic quantum numbers with -1.

photons and the scattering rate is much smaller. Since we strongly saturate the transition, the scattering rate is half the linewidth $\Gamma_{scatt} = \Gamma/2$ and the acceleration experienced by an atom in resonance is $a \approx 4 \times 10^3\,\mathrm{m/s^2}$ according to (4.3).

Atoms that enter the MOT region are decelerated over a distance of at most $2r_c$. The maximum velocity that can still be captured can then be calculated from kinetic theory and is given by

$$v_c = \sqrt{2a \times 2r_c} \approx 5\,\mathrm{m/s}. \tag{5.2}$$

The operation of the infrared MOT is monitored indirectly by optically pumping the atoms from $^3\mathrm{P}_2$ to $^3\mathrm{P}_1$ and then observing the burst of light at 657 nm of the decay back to the ground state (cf. Figure 4.2). The atoms are optically pumped from $^3\mathrm{P}_2$ to $^3\mathrm{P}_1$ by a pulse of light at 430 nm that drives the transition $^3\mathrm{P}_2$ (4s4p) $\rightarrow$ $^3\mathrm{P}_2$ (4p4p). Atoms in the upper $^3\mathrm{P}_2$ state decay to $^3\mathrm{P}_1$ with a branching ratio of about 1:3. With a linewidth of $\Gamma = 2\pi \times 21.6\,\mathrm{MHz}$ of the $^3\mathrm{P}_2$ (4s4p) $\rightarrow$ $^3\mathrm{P}_2$ (4p4p) transition, the average time for the optical pumping process to $^3\mathrm{P}_1$ is about 80 ns. The area under the depumping peak of 657 nm is a measure of the population of the metastable $^3\mathrm{P}_2$ state. Figure 5.2 shows a typical signal of the photomultiplier tube[4] that records the fluorescence at 657 nm. Before $t = -10\,\mathrm{ms}$ the laser beams of the Zeeman slower, the blue MOT, and the infrared MOT had been turned on for $> 1\,\mathrm{s}$ to ensure that the infrared MOT is fully loaded. The blue MOT has reached a steady

[4]Hamamatsu R928

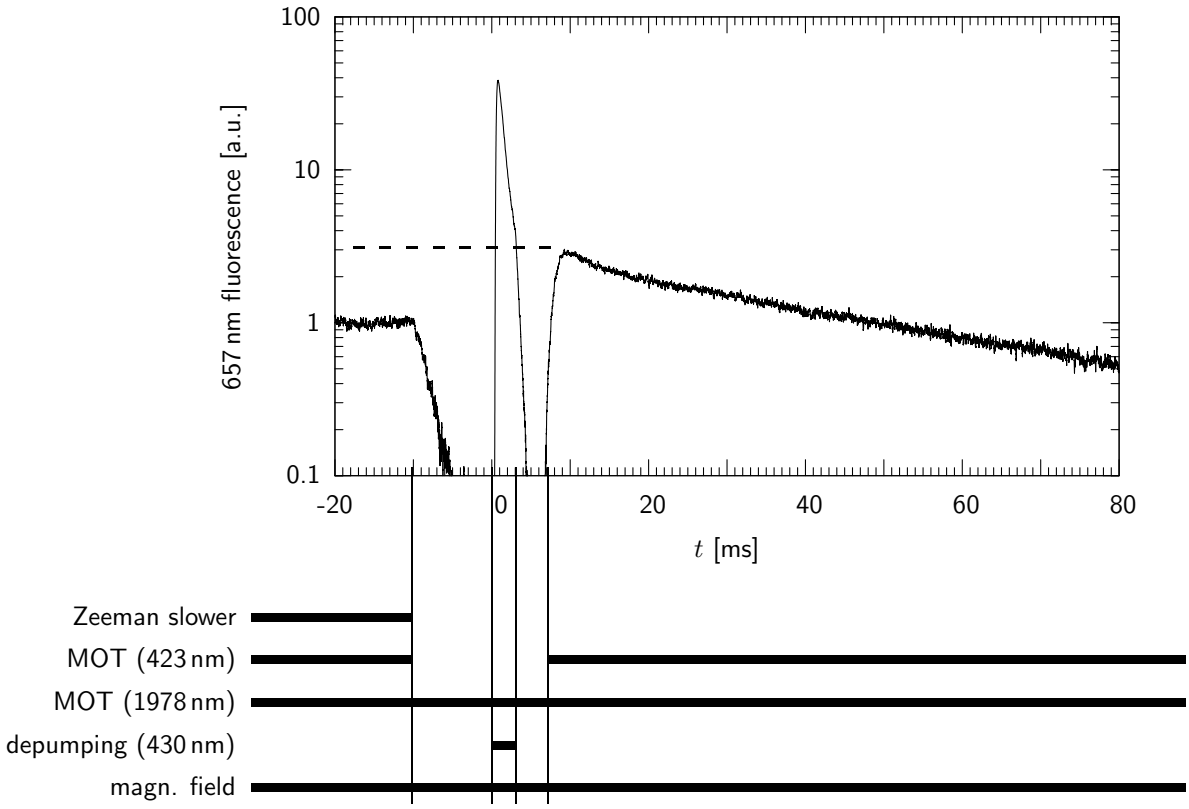

Figure 5.2: Depumping and recapture peak of the infrared MOT. The horizontal lines indicate which parts of the setup are turned on. See text for further explanation

state, which can be seen from the constant level of red fluorescence. At $t = -10\,\text{ms}$, the laser beams of the blue MOT and the Zeeman slower are turned off and the red fluorescence dies out in accordance with the lifetime of the $^1D_2$ state ($\tau \approx 3.3\,\text{ms}$). The population of the infrared MOT is probed at $t = 0$ by applying a 3 ms pulse of light at 430 nm resulting in an intense burst of red fluorescence. The metastable atoms that have decayed to the ground state can now be recaptured in the blue MOT by turning on the blue MOT laser beam at $t = 7\,\text{ms}$. Note that the red fluorescence of the recapture peak is about 3 times the steady state fluorescence level of the blue MOT, indicating that the infrared MOT population is about 3 times the blue MOT population:

$$N \approx 2 \times 10^9.$$

The red fluorescence after the recapture dies out in accordance with the lifetime of the blue MOT of $\tau = 53\,\text{ms}$ (there is no further loading since the Zeeman slower laser is turned off).

The number of atoms in the infrared MOT can be maximized by optimizing the flux of metastable atoms into the MOT region. The flux, in turn, depends on the spatial overlap of the two traps. By balancing the power in each dimension of the blue MOT, the spatial overlap

can be adjusted. We used the height of the recapture peak as an indicator while adjusting the power in the MOT beams. The flux of atoms into the MOT can also be increased by using laser beams of a larger diameter to extend the capture radius. A setting with a beam waist of 12 mm was tried but produced an ensemble with a smaller number of atoms. Obviously, at such a large beam diameter, the linewidth cannot be sufficiently power-broadened due to the limited laser power.

A direct measurement of the number of atoms in the infrared MOT by observing the steady state fluorescence proved very difficult. The total steady state fluorescence of the trap in the case of high saturation is $P = N\hbar\omega_L\Gamma_{scatt} = 8.2 \times 10^{-5}$ W. The detection solid angle in the setup is limited to $4\pi \times 3.32 \times 10^{-3}$; the corresponding power that needs to be detected is 270 nW. This small power is drowned out by the large background of infrared photons in the chamber. One stage of spatial filtering by a small aperture did not block enough background radiation and a more sophisticated optical setup would be needed for detection.

The temperature of the atoms in the infrared MOT was determined in experiments with the previous setup at the former location of the ILP: A light carpet was positioned a few mm below the MOT and the temperature was measured by a time-of-flight method. As the atoms are released from the trap, they fall through the light carpet and the spatial extension of the cloud (and, hence, the temperature) can be inferred from a photomultiplier signal that records the fluorescence induced by the light carpet [50]. The temperature of the infrared MOT was determined to be 180 µK; it can be reduced by optimizing the operating parameters: The linewidth is reduced by decreasing the saturation parameter. At the same time, the magnetic field and the detuning need to be ramped down to maintain a sufficient capture radius. We achieved a minimum temperature of about 20 µK. A slightly different approach modeled the population of the MOT with a bimodal distribution. An inner region where polarization gradient cooling is active is surrounded by a larger cloud of atoms that are simply Doppler cooled. The temperature of the colder inner region was determined to be 22 µK by a recapture experiment [47].

6

Magnetic Trapping of Metastable Calcium

6.1 Loading a magnetic trap from the 1978 nm MOT

Starting point for the loading of the magnetic trap is the atomic sample prepared in the MOT at 1978 nm as described in Chapter 5. The atoms are transferred by switching off the light beams that form the MOT, thereby subjecting them to the trapping potential formed by the quadrupole field generated by the MOT coils. In an alternative approach to loading the trap, the cooling stage of the MOT at 1978 nm is omitted and the $^3P_2$ atoms that are produced through the radiative decay cascade of the $^1P_1$ state of the MOT at 423 nm are directly captured in the magnetic field [50]. A detailed study of different trap loading techniques can be found in [59]. The method of applying the additional cooling and trapping stage of the MOT at 1978 nm was chosen for all experiments presented in this thesis because it yields colder atomic samples that also exceed those of direct loading by about an order of magnitude in atom number.

Magnetically captured $^3P_2$ atoms are detected in complete analogy to Chapter 5: A depumping pulse at 430 nm is applied and the red fluorescence of the decay of the $^3P_1$ state is monitored. The ratio of the areas under the depumping peaks of metastable atoms stored in the magnetic and magneto-optic traps is an indicator of the transfer efficiency to the magnetic trap. Figure 6.1 shows two depumping peaks; in a) the MOT loading time is set at 800 ms, then the atoms are stored in the MOT for another 50 ms without further loading and the depumping pulse is applied. In b) the MOT is loaded for 800 ms and then the laser is shut

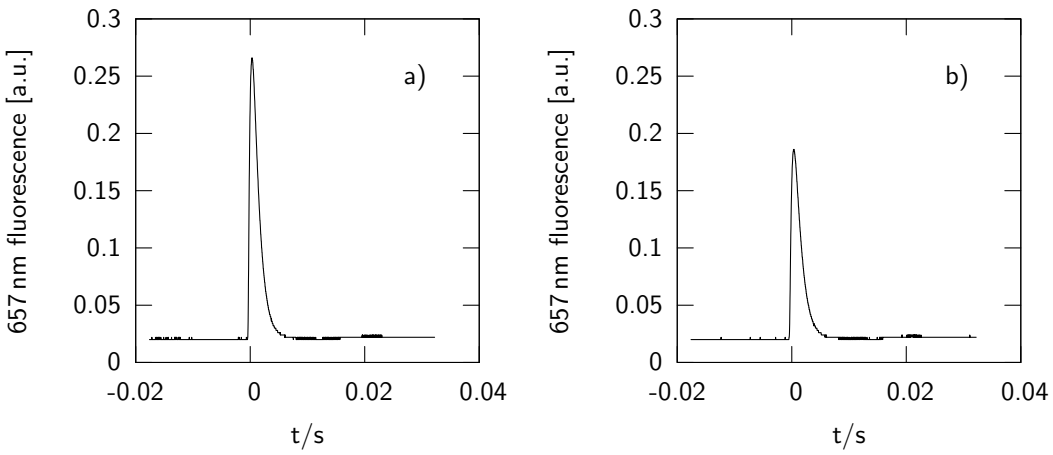

Figure 6.1: Transfer efficiency MOT at 1978 nm → magnetic trap. a) Depumping peak of atoms stored in the MOT at 1978 nm. b) Depumping peak of magnetically trapped atoms. The area under the peak is a measure of the number of trapped atoms. Comparing both areas yields a value for the transfer efficiency of about 75%

off, thereby transferring the atoms to the magnetic trap. After a waiting period of 50 ms to ensure that all untrapped atoms have left the trapping volume, the depumping pulse is applied. Typical transfer efficiencies in our setup are about 75%.

The magnetic trap formed by the quadrupole coils of the MOT has several disadvantages: First, because of its quadrupole configuration, it exhibits a point of zero magnetic field at its center. An atom passing through this area can experience a change in the direction of the magnetic field that is fast compared to its Larmor frequency. In such a case, transitions between Zeeman sub-levels can occur ("Majorana transitions"), leaving the atom in an untrapped state [8, 26, 61, 80, 84]. Second, because of the relatively large geometric dimensions of the MOT coils (cf. Appendix A.1), steep trapping potentials to achieve high sample compressions are hard to realize. As an example, a current of 12 A would be needed to generate a field of 100 G/cm. The corresponding energy dissipation of 435 W would heat the coils to temperatures well above any tolerable value, given the requirements of the vacuum chamber (cf. Chapter 3). Third, the switching time of the coils is limited to about 2.5 ms. The limiting factor is their inductivity that is governed by their size and the fact that they are wound on a base of copper. (The base contains one slit across its cross section, however, eddy currents cannot be suppressed completely.) For efficient loading and detection of atom samples, switching times well below that value are needed.

Hence, a trap with a different design is needed to remedy these disadvantages. Prominent examples that were successfully applied in a number of experiments are: The Ioffe-Pritchard (IP) trap [39, 77] and a number of variations of the IP scheme [7], among others: the cloverleaf

trap [64], the QUIC (quadrupole and Ioffe configuration) trap [38], and the baseball trap [68]. The IP trap and its variations use a magnetostatic field configuration to achieve a stable field minimum with $B \neq 0$. Other approaches use an oscillating field to create an effective field minimum (TOP (time orbiting potential) trap [72]), or prevent the atoms from entering the region of zero magnetic field: A blue-detuned laser is tightly focused on the point of zero field, thereby creating a repulsive potential that overlaps the magnetic trapping potential [25]. Switching times and currents that are required to operate these traps mainly depend on the chosen geometry of the setup. Generally, smaller trap geometries require smaller currents and result in smaller inductances and, hence, in faster switching times. Factors that limit the miniaturization of the traps are, e.g., the need of good optical access to the traps and atom sample sizes. However, for some atomic species, a drastic miniaturization could be achieved ("micro traps" or "atom chips" [14, 81]).

The experiments presented in this thesis were conducted in a QUIC trap. It is fairly easy to build (only three coils), dissipates little power (here: max. $\approx 20\,\mathrm{W}$), provides a strong confinement of the atoms (here: maximum curvature $\approx 4000\,\mathrm{G/cm^2}$), offers good optical access, and can be loaded fairly easily with cold atoms.

6.2 Transferring atoms between traps

The miniaturization of the magnetic trap is incompatible with the requirements of a MOT because the dimensions of the trap coils are on the order of the dimension of the laser beam diameters of the MOT. Thus, the magnetic trap is set up at a distance of 25 mm from the MOT and the atoms need to be transferred after loading the initial magnetic trap formed by the MOT coils. The transport is accomplished by moving the actual trapping potential over a certain distance [41]. The principal idea is as follows: Consider two pairs of quadrupole coils displaced by a small distance with respect to each other; by gradually decreasing the current in one pair and simultaneously increasing the current in the other one, the quadrupole potential moves from the first pair of coils to the second one. In the experiment, we employ three sets of coils: the MOT coils, the quadrupole coils of the QUIC trap, and an additional pair of transfer coils in between (see Figure 6.2(a) for a schema and Figure 6.2(b) for a picture of the assembly). To prevent any heating of the sample, the geometry and the aspect ratio of the potential should ideally remain unchanged during the transport. The magnetic fields generated by the currents in the different coils were simulated using the software BiotSavart (by Ripplon Software Inc.). Perfect preservation of the potential geometry cannot be achieved due to the different dimensions of the coils, however, the transfer can be accomplished with fairly little distortions. Figure 6.5 shows plots of the potential during transfer; the corresponding currents are displayed in Figure 6.3 and the area that is used for the potential plots is shown in Figure 6.4. The atoms are transported to the position of the center of the quadrupole

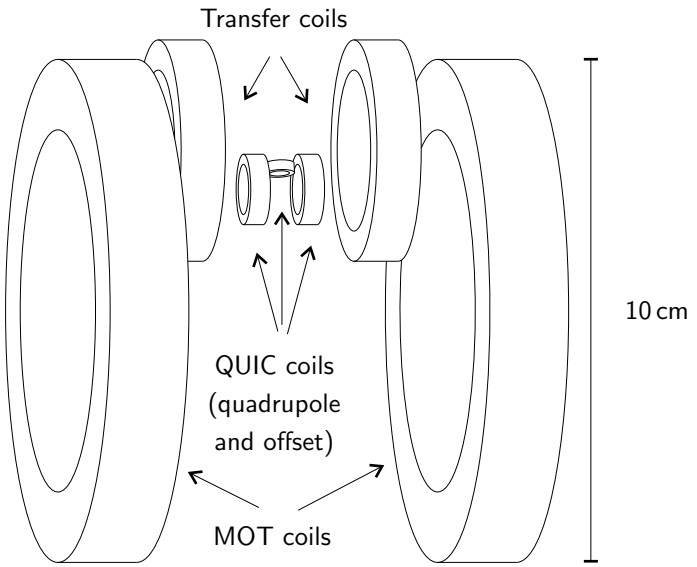

(a)

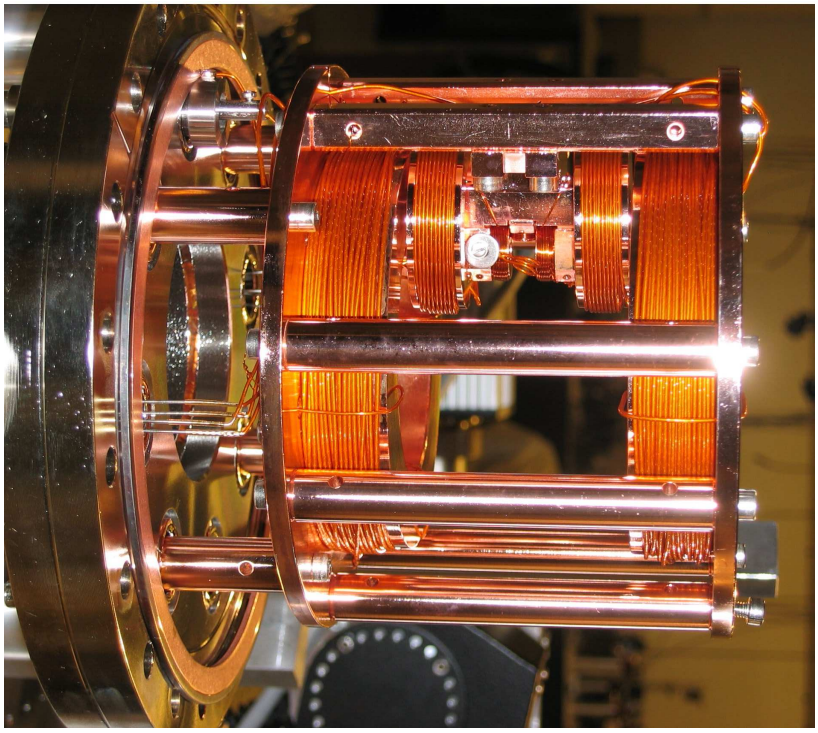

(b)

Figure 6.2: Magnetic field coils. (a) Schema of the configuration. The picture shows only the dimensions of the windings and omits the bases of the coils. (b) Photograph of the field coils before moving it into the vacuum chamber. The wires are wound on copper bases that can be cooled to remove heat during operation.

field of the QUIC trap. Then the currents in the MOT and transfer coils are simultaneously ramped down (in 15 ms) as the current in the quadrupole coils of the QUIC trap is ramped up, thereby trapping the atoms in the magnetic quadrupole field of the QUIC trap. An increase of compression of the sample by a factor of 2.8 was already introduced during transport to increase the density of the sample. The compression is further increased by a factor of 2.5 while ramping up the QUIC quadrupole coils, resulting in a compression of a factor of 7.

The time allowed for compressing the sample is larger than an oscillation period of the atoms; the resulting adiabatic heating can be estimated in the following way: The atoms move in a central potential, hence the angular momentum $L = mvr$ is a constant of motion. By equating the centripetal force with the magnetic force on the atoms, we can derive an expression for the kinetic energy of an atom as a function of the field gradient:

$$\begin{aligned} & \frac{mv^2}{r} = \mu \frac{\mathrm{d}B}{\mathrm{d}r} \\ \Leftrightarrow \quad & v^2 = \frac{L}{m^2 v} \mu \frac{\mathrm{d}B}{\mathrm{d}r} \\ \Leftrightarrow \quad & v^2 = \left(\frac{L\mu}{m^2} \frac{\mathrm{d}B}{\mathrm{d}r} \right)^{2/3} \propto \left(\frac{\mathrm{d}B}{\mathrm{d}r} \right)^{2/3} . \end{aligned} \tag{6.1}$$

Here, m denotes the atomic mass, μ the magnetic moment, B the magnetic field, v the velocity, and r the distance to the center of the trap. The kinetic energy of the atoms is proportional to $\left(\frac{\mathrm{d}B}{\mathrm{d}r}\right)^{2/3}$, hence an increase in temperature by a factor of $7^{2/3} = 3.7$ is expected if the compression is increased by a factor of 7.

Since the quadrupole character of the potential remains throughout the transfer, an estimate of the expected losses by Majorana transitions seems necessary. Losses can be estimated in the following way [72]: The angular velocity ω_T of the change of direction of the magnetic field is $\omega_T = v/b$, where v is the velocity of the atom and b is the minimum distance of the atom as it passes the center of the trap. The Larmor frequency ω_L can be written in terms of the magnetic moment of the atom μ and the magnetic field gradient B' as $\omega_T = \frac{\mu B' b}{\hbar}$. The magnetic moment of an atom in the $^3\mathrm{P}_2$ state is $\mu = g_J m_J \mu_B = 3\mu_B$, where $g_J = 3/2$ is the Landé g factor of the state, μ_B is the Bohr magneton, and we are only concerned with $m_J = +2$ atoms. (Any $m_J = +1$ atoms are either optically pumped to $m_J = +2$ during a later Doppler cooling stage or leave the trap because the trap provides not a sufficient trapping depth for this species.) Majorana losses start to occur when $\omega_T \approx \omega_L \Rightarrow b^2 \approx \frac{v\hbar}{\mu B'}$. Typical values here are $v \approx 1\,\mathrm{m/s}$ for temperatures of the sample of about 1 mK and $B' \approx 100\,\mathrm{G/cm}$ at the end of the transfer, yielding $b \approx 2\,\mu\mathrm{m}$. Typical sample diameters are at $d = 1\,\mathrm{mm}$ orders of magnitude larger than b; nevertheless, on can estimate a loss rate $\frac{N}{\tau_0} = \frac{N}{d^3} v b^2 = \frac{N}{d^2} \frac{\hbar}{m}$ (N: number of particles in the sample, m: atomic mass). Here, the average kinetic energy is taken to be half the maximum potential energy $< \frac{1}{2} m v^2 >= \frac{1}{2} \mu B' d$, yielding a characteristic time constant for the loss of $\tau_0 = 630\,\mathrm{s}$.

Even if this is just a crude estimate, it still shows that Majorana losses should not be a

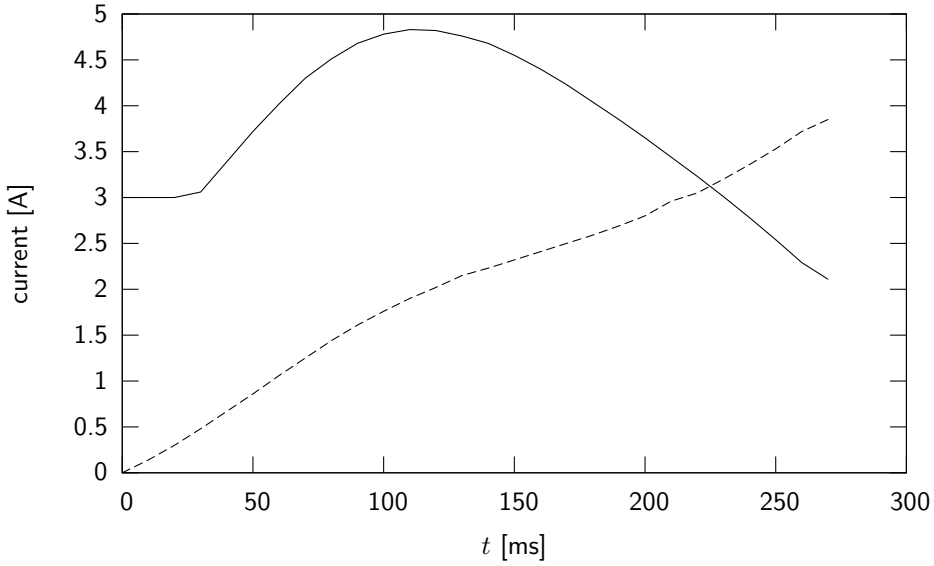

Figure 6.3: Magnetic transfer. The solid line shows the current in the MOT coils during transfer, the dashed line displays the current in the transfer coils. Total transfer time is 270 ms. The corresponding potentials are illustrated in Figure 6.4 and Figure 6.5.

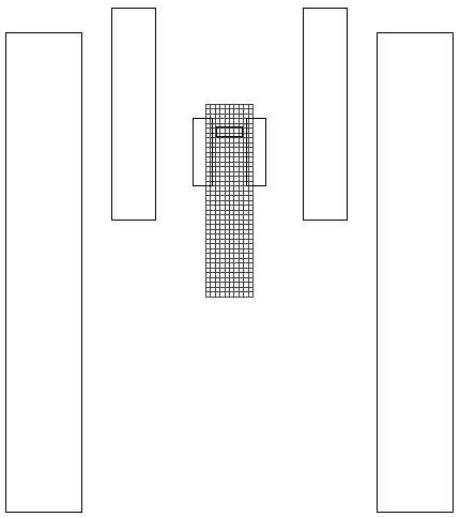

Figure 6.4: The rectangle at the center displays the area in the yz plane of which potential plots during the transfer are shown in Figure 6.5.

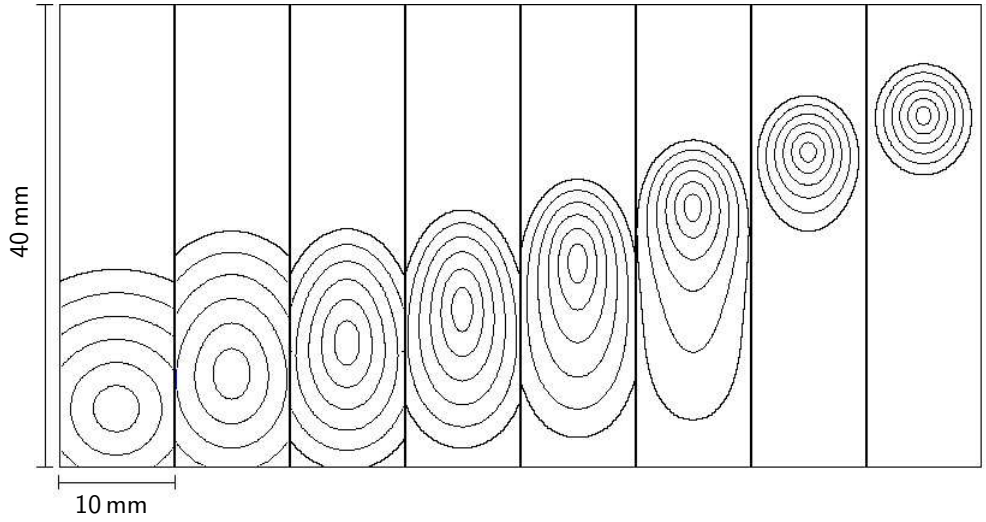

(a)

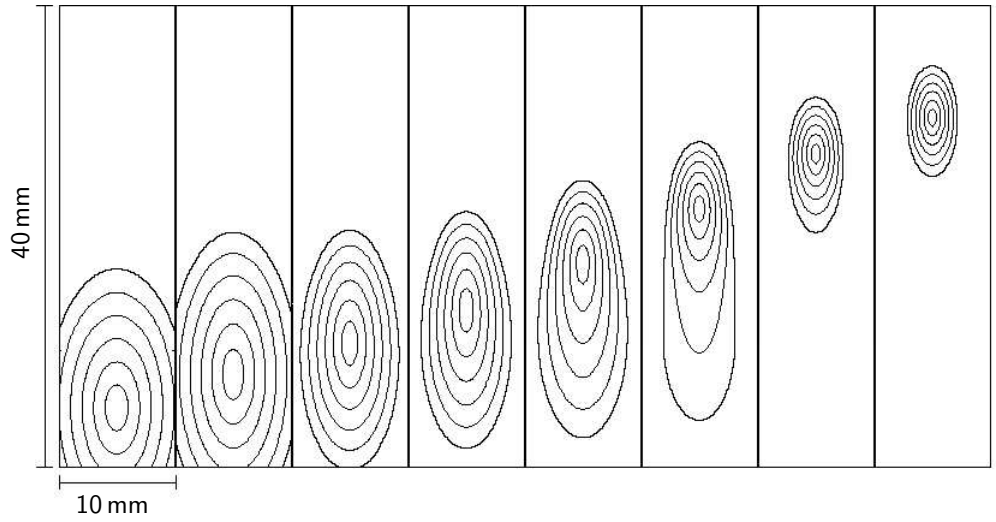

(b)

Figure 6.5: Magnetic transfer: potential plots. (a) shows the potential during transfer in the yz plane. (b) potential in the xy plane (same area as in (a) rotated by 90° about the y axis). Contours correspond to magnetic fields in steps of 2.5 G with zero field at the center. Contours larger than 15 G (outermost contour) are omitted to illustrate the compression of the potential. The 8 plots shown belong to t = 0, 40, 80, 120, 160, 200, 240, 270 ms (left to right).

limiting factor in trapping the sample in a quadrupole field during transfer. Indeed, losses due to collisions with background gas atoms play a far more significant role and limit the lifetime of the sample to about 4 s. The lifetime is determined by γ_{ie}^{-1} in (7.20); Figure 7.1 shows a lifetime measurement for a magnetic field configuration including a magnetic offset field where Majorana transitions should be completely suppressed.

The time allowed for transferring the atoms was chosen to be long compared to the oscillation time in the trap to prevent any additional heating. Oscillation frequencies along the weak axes vary between $\omega/2\pi$ =32 Hz at the beginning and 57 Hz at the end of the transfer before applying the quadrupole field of the QUIC trap (Appendix A.2). The time set for the transfer is 270 ms. The quadrupole field of the QUIC trap is then ramped up in 15 ms; the oscillation frequency along the weak axis rises to 96 Hz. Allowing more time for the final compression step did not result in significantly lower temperatures, however, due to the high inelastic losses at high compressions (Section 7.2), longer compression times would lead to significant particle loss, and, hence, the time for ramping up the quadrupole coils was set to a minimum. Typical atom numbers at the end of the transfer (before loading of the QUIC trap) are 2×10^8 and can be varied by adjusting the temperature of the calcium oven. Atom numbers are obtained by absorption imaging (Section 6.4).

6.3 Loading of the QUIC trap

The QUIC trap is loaded from the quadrupole trap by turning on the current in the small offset coil. While ramping up the current in the offset coil, two additional magnetic field minima develop that are at first only poorly separated by potential barriers. The timing in applying the offset field is crucial in order not to lose the atoms to these additional minima. Figure 6.6 shows a plot of the magnitude of the magnetic field in y direction during application of the offset field.

The strategy chosen here is to apply the offset field quasi instantaneously (i.e., within the limit dictated by the inductance of the system and the power supply) such that no significant number of atoms can escape to the next field minimum. The offset field is set to a value such that the center of the trapping potential coincides with the center of the quadrupole coils of the QUIC trap. Thus, the atoms are loaded into the center of the QUIC trap, thereby minimizing any additional potential energy transfer into the system. The loading efficiency here is about 75%. Different QUIC trap geometries can then be realized by adiabatically varying the currents in the quadrupole and offset coils after the initial loading step. The different trap geometries used in the experiments are summarized in Table A.3.

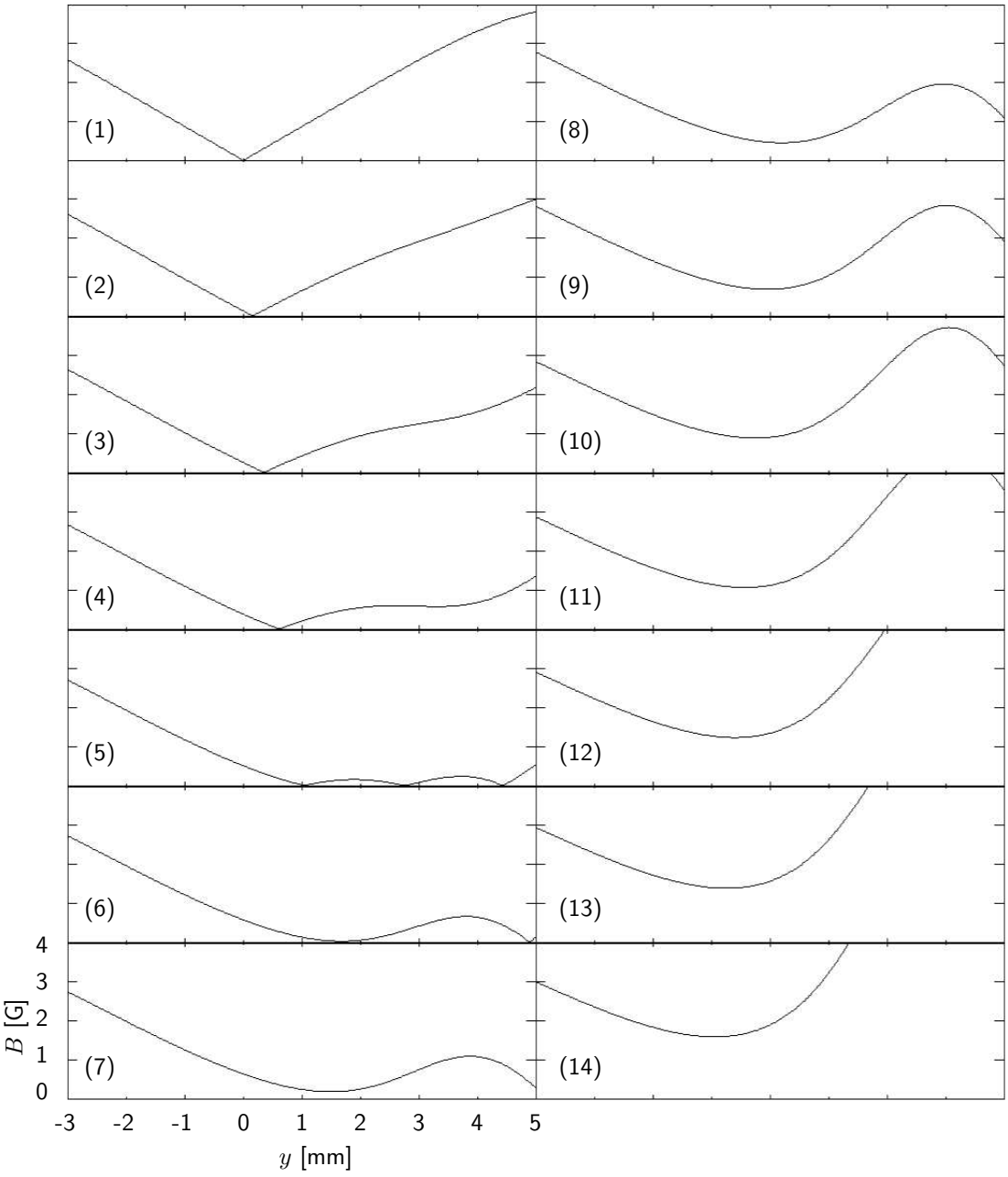

Figure 6.6: Field along the y axis during loading of the QUIC trap from the quadrupole trap. The center of the quadrupole coils is at y=0. The current in the quadrupole coils is set at 1 A, the current in the offset coil is ramped up to 2.5 A. Offset currents of 0, 0.2, 0.4, 0.6, 0.8, 0.9, 1.0, 1.2, 1.4, 1.6, 1.8, 2.0, 2.2, 2.5 A are displayed in graphs (1) to (14). The crucial moment in the loading process can be seen in (5) when two additional minima develop that can cause atoms to be lost from the trap. The center of the loaded QUIC trap finally coincides with the center of the original quadrupole trap.

6.4 Detection of atoms by absorption imaging

The atoms in the magnetic trap are detected by absorption imaging on the principal fluorescence line. The ground state transition $^1S_0 \rightarrow {}^1P_1$ was chosen because, for detection purposes, it can be considered a closed transition with a high scattering rate and because the laser source was already available in the laboratory. The sample is illuminated for 30 µs during absorption imaging. The branching ratio to $^1D_2$ from the excited $^1P_1$ state is $1 : 10^5$ [9] and one absorption - emission cycle takes about 9.2 ns. Hence, even if we consider an atom to be lost completely after branching into $^1D_2$, this process takes on average at least 920 µs. For the infrared transition $^3P_2 \rightarrow {}^3D_3$ at 1978 nm no CCD arrays are available. The transition $^3P_2$ (4s4p) $\rightarrow {}^3P_2$ (4p4p) at 430 nm also offers a high scattering ratio at a linewidth of $\frac{\Gamma}{2\pi}=$ 21.6 MHz but is not closed and on average only ≈ 4 photons are scattered per atom, resulting in poor contrast of the image. The same holds for a transition at 616 nm with a linewidth of $\frac{\Gamma}{2\pi}=$ 11.7 MHz. Spectral line data is taken from [57].

The method of measuring the fluorescence of the $^3P_1 \rightarrow {}^1S_0$ decay after transferring the atoms from $^3P_2$ to $^3P_1$ is not sufficient here because it only contains information about the total number of atoms. For a more detailed analysis, information about the spatial distribution of the atoms is needed to extract values like the number density or temperature; imaging the sample onto the CCD array of a camera is indispensable.

Two effects need to be accounted for when analyzing the images obtained on the ground state transition: After optically pumping the atoms to $^3P_1$, a certain amount of time has to be allowed for the atoms to decay to the ground state. The sample expands during this time and the spatial density distribution has to be corrected. In addition to that, only a certain number of atoms decays during this time such that the actual number of trapped atoms is higher than the detected number. The treatment on how to correct the data can be found in Appendix C.

Two standard and convenient methods of producing images of the atom sample are absorption imaging and phase-contrast imaging. Phase-contrast imaging is the method of choice for very dense samples as, e.g., in the case of a BEC. At maximum optical densities of about 2 (as is the case here), absorption imaging is preferable because of its ease of implementation and image analysis. A good summary of the different techniques is given in [55]; the results relevant to the experiments presented here shall be repeated in brief in the following paragraphs.

The probe beam for absorption imaging propagates along the symmetry axis of the quadrupole coils of the QUIC trap. The shadow of the atom sample is imaged onto a CCD camera[1]. See Figure 6.7 for a sketch of the setup. The beam waist of the probe beam is 4 mm at an intensity of about 70 nW.

[1] PixelFly scientific, PCO computer optics GmbH, resolution 1280x1024 pixels, CCD sensor diagonal 11 mm

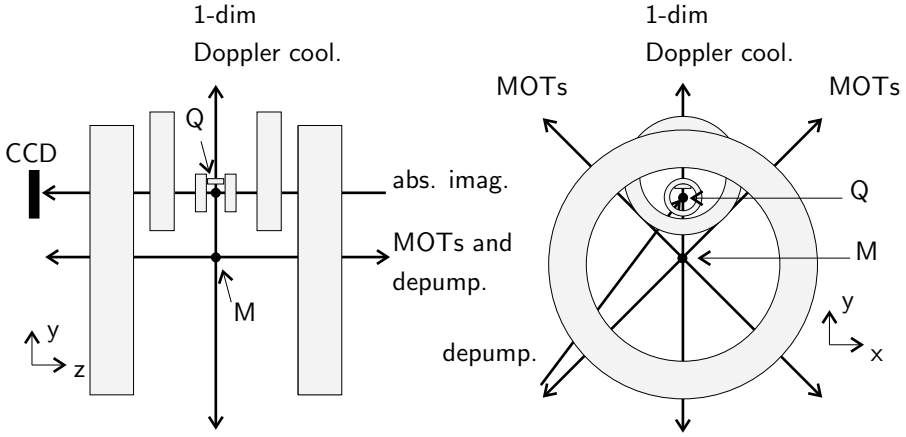

Figure 6.7: Beam configuration. M indicates the location of the MOTs at 423 nm and 1978 nm, Q indicates the location of the QUIC trap. Beams at 423 nm and 1978 nm are superimposed for the two MOTs. Two beams at 430 nm are used for depumping the atoms at positions Q and M. Absorption imaging is done with a light at 423 nm propagating along the symmetry axis of the quadrupole coils of the QUIC trap. For 1-dim Doppler cooling, beams at 1978 nm are used, propagating along the y axis. All beam-shaping and imaging optics are omitted in this figure. The coil outlines represent the volume containing the wire. The bases of the coils are not shown.

The goal of the imaging is to obtain the column number density $\tilde{n}$ along the line of sight (x and y denote the coordinates in the picture):

$$\tilde{n}(x,y) = \int n(x,y,z)dz. \tag{6.2}$$

The column number density is related to the optical density D by

$$D(x,y) = \tilde{n}(x,y)\frac{\sigma_0}{1+\delta^2}, \tag{6.3}$$

with the resonant scattering cross-section $\sigma_0 = \frac{3\lambda^2}{2\pi}$ (for a two level atom) and the detuning δ (in half linewidths). For all experiments presented in this thesis, the probe beam was tuned to the optical resonance, thus $\delta = 0$.

Let us now consider a number density distribution that has a Gaussian shape along the z axis, i.e.,

$$n(\vec{r}) = n_0(x,y)e^{-z^2/\sigma_z^2}, \tag{6.4}$$

where $n_0(x,y)$ is the peak density along the line of sight at a particular coordinate in the picture and σ_z is the $1/e$ radius. Combining (6.2), (6.3), and (6.4), the optical density is then given by

$$D(x,y) = n_0(x,y)\sigma_0\sigma_z\sqrt{\pi}. \tag{6.5}$$

To minimize effects by light scattered after having passed the atom sample and by background light (i.e., light coming from sources other than the probe beam), three images are

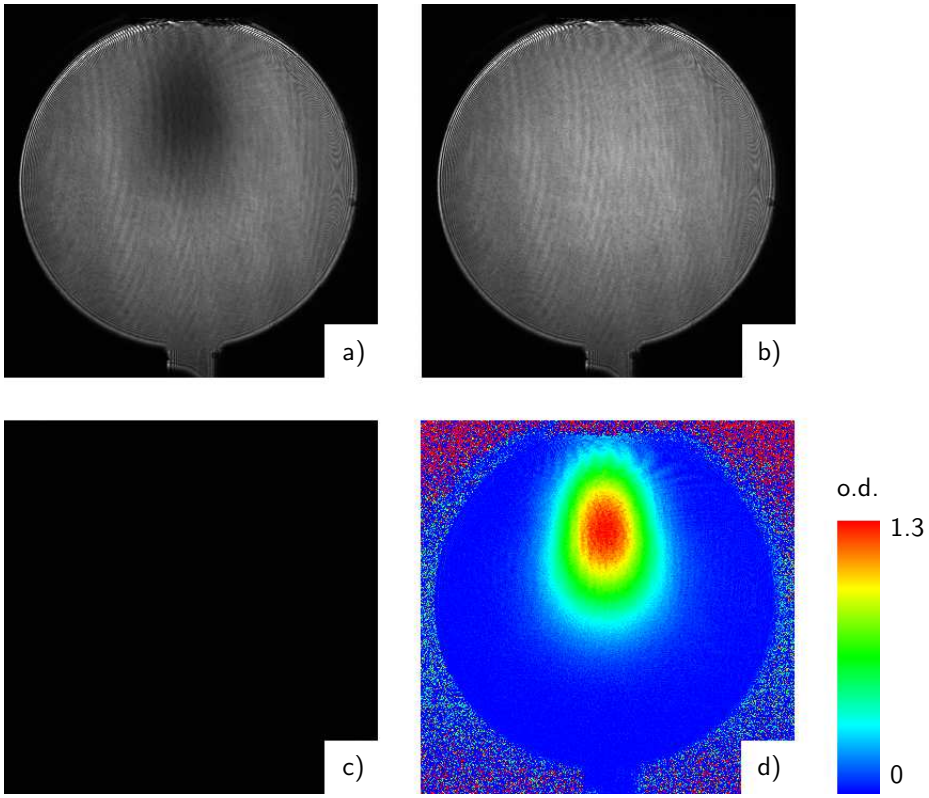

Figure 6.8: a) absorption image I_a, b) bright-field image I_{bf}, c) dark-field image I_{df}, d) transmission image T. The diameter of the illuminated area in the pictures is 6 mm (inner diameter of the base of the QUIC quadrupole coils). The optical density (o.d.) of the atom cloud in this example varies between 0 and 1.3 at its center.

taken and processed to obtain one transmission image: one absorption image with probe beam and atoms (I_a), a bright-field image with probe and without atoms (I_{bf}), and a dark-field image with neither probe beam nor atoms (I_{df}).

To minimize effects caused by intensity fluctuations in the probe beam, the bright-field image is normalized with respect to the absorption image: An area in the images where no atoms are is taken and the bright-field image is multiplied with the quotient of the average intensities in this area. The transmission image T is then calculated as

$$T(x,y) = \frac{I_a(x,y) - I_{df}(x,y)}{I_{bf}(x,y) - I_{df}(x,y)}, \tag{6.6}$$

and the optical density D is obtained by

$$D(x,y) = -ln(T(x,y)). \tag{6.7}$$

Figure 6.8 shows a set of three images that is used to acquire a transmission image.

6.5 1-dim Doppler cooling in the QUIC trap

After transferring the atoms and loading the ensemble into the QUIC trap, an additional 1-dim Doppler cooling stage can be applied to reduce the temperature of the atoms and to bring the ensemble out of thermal equilibrium. We use a standing wave made up of σ^+/σ^+ polarized light propagating along the symmetry axis of the trap (y axis). The intensity and detuning of the light can be adjusted using an AOM. The parameters were experimentally adjusted to yield a maximum cooling rate at a minimum atom loss. The detuning is set 15 MHz below the MOT frequency at 1978 nm. Figure 6.9 compares a Doppler-cooled ensemble to one without application of Doppler cooling. The Doppler cooling beams were applied for a duration of 700 ms; the intensity in the cooling beams is then linearly ramped down to zero in 50 ms while keeping the detuning constant. The beam waist is 2.0 mm and the peak intensity is set to about the saturation intensity of 2.2 µW / cm^2. The trap configuration used is dcool (cf. Table A.3).

The the $1/e$ radius of the Doppler-cooled ensemble is reduced from 1.01 mm to 0.31 mm along the propagation direction of the cooling beams (y) and from 1.37 mm to 0.73 mm perpendicular to it (x). These ensemble sizes correspond to temperatures of $T_{y,cool} = 53\,\mu\text{K}$, $T_y = 561\,\mu\text{K}$, $T_{x,cool} = 404\,\mu\text{K}$, and $T_x = 1410\,\mu\text{K}$, where the subscript "cool" denotes the Doppler-cooled ensembles. Hence, the temperature in y direction could be reduced to 17 times the Doppler temperature of the transition of 3.1 µK.

During application of the Doppler cooling stage, atoms can be lost through depolarizing transitions $m_J \to m_J$ or $m_J \to m_J - 1$; the magnetic field direction is not completely uniform throughout the volume of the standing wave resulting in a nonzero probability for these transitions. However, the 1-dim Doppler cooling stage is applied to a trap with comparatively high offset field of 16 G to provide a good selectivity of the cooling transition. For an ensemble prepared in the $m_J = +2$ state, the π transition is red detuned by $\Delta\omega_Z = \frac{4}{3}\frac{\mu_B}{\hbar}B = 30\,\text{MHz}$ to the σ^+ transition and the σ^- transition is detuned by twice that amount (cf. Figure 5.1). At a natural linewidth of 130 kHz, the excitation probability for these transitions is very small and, thus, atom loss occurs predominantly through two-body collisions (cf. Section 7.2).

For the experiments described in Chapter 7, the duration of the Doppler cooling stage was shortened to 50 ms to reduce the atom loss while still disturbing the thermal equilibrium of the sample. Figure 6.10 compares two ensembles loaded into trap ld4 (cf. Table A.3) with and without previous 1-dim Doppler cooling. 7.6×10^7 atoms are Doppler cooled in trap dcool and subsequently loaded into trap ld4. The average temperature of the sample is 1.2 mK at a peak density of $5 \times 10^{10}\,cm^{-3}$. 1.1×10^8 atoms are loaded into trap ld4 without Doppler cooling (right hand side of the Figure). Here, the average temperature is 2.5 mK and the peak density is $2.9 \times 10^{10}\,cm^{-3}$. The relatively high temperatures in this example can be attributed to the high compression in trap ld4 compared with trap dcool.

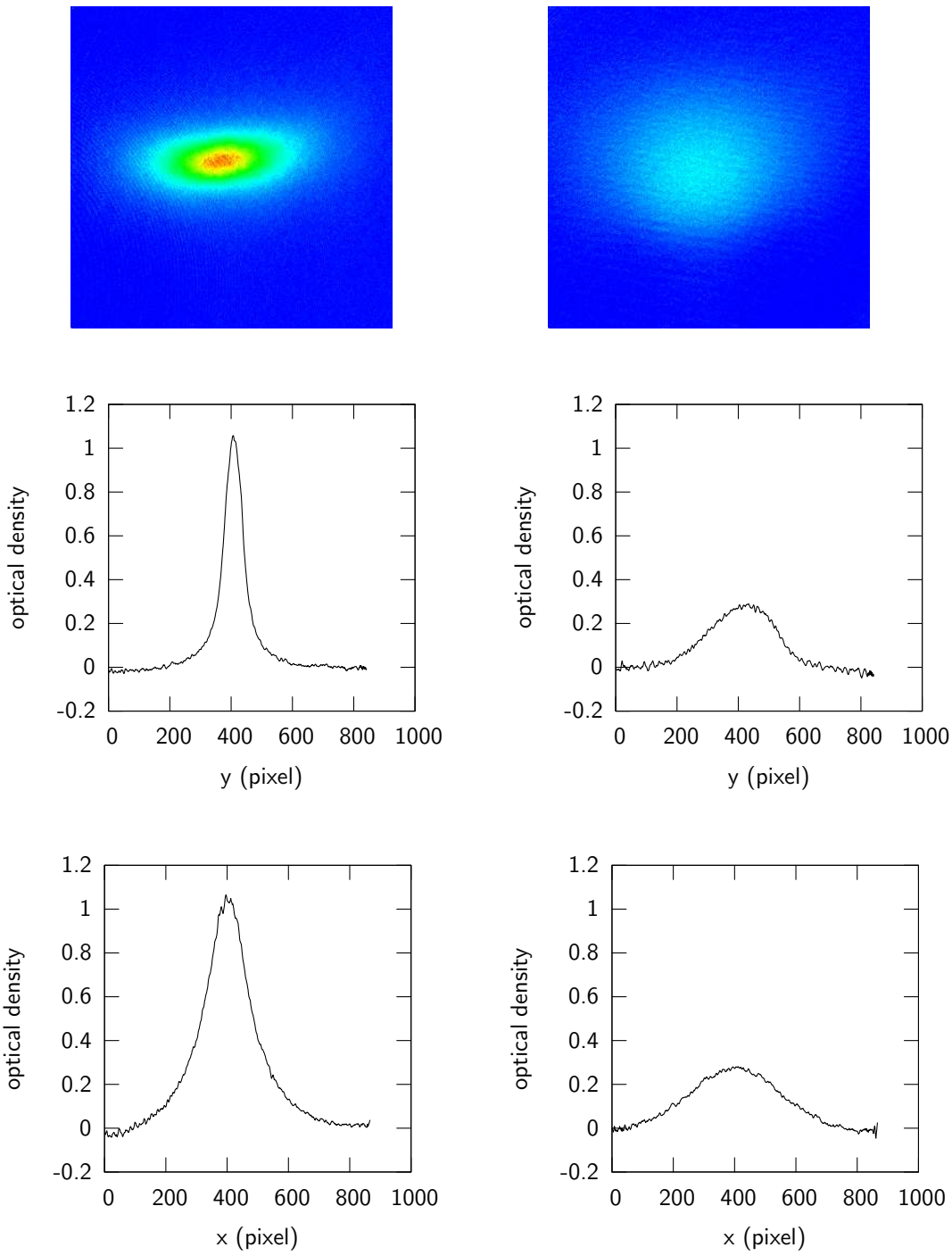

Figure 6.9: 1-dim Doppler cooling, demonstrated in trap dcool (cf. Table A.3). The left hand side of the figure shows an ensemble that was Doppler-cooled for 700 ms with the laser beam intensity set to about the saturation intensity of 2.2 µW/cm^2. The right hand side shows an ensemble after a delay of 700 ms but without Doppler cooling. The atom number in both cases is about 1.2×10^7. Note the significant reduction in size of the sample and the fourfold increase in optical density. The average temperature of the Doppler-cooled ensemble is 290 µK compared to 1130 µK without Doppler cooling. The dimension of the pictures is 2×2 mm^2. One pixel corresponds to 6.84 µm (the traces extend beyond the area displayed in the pictures).

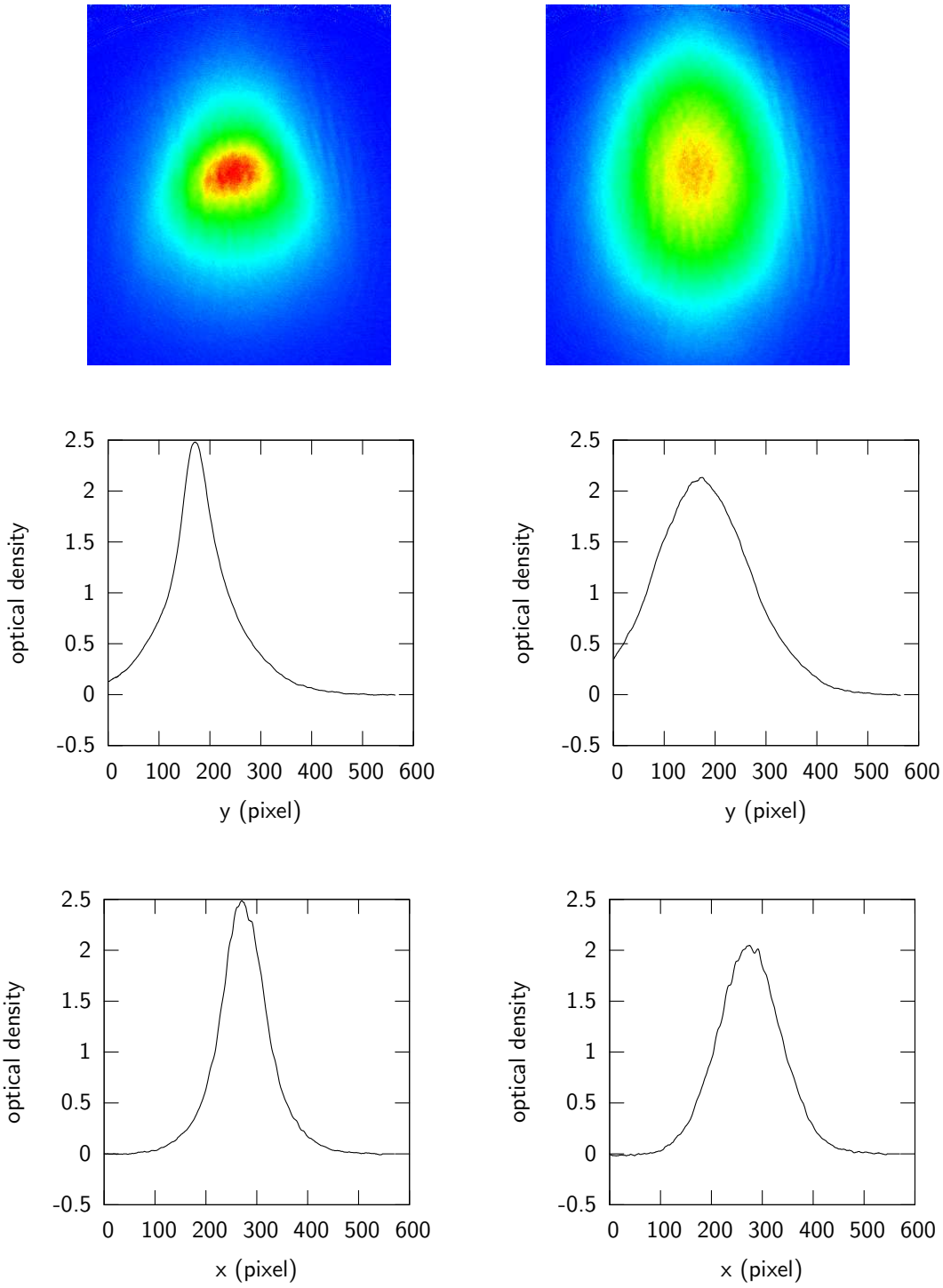

Figure 6.10: 1-dim Doppler cooling as applied in Chapter 7. On the left hand side is an ensemble that was Doppler cooled in trap dcool (cf. Table A.3) for 50 ms and subsequently loaded into trap ld4. The right hand side shows an ensemble that was loaded into ld4 without prior Doppler cooling. The graphs show optical density profiles through the center of the ensembles. The reduction of the sample radius of the Doppler cooled ensemble is evident, as well as the increase in density. The horizontal dimension of the pictures is 3 mm; one pixel corresponds to 9.38 µm (the traces extend beyond the area displayed in the pictures).

7

Results: Elastic and Inelastic Collision Properties

7.1 Elastic collisions

Loading of the QUIC trap and subsequent adjustment of different trap geometries (curvature and aspect ratio) destroys the thermal equilibrium of the sample, an effect that is enhanced if an additional 1-dim Doppler-cooling stage is applied. Elastic collision parameters can now be measured by observing the sample reequilibrate. During such a cross-dimensional relaxation process, the aspect ratio of the sample changes in the following way:

$$\dot{A} = -(A(t) - A_{eq})(\gamma_0 + \gamma_1(t)), \tag{7.1}$$

where A denotes the aspect ratio of the sample with $A = \frac{\sigma_y}{\sigma_x}$. $\sigma_{x,y}$ are the $1/e$ radii of the sample in x and y direction, A_{eq} is the aspect ratio in thermal equilibrium, γ_0 is a constant relaxation rate (e.g. due to ergodic mixing), and $\gamma_1(t)$ is the mean relaxation rate due to elastic collisions [4, 53, 67, 86].

From kinetic theory, the mean relaxation rate can be written in terms of the mean number density of the sample $\bar{n}(t)$, the mean thermal velocity $\bar{v}(t)$, and an effective relaxation cross-section σ_{eff}, which is in turn directly proportional to the elastic collision cross-section:

$$\gamma_1(t) = \sigma_{eff}\bar{n}(t)\bar{v}(t). \tag{7.2}$$

Atom loss occurs predominantly at the center of the trap where the density is highest, hence removing colder atoms from the sample. As a consequence, the temperature of the sample

increases during the trapping time and the density decreases. Thus, the time dependence has to be taken into account when evaluating (7.2). For the temperature range of interest in the experiment (about 500 µK – 2.5 mK), the temperature dependence of σ_{eff} is neglected.

To draw a comparison between theory and measured data, it is useful to formally integrate (7.1):

$$A^*(t) = -\gamma_0 - \frac{\gamma_1(0)}{\bar{n}(0)} n_v^*(t), \tag{7.3}$$

with

$$A^*(t) = \frac{1}{t} ln(\frac{A(t) - A_{eq}}{A(0) - A_{eq}}) \tag{7.4}$$

and

$$n_v^*(t) = \frac{1}{t} \int_0^t \bar{n}(t') \frac{\bar{v}(t')}{\bar{v}(0)} dt'. \tag{7.5}$$

The mean velocity in the sample can be expressed according to the Maxwell distribution as

$$\bar{v}(t) = \sqrt{\frac{8 k_B \bar{T}}{\pi m}}, \tag{7.6}$$

where k_B is Boltzmann's constant, m is the atomic mass, and $\bar{T} = \frac{1}{3}(2T_x + T_y)$ is the average temperature in the sample. Here, the temperature along the line of sight T_z is taken to be equal to T_x, which is justified because the trap shows an approximate rotational symmetry about the y axis. 1-dim Doppler cooling does not disturb this symmetry since it is applied along the y axis.

The temperature can be deduced from the density distribution of the cloud if the shape of the potential φ is known [1]; the density distribution is proportional to $e^{-\frac{\varphi}{k_B T}}$. In the case of a harmonic potential, which in good approximation reflects the situation in the QUIC trap, the temperature is then related to the $1/e$ radii $\sigma_{x,y,z}$ of the sample as

$$k_B T_i = \frac{1}{2} m \omega_i^2 \sigma_i^2, \qquad i \in \{x, y, z\}. \tag{7.7}$$

The quotient of the velocities in (7.5) can now be expressed in terms of σ_x and the aspect ratio A:

$$\begin{aligned}
\frac{\bar{v}(t')}{\bar{v}(0)} &= \sqrt{\frac{\bar{T}(t')}{\bar{T}(0)}} \\
&= \sqrt{\frac{\omega_y^2 \sigma_y^2(t') + 2\omega_x^2 \sigma_x^2(t')}{\omega_y^2 \sigma_y^2(0) + 2\omega_x^2 \sigma_x^2(0)}} \\
&= \sqrt{\frac{\sigma_x^2(t')(\frac{\sigma_y^2(t')}{\sigma_x^2(t')} + 2(\frac{\omega_x}{\omega_y})^2)}{\sigma_x^2(0)(\frac{\sigma_y^2(0)}{\sigma_x^2(0)} + 2(\frac{\omega_x}{\omega_y})^2)}} \\
&= \frac{\sigma_x(t')}{\sigma_x(0)} \sqrt{\frac{A^2(t') + 2A_{eq}^2}{A^2(0) + 2A_{eq}^2}}.
\end{aligned} \tag{7.8}$$

In this derivation, it is used that for large values of t', the sample reaches thermal equilibrium and, hence, $T_x = T_y$, i.e., $\frac{\omega_x^2}{\omega_y^2} = \frac{\sigma_y^2(\infty)}{\sigma_x^2(\infty)} = A_{eq}^2$.

The mean number density $\bar{n}$ is defined as [4]

$$\bar{n} = \frac{\int n^2(\vec{r})d^3r}{\int n(\vec{r})d^3r}. \tag{7.9}$$

When evaluating the integrals in (7.9), the integrations over x and y become discrete sums over the pixels of the CCD camera. $\Delta x \Delta y$ is an area of the sample that is imaged onto one pixel of the CCD chip with Δx and Δy being the respective sides of the rectangle. With (6.4) and (6.5), integrating yields

$$\begin{aligned}\int n^2(\vec{r})d^3r &= \int n_0^2(x,y)e^{-2z^2/\sigma_z^2}dxdydz \\ &= \Delta x \Delta y \sigma_z \sqrt{\pi/2} \sum_{x,y} n_0^2(x,y) \\ &= \frac{\Delta x \Delta y}{\sigma_0^2 \sigma_z \sqrt{2\pi}} \sum_{x,y} D^2(x,y).\end{aligned} \tag{7.10}$$

The second integral in (7.9), which is equal to the total number of particles N, can also be expressed in terms of the optical density D. Using (6.2) and (6.3), it can be written as

$$\begin{aligned}N = \int n(\vec{r})d^3r &= \int \tilde{n}(x,y)dxdy \\ &= \frac{\Delta x \Delta y}{\sigma_0} \sum_{x,y} D^2(x,y).\end{aligned} \tag{7.11}$$

(7.9) then simplifies to

$$\bar{n} = \frac{1}{\sigma_0 \sigma_z \sqrt{2\pi}} \frac{\sum_{x,y} D^2(x,y)}{\sum_{x,y} D(x,y)}. \tag{7.12}$$

The expression for the scaled integrated number density (7.5) finally reads, using (7.8) and (7.12):

$$n_v^*(t) = \frac{1}{t} \frac{1}{\sigma_x(0)\sigma_0\sqrt{2\pi}} \int_0^t \frac{\sigma_x(t')}{\sigma_z(t')} \frac{\sum_{x,y} D^2(x,y)}{\sum_{x,y} D(x,y)} \sqrt{\frac{A^2(t') + 2A_{eq}^2}{A^2(0) + 2A_{eq}^2}} dt' \tag{7.13}$$

The expression $\frac{\sigma_x(t')}{\sigma_z(t')}$ is the aspect ratio of the trap in the xz plane, which is approximately equal to 1 due to the rotational symmetry of the trap about the y axis. All other quantities (time, radii, and optical density) in the equation can directly be measured.

The elastic collision parameter $\beta_e = \frac{\gamma_1(0)}{\bar{n}(0)}$ can now be obtained by plotting A^* vs. n_v^* (cf. Equation (7.3)) and applying a linear fit to the data. Figure 7.1 shows such a plot for the trap configuration ld4. The straight line fit to the data crosses the y axis at ≈ 0, which indicates that ergodic mixing plays a negligible role in the relaxation process of the aspect ratio of the

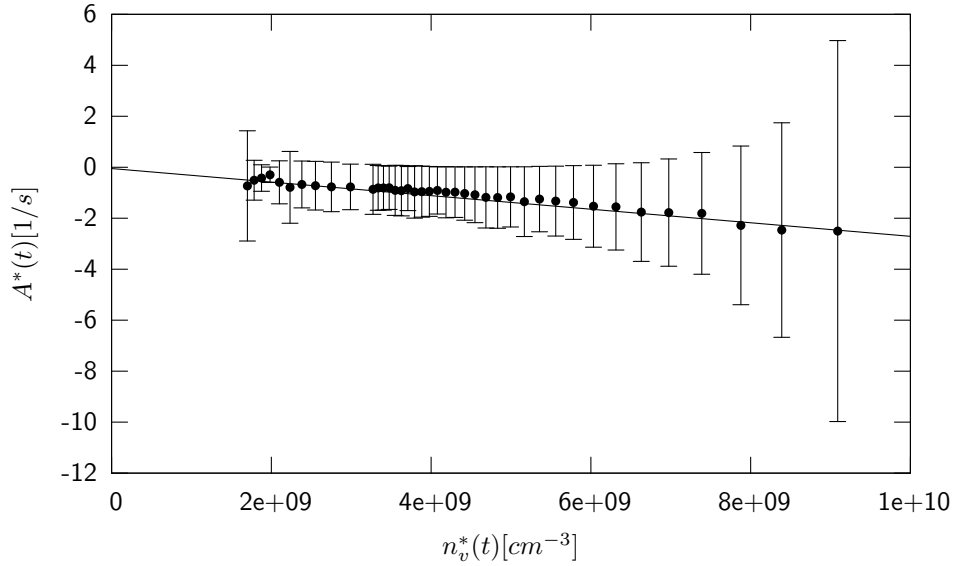

Figure 7.1: Plot of the scaled values $A^*(t)$ vs. $n_v^*(t)$ for trap configuration ld4 without 1-dim Doppler cooling. The solid line shows a fit to the data resulting in $\gamma_0 = 0.05\,s^{-1}$ and an elastic collision parameter $\beta_e(0) = 2.66 \times 10^{-10}\,\frac{cm^3}{s}$.

sample. In the experiment, five different trap configurations (cf. Table A.3) were examined, each with and without application of 1-dim Doppler cooling. The results are summarized in Figure 7.2.

The temperatures associated with the measurements are derived from (7.7). If the magnetic field is of purely harmonic character with a field curvature a and an offset c

$$B(i) = a_i i^2 + c, \qquad i \in \{x, y, z\}, \tag{7.14}$$

the trap frequency ω_i can be written as

$$\omega_i = \frac{2a_i\mu}{m} = \frac{2a_i m_J g_J \mu_B}{m}, \tag{7.15}$$

with the magnetic quantum number m_J and the Landé g factor g_J. For atoms trapped in the $m_J = 2$ state and $g_J = \frac{3}{2}$ for $^3\mathrm{P}_2$ atoms [10], (7.7) becomes

$$T_i = 3a_i\sigma_i^2\frac{\mu_B}{k_B}. \tag{7.16}$$

In [54], thermal relaxation rates in clouds of trapped bosons are calculated from theory. Expressions are derived for the cases of energy-dependent and energy-independent scattering cross-sections. If we identify Γ_T given in the paper with $\gamma_1(0)$, we can derive a theoretical value for the measured parameter β_e. For the case of an energy-independent cross-section (assumption made in (7.2)), Γ_T^{indep} is given by Equation (88) in terms of the peak density of the sample n_0, the elastic collision cross-section σ_{el}, and the mean thermal velocity $\bar{v}$:

$$\Gamma_T^{indep} \simeq 0.189 n_0 \sigma_{el} \bar{v}. \tag{7.17}$$

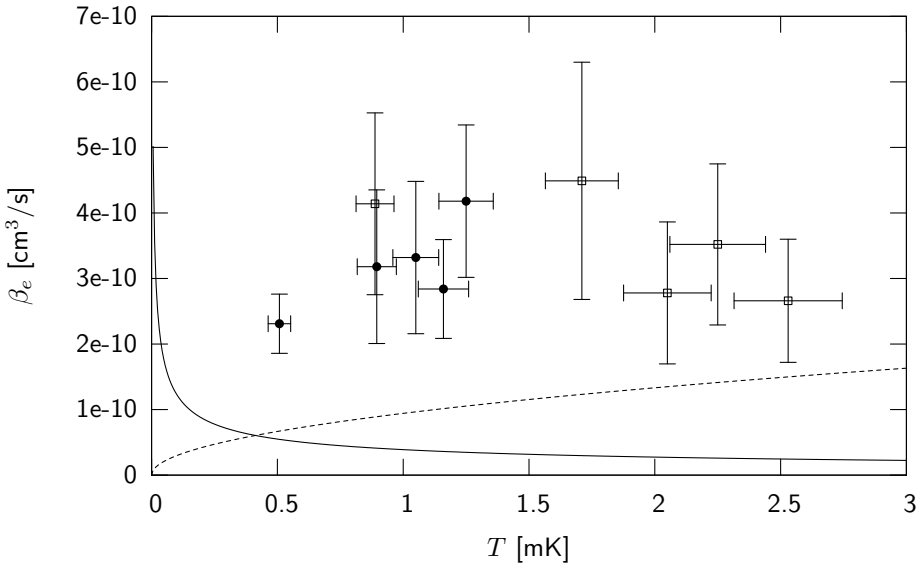

Figure 7.2: Elastic collision parameter β_e plotted vs. initial mean temperature $\bar{T}(0)$. • and □ depict values measured with and without 1-dim Doppler cooling, respectively. The dashed line shows $\beta_{e,theo}^{indep}$ as in (7.18). The solid line is $\beta_{e,theo}^{dep}$ according to (7.19)

.

For a density distribution that is Gaussian in all three dimensions, $n_0 = \sqrt{8}\bar{n}$, and (7.17) yields

$$\beta_{e,theo}^{indep} = \frac{\Gamma_T^{indep}}{\bar{n}} = 0.189\sqrt{8}\sigma_{el}\bar{v}. \tag{7.18}$$

The theoretical value for the elastic collision parameter for energy-independent scattering $\beta_{e,theo}^{indep}$ is plotted as the dashed line in Figure 7.2, using $\sigma_{el} = 2.4 \times 10^{-12} cm^2$, which is taken from [56].

Equation (89) in [54] gives an expression for energy-dependent scattering. It uses the elastic collision cross-section in the unitarity limit for s-wave scattering $\sigma_{el}(u) = \frac{32\pi\hbar^2}{(mu)^2}$, where u is the relative velocity of the collision partners. The theoretical value for the elastic collision parameter for energy-dependent scattering then becomes (solid line in Figure 7.2):

$$\beta_{e,theo}^{dep} = \frac{\Gamma_T^{dep}}{\bar{n}} = 4\sqrt{8}\frac{\hbar^2}{m^2\bar{v}}. \tag{7.19}$$

The measured values are clearly above the theoretical value for s-wave scattering, which is an indication that partial waves of higher order play a significant role in the scattering process. [56] states that partial waves with $L > 6$ play a dominant role, however, the derived value for σ_{el} still seems to underestimate the elastic scattering process. One reason for this discrepancy might be that short range molecular dynamics has not been accounted for in [56].

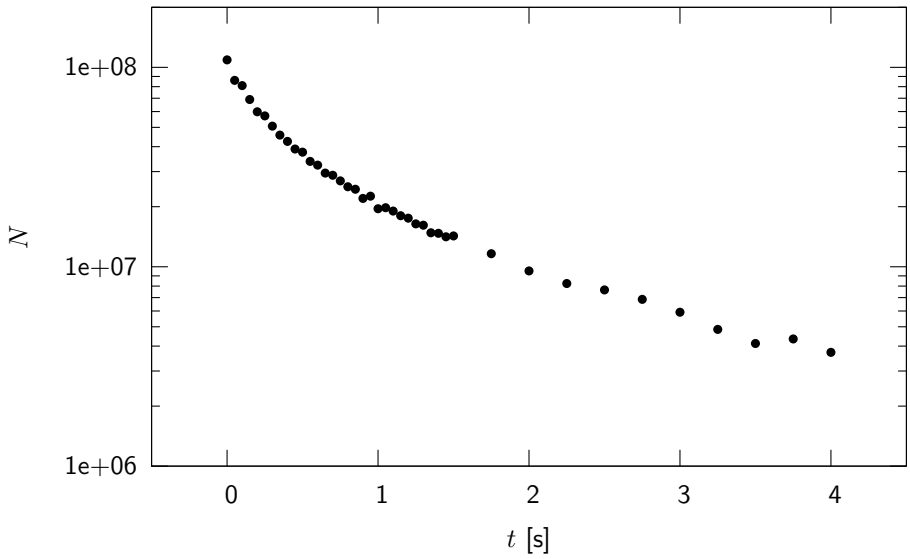

Figure 7.3: Lifetime measurement of atoms trapped in ld4. The nonlinear character of the decay is clearly visible.

7.2 Inelastic collisions

The rate of inelastic binary collisions is investigated by an analysis of the atom losses from the trap. The particle number $N(t)$ in the trap decays according to

$$\dot{N}(t) = -\gamma_{ie}N(t) - \beta_{ie}(t)\frac{N^2(t)}{V_{eff}(t)}, \tag{7.20}$$

where γ_{ie} is the linear decay parameter due to collisions with background gas atoms and $\beta_{ie}(t) = \sigma_{ie}\bar{v}(t)$ is the inelastic two-body loss parameter. σ_{ie} can be identified with the inelastic collision cross-section if both collision partners are lost in the process. As in the case of the elastic collisions, the temperature dependence of the inelastic cross-section is neglected. $V_{eff}(t) = \frac{N(t)}{\bar{n}(t)}$ is the effective trap volume, which can change in time due to heating of the sample. Figure 7.3 shows a measurement of the particle number N in trap ld4 as a function of time. The strongly nonlinear character of the trap decay is clearly visible.

Equation (7.20) can be rewritten as

$$\dot{N}(t) = -\gamma_{ie}N(t) - \sigma_{ie}\bar{n}(t)\bar{v}(t)N(t), \tag{7.21}$$

which is formally identical to (7.1) and can be integrated to

$$N^*(t) = -\gamma_{ie} - \beta_{ie}(0)n_v^*(t), \tag{7.22}$$

with $n_v^*(t)$ as given in (7.13) and

$$N^*(t) = \frac{1}{t}ln(\frac{N(t)}{N(0)}). \tag{7.23}$$

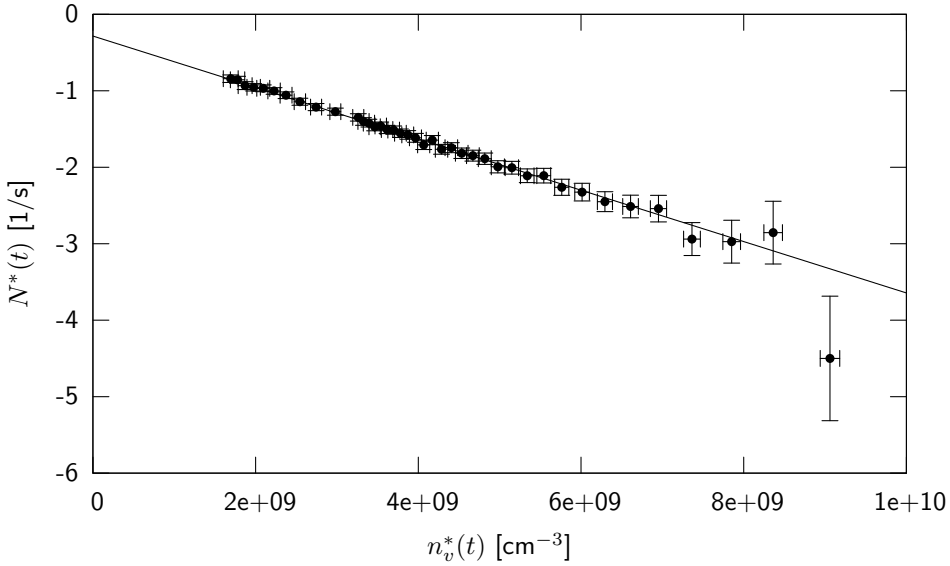

Figure 7.4: Plot of the scaled values $N^*(t)$ vs. $n_v^*(t)$ for trap configuration ld4 without 1-dim Doppler cooling. The solid line shows a fit to the data resulting in a linear decay parameter $\gamma_{ie} = 0.28\,s^{-1}$ and a two-body loss parameter $\beta_{ie}(0) = 3.41\text{e-}10\,\frac{cm^3}{s}$.

The linear decay parameter γ_{ie} and the two-body loss parameter $\beta_{ie}(0)$ are now obtained as the results of a linear fit to a data plot of N^* vs. n_v^*. Figure 7.4 shows a plot corresponding to the trap configuration ld4. 1-dim Doppler cooling was not used for this particular data set.

Figure 7.5 summarizes the measurements of the inelastic collision rates. The same five trap configurations as for the elastic case were used here; for each trap configuration a data point with and without 1-dim Doppler cooling was measured.

7.3 Error analysis and verification of QUIC trap geometry

The various sources of error associated with the measurements shall be discussed here briefly. All the results presented in this Chapter are derived from absorption images. The parameters that are directly taken from these images are σ_x, σ_y, D, and D^2. All numbers concerning the geometry of the trap (cf. Appendix A.1) are obtained through simulations of the magnetic field, which is determined by the current in the quadrupole coils of the QUIC trap I_{quad} and by the current in the offset coil I_{off}. Parameters relevant to the data analysis are the aspect ratio σ_x/σ_z used in (7.13) and the magnetic field curvatures a_i.

To verify that the actual trap geometry agrees with the simulated one, two sets of measurements were carried out. The y position of the minimum of the trap depends on I_{off}/I_{quad}, whereas the value of the offset field for a given ratio of these currents depends on the mag-

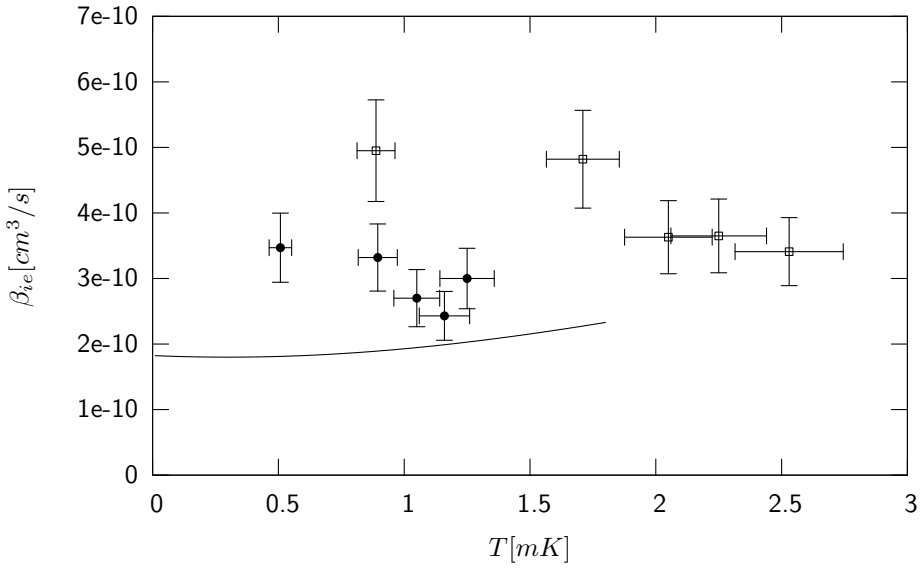

Figure 7.5: Inelastic collision parameter β_{ie} plotted vs. initial mean temperature $\bar{T}(0)$. • and □ depict values measured with and without 1-dim Doppler cooling, respectively. The solid line shows the prediction of the theory of [56] multiplied by a factor of 10. The theory considered the case of a slightly larger magnetic field of 100 G and of a spin polarized ensemble. The discrepancy might be attributed to the fact that spin polarization in the measured ensembles is not perfect, even after application of 1-dim Doppler cooling. Also, the limitation of the treatment to the s-wave entrance channel might not be justified for the temperatures of the measured ensembles.

nitude of the currents. Hence, by measuring the y position and offset field value of the field minimum, the simulation of the trap geometry can be verified.

The y position of the field minimum was determined by taking an absorption image of an ensemble and measuring the position of the center of mass of the cloud. To correct for a shift of the ensemble position due to gravity, the oscillation frequency ω_y of the ensemble in the trap was measured, too. The magnitude of the shift is determined by equating the magnetic force on the atoms in the trap with the gravitational force $m\omega_y^2 y = mg \Leftrightarrow y = g/\omega_y^2$. Typical oscillation frequencies in the examined traps are $\omega_y = 500\,\mathrm{Hz}$ resulting in a gravitational sag of $y = 0.04\,\mathrm{mm}$.

To measure the value of the offset field, a pulse of radio frequency was applied to the sample. The frequency was ramped up from zero to a few 10 MHz; as soon as the radio frequency reaches the Zeeman detuning $\Delta\omega = g_J \Delta m_J \mu_B B/\hbar$ for $\Delta m_J = 1$ at the bottom of the trap, atoms are removed from the ensemble through rf-induced Zeeman transitions. By measuring the frequency at which considerable atom loss starts to occur, the offset field at the center of the trap can be determined.

For both parameters (y position and offset field), the experimental values agree with the simulated ones to within 10%, which was taken to be the systematic error associated with

these two parameters.

The systematic error made in the determination of the $1/e$ radii $\sigma_{x,y}$ mainly comes from distributions that are not perfectly Gaussian. The effect is more serious for σ_y since the distribution deviates more seriously from a perfect Gaussian shape for Doppler-cooled ensembles at very small t. In addition to that, part of one wing of the distribution is obscured by the aperture (cf. Figure 6.9). Systematic errors were estimated to be 3% for σ_x and 10% for σ_y.

Systematic errors in D and D^2 stem from two sources. First, due to the large sample sizes observed in the experiments, a small fraction of atoms is hidden behind the aperture. Second, even though great care was taken to ensure that the absorption laser beam is on resonance, small drifts of the laser system might cause the laser frequency to deviate from resonance. Hence, the optical densities observed might be smaller than the on-resonance density. These effects individually cancel out in $N^*(t)$ but need to be noted in $\frac{\sum D^2}{\sum D}$ in $n_v^*(t)$ and amount to an error of about 10%.

To be able to estimate the random errors, the same data point was measured 100 times during one hour, which is the time span that is characteristic for taking one lifetime measurement of a trap. The random errors are 3% for $\sigma_{x,y}$ and D, and 5% for D^2, with a tendency to increase a bit for samples with small atom numbers.

The noise in the camera was measured by taking absorption images without loading the trap; atom numbers "detected" were $\pm 3 \times 10^5$.

The timing in the experiments is controlled by an independent computer system[1] with a maximum resolution of 25 ns and was taken to be exact.

[1] ADwin-Pro, Processor T9, Jäger GmbH

8

Summary and Perspectives

The main results of the work presented in this thesis are the measurements of the inelastic two-body loss parameter for cold collisions and the determination of the cross-dimensional relaxation parameter that is attributed to elastic collisions. The values for the elastic and inelastic rates were found to be roughly equal to each other at about $3 \times 10^{-10}\,\mathrm{cm}^3/\mathrm{s}$. In the experiment, a temperature range between 0.5 mK and 2.5 mK could be addressed at magnetic fields between 2 G and 10 G. The experimental findings confirm the general character of the theory developed in [56]; the observed elastic collision rates are clearly above the unitarity limit for s-wave scattering. Thus, the asserted multi-channel character of cold collisions between metastable calcium atoms in a magnetic trap can be confirmed.

The observed inelastic rates are even one order of magnitude above the theoretical predictions, a fact that might be attributed to several reasons. The magnetic fields considered in the theoretical study cover the range between 100 G and 1500 G. No data were given for lower fields but calculated values showed a tendency to increase as the magnetic field becomes smaller than 100 G. Our magnetic trap, unfortunately, does not permit to adjust offset fields in the 100 G range because the heat that is dissipated in the magnetic coils would then by far exceed the capabilities of the cooling system.

Then, the theory gave quantitative values only for the case of a spin-polarized ensemble in the $m_J = +2$ state. For mixed spin ensembles, it is asserted that short range interactions between two colliding atoms become increasingly significant, whereas the theoretical treatment is limited to long range interactions. For mixed spin collisions, the rates are es-

timated to be higher that the values given for spin-polarized ensembles. The experiments were conducted with ensembles that might contain a residual fraction of $m_J = +1$ atoms. The degree of spin-polarization after loading the magnetic trap from the MOT is not known and can be additionally reduced by collisions or Majorana transitions during the transfer. The spin-polarization is expected to be restored by 1-dim Doppler cooling in the QUIC trap; some depolarizing transitions might occur, however, due to the fact that the magnetic field direction is not completely uniform over the total volume covered by the cooling beams. In addition, inelastic collisions will increase the $m_J = +1$ population in the sample. So far, a Stern-Gerlach experiment to check the spin orientation of the sample could not be conducted because the geometry of the vacuum chamber does not offer the optical access needed for it.

The most important conclusion to be drawn from these experiments is that it will not be possible to reach Bose-Einstein condensation of metastable calcium in a magnetic trap. We have tried applying resonant radio frequency, thereby removing the most energetic atoms from the trap but could not detect any significant increase in phase space density. The situation with calcium is thus similar to previous experiences with Cs, where evaporative cooling was attempted in a magnetic trap but failed to reach the quantum degenerate regime [85, 91]. A spectacular success came with the use of an optical dipole trap instead of a magnetic trap and the realization of BEC in the group of Grimm in 2003 [95]. Subsequently, this technique was applied in a few other experiments. Most notably, the species of condensed elements has thus be extended by chromium [43] and ytterbium [90]. The situation with chromium is somewhat similar to the one with calcium in the sense that it possesses an even larger magnetic moment ($6\mu_B$) and dipolar relaxation processes inhibit evaporative cooling in a magnetic trap [52]. Ytterbium is a very interesting example in the context of this thesis, too, because it also possesses two valence electrons and, thus, an electronic structure similar to the one of calcium with singlet and triplet states. BEC of ytterbium was achieved in the $^1S_0$ ground state.

We have recently set up an optical dipole trap and made first measurements. The dipole trap is formed by a laser at 532 nm[1]. The beam can be split in two branches to set up a crossed trap; each branch can be controlled independently with an AOM[2]. For an excellent review of the basics of trapping neutral particles in strongly focused laser beams see [32]. In short, the trapping potential U_{dip} is given by the sum of the light shifts due to the trapping laser between the trapped state and all potential excited states:

$$U_{dip}(\vec{r}) = \frac{3\pi c^2}{2} I(\vec{r}) \sum_i \frac{\Gamma_i c_i^2}{\omega_{i,0}\delta_i}, \tag{8.1}$$

where c is the velocity of light, $I(\vec{r})$ is the intensity profile of the trapping laser, Γ_i is the spontaneous decay rate of the excited level, c_i is the Clebsch-Gordan coefficient of the transition,

[1] Verdi V5, Coherent Inc.

[2] Crystal Technology 3080-125, center frequency 80 MHz

$\omega_{i,0}$ is the on-resonance frequency of the transition, δ_i is the detuning between the trapping laser, and the resonance frequency and the sum runs over all possible transitions i.

At present, we have set up a trap consisting of one single laser beam propagating along the axis of the quadrupole coils of the QUIC trap (z direction, cf. Figure A.1). The laser beam is focused at the center of the QUIC trap with a $1/e^2$ beam radius of $w = 17\,\mu\text{m}$. The power at the location of the atoms is 3 W. With these parameters, the trap depth for calcium atoms in the $^1S_0$ state is 610 µK, with by far the largest contribution of 542 µK stemming from the $^1S_0 \rightarrow {}^1P_1$ transition at 423 nm. (The data necessary to evaluate Equation (8.1) is taken from [57].)

The following procedure was used to load atoms in the dipole trap: At first, the 1-dim Doppler cooling stage was applied for 200 ms in trap dcool (cf. Section 6.5 and Table A.3). Then the intensity of the trapping laser was ramped up while the 1-dim Doppler cooling was still active. Next, the Doppler cooling beams were switched off and a 500 µs long pulse of light at 430 nm was applied to optically pump the atoms to the ground state. Figure 8.1 shows an absorption picture of the ground state dipole trap. The laser for absorption imaging is superimposed on the trapping laser and, hence, one sees a pancake shaped projection of the trapped atoms. Great care needs to be taken to shield the dipole trap from any stray light at 423 nm since absorption quickly heats the sample and causes excessive trap loss. Figure 8.2 shows a lifetime measurement of the trap.

At this point, we succeeded to load only moderate numbers of about 2×10^4 atoms into the trap. The trap lifetime is $\tau = 5\,\text{s}$, which is in accordance with the vacuum conditions of 2×10^{-10} mbar. The limiting factors for the loading of the dipole trap are the temperature and the density of the atoms after the Doppler cooling in the QUIC trap. The ensemble that was used in the measurements in Figure 8.2 had an average temperature of 400 µK after the Doppler cooling. We have achieved lower average temperatures at different cooling parameters but these were also accompanied with a decrease in atom number. At temperatures that are two orders of magnitude above the Doppler limit of 3 µK of the infrared transition, there clearly is a need for a better understanding of the process. An increase of the trap volume by using a larger waist of the trapping laser could also help to load more atoms into the trap, the trade-off here is a reduction in the trap depth if the total power in the laser remains constant and ultimately starting with lower temperature samples seems inevitable.

As another possibility to load the dipole trap, it could be set up at the location of the MOT instead of the QUIC. Here again, a better understanding of the Doppler cooling processes would be needed to reduce the temperature of the samples in the MOT. In previous experiments, we have tried to optimize the temperature by reducing the saturation of the $^3P_2 \rightarrow {}^3D_3$ transition and at the same time adjusting the magnetic field and the detuning in the MOT beams. The lowest temperature that was achieved (20 µK) was accompanied by a heavy loss of atoms. One reason for this might have been insufficient frequency stability of

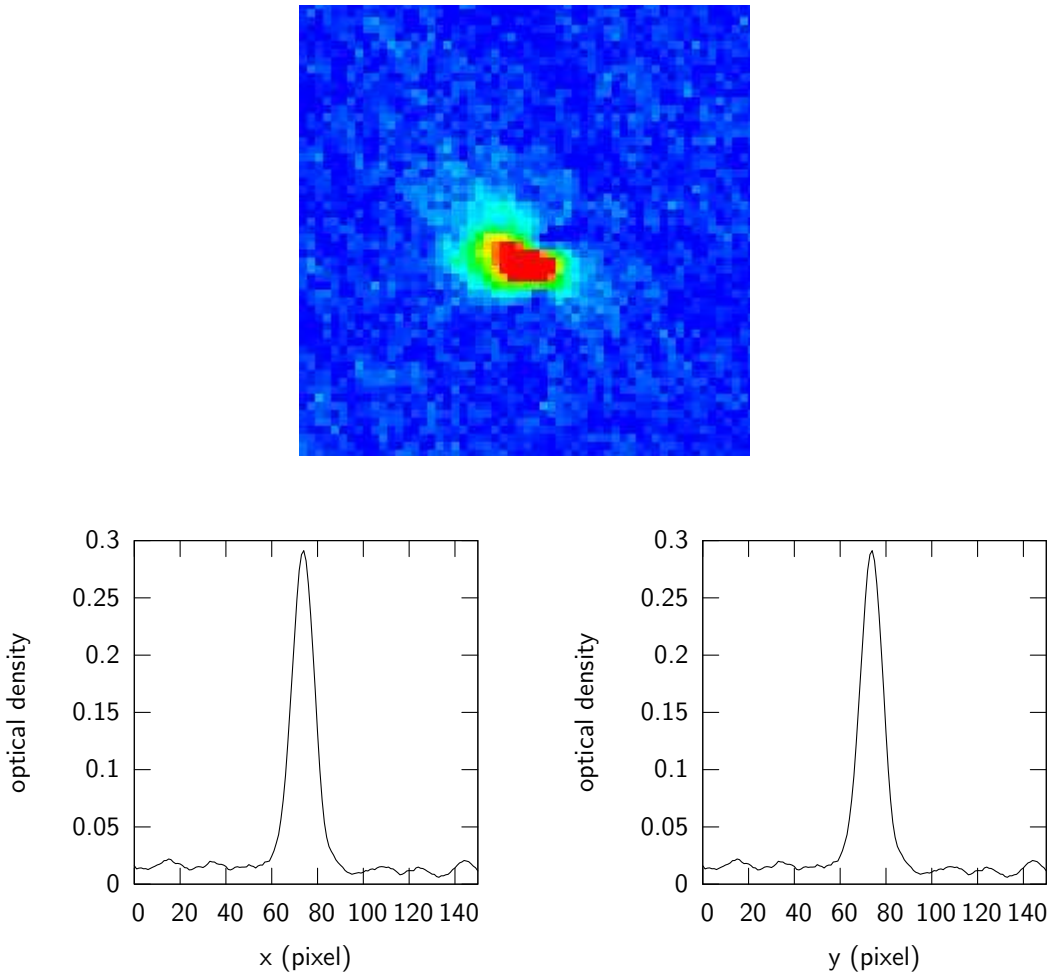

Figure 8.1: Absorption imaging picture of the dipole trap. The picture area is 0.38×0.38 mm^2. The graphs display the optical density of the cloud along lines through the center of the cloud; the traces extend beyond the area displayed in the picture. One pixel corresponds to 6.84 µm.

the Tm:YAG laser and we are currently working on improving this part of the setup.

Another interesting option is to load the dipole trap with metastable $^3P_2$ atoms instead of pumping them to the ground state. Figure 8.3 shows a schema of the dipole trap potential for π polarization of the trapping laser. The interesting feature here is that the sum of all light shifts yields a trapping potential for $m_J = \pm 2$ and $m_J = \pm 1$ atoms, whereas the potential is repulsive for $m_J = 0$ atoms. Such a feature could eventually be exploited for an evaporative cooling scheme in an optical trap. A first attempt to load metastable atoms into the trap, however, failed. The experimental procedure we used was similar to the one used in loading the trap with ground state atoms, only the depumping pulse was omitted. The trap decayed on a time scale of 100 ms and the mechanism for this trap loss remains to be understood. It could possibly be attributed to interactions between the magnetic field and the large magnetic

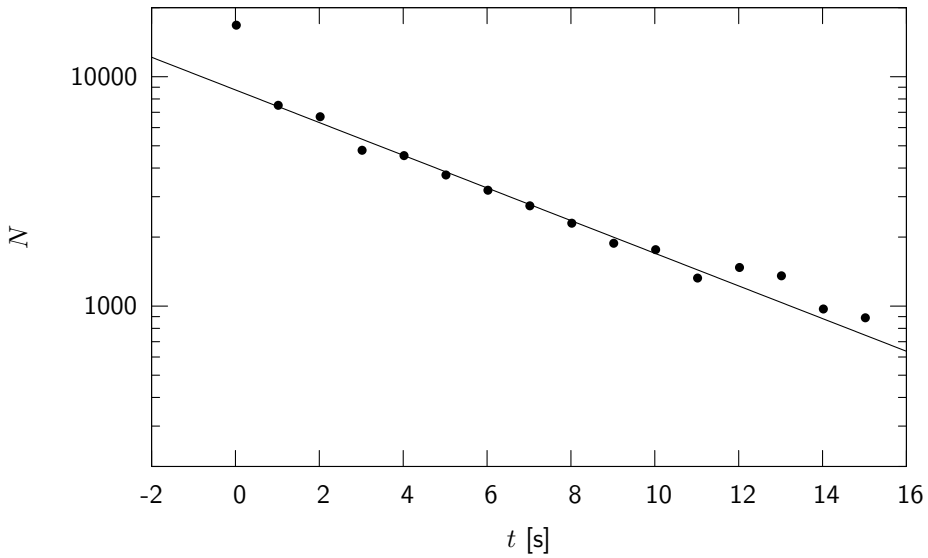

Figure 8.2: Decay of dipole trap loaded with $^1S_0$ atoms. The lifetime measurement shows a linear decay with a time constant of $\tau = 5\,\mathrm{s}$. The first data point, taken 20 ms after turning off the QUIC trap, exceeds the expected value by about a factor of two because it contains a fraction of hot atoms that has not yet left the volume that is imaged onto the CCD camera.

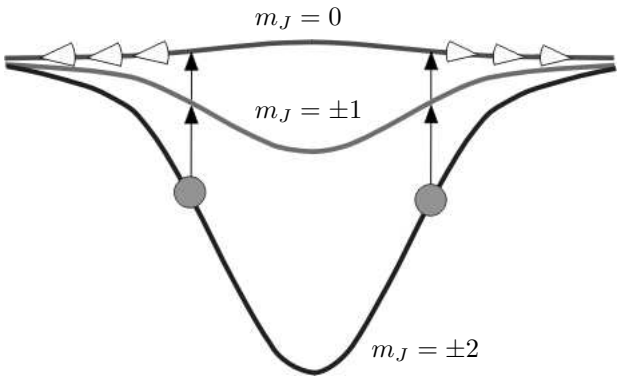

Figure 8.3: $^3P_2$ dipole trap potential (not drawn to scale). The sum of the light sifts for a π polarized trap laser results in an attractive potential for $m_J = \pm 2$ and $m_J = \pm 1$ atoms, whereas the $m_J = 0$ is not trapped. As a consequence, an evaporative cooling scheme using radio frequency might be implemented in such a trap.

moment of the atoms when switching off the Ioffe trap.

A

Magnetic Trap Specifications

A.1 Magnetic field coils

	MOT	transfer	QUIC (quadrupole)	QUIC (offset)
inner radius [mm]	36	16	5	2
outer radius [mm]	50	22	7	3
length [mm]	16	9	4	2
position (z) [mm]	±38.6	±19.9	±5.5	0
position (y) [mm]	0	33	25	29.3
windings	200	86	83	19
resistance (1 coil) at 20 °C (w/o feed cables) [Ω]	1.51	0.65	0.78	0.10
wire type	KW9	KW6	KW3	KW3

Table A.1: Magnetic field coils. For wire specifications see Table A.2. The coordinate system is outlined in Figure A.1. Values refer to the center of the coils.

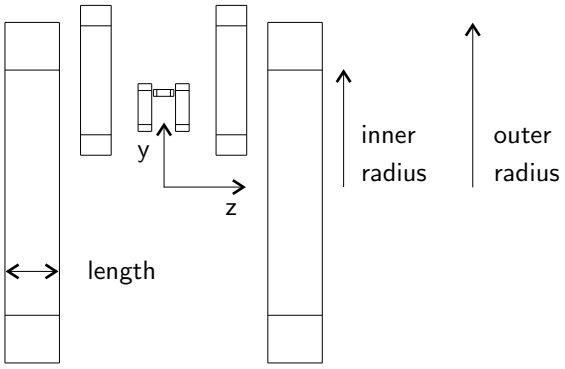

Figure A.1: Coordinate system used in connection with the coils.

	diam. copper conductor [mm]	diam. conductor and insulation [mm]	specific resistance [Ω/m]
KW9	0.91	1.10 - 1.17	0.0333
KW6	0.64	0.81 - 0.87	0.0650
KW3	0.295	0.314 - 0.331	0.175

Table A.2: Wire specifications. Wire bought at tectra GmbH. Diameters are given as specified by the company; resistances are measured values. Insulation material is polyimid (Kapton®).

trap label	I(quad) [A]	I(offset) [A]	oscillation freq. (x, y) $\omega/2\pi$ [Hz]	curvatures (x, y) a [T/m²]	offset field c [G]
dcool	1.0	2.50	89, 79	375, 275	16
ld0	0.5	0.63	107, 54	550, 140	2.6
ld1	1.0	1.15	164, 74	1280, 260	3.9
ld2	1.5	1.73	201, 90	1920, 390	5.8
ld3	2.0	2.3	232, 104	2560, 510	7.7
ld4	2.6	3.0	264, 119	3310, 670	10.2

Table A.3: Magnetic potentials of different QUIC trap settings. 1-dim Doppler cooling is performed in dcool. Measurements on elastic and inelastic collision rates are carried out in ldx. Values are obtained by simulating the current configuration with BiotSavart. The curvatures are calculated by fitting a parabola ($B(x) = ax^2 + c$) to a region of the B field around the origin with radius 0.6 mm (represents best the actual dimension of the sample). The oscillation frequencies then follow with $\omega^2 = \frac{2a\mu}{m}$. Due to the rotational symmetry of the trap, the values for the x and z directions are approximately equal.

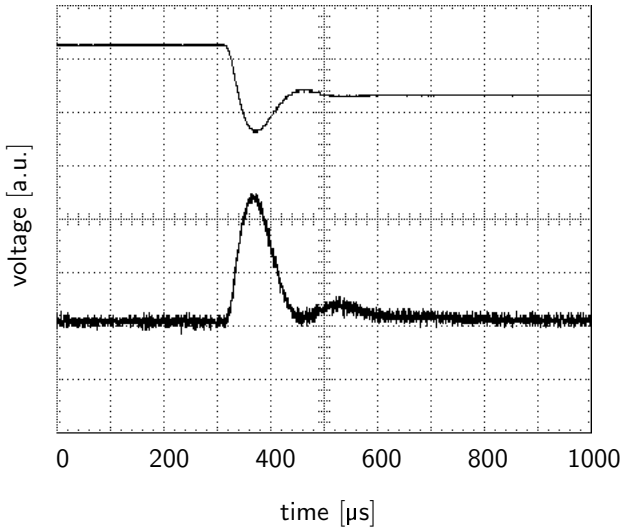

Figure A.2: QUIC trap quadrupole coils: switching time. The upper trace shows the voltage measured across one quadrupole coil of the QUIC trap while switching off the current in this coil. To measure the decay of the magnetic field, the offset coil of the QUIC trap was used as a pickup and and the induced voltage was recorded while switching off the current in the quadrupole coil (lower trace). The measurements show that the main part of the switching process takes about 150 µs and about 250 µs for the coil to be completely turned off.

	MOT	transfer	QUIC
$\frac{B'}{I}[\frac{\mathrm{G}}{\mathrm{cmA}}]$	8.34	14.9	174

Table A.4: Magnetic fields generated by the quadrupole coil pairs. Shown are the field gradients per current along the symmetry axes ("strong" axes). Values are obtained by simulating the current configuration with BiotSavart.

	I [A]	R [Ω] at 20 °C
slower coil	5.9	3.8
outcoupling coil	1.5	2.8

Table A.5: Zeeman slower operating parameters.

MOT coils	Delta Elektronika ES 030-10
transfer coils	Delta Elektronika ES 015-10
quadrupole coils (QUIC)	2 × HighFinesse BCS 6A/4V
offset coil (QUIC)	HighFinesse BCS 3A/12V

Table A.6: Power supplies used for the magnetic field coils.

A.2 Magnetic quadrupole field: oscillation frequencies

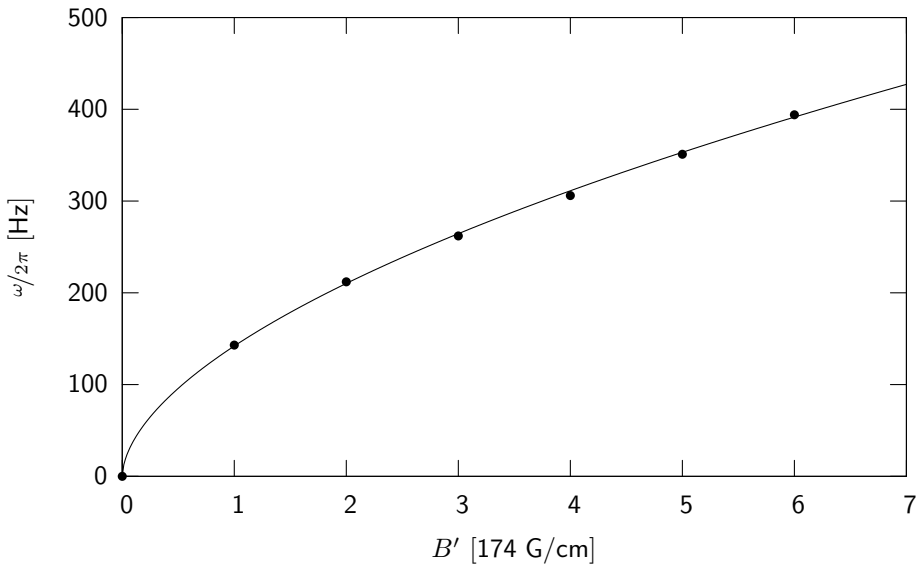

Figure A.3: Oscillation frequencies of a metastable calcium ensemble in a magnetic quadrupole trap.

Oscillation frequencies in a quadrupole potential are of interest when transferring or compressing the potential. In contrast to a harmonic potential, the frequencies cannot easily be calculated and need to be measured. The measurements were carried out in the quadrupole potential of the QUIC trap; the ensemble was displaced from the center of the trap by about 0.4 mm along the symmetry axis of the coils, which corresponds roughly to half the $1/e$ radius of the sample. The displacement was realized by applying two different currents to the quadrupole coils. Then the oscillation was started by instantly equalizing the currents and the position of the center of mass of the ensemble was monitored by absorption imaging. The oscillation frequencies were measured for 6 different field gradients (Figure A.3). A fit to the data through the origin yields an empirical value for the oscillation frequency as a function

of the magnetic field gradient:

$$\frac{\omega}{2\pi} = 142\,\mathrm{Hz} \times \left(\frac{B'}{174\,\mathrm{G/cm}}\right)^{0.566} \tag{A.1}$$

Oscillation frequencies cannot always readily be measured; one might lack the appropriate coil to excite an oscillation or the adaption of the setup for absorption imaging to a particular magnetic field setup might be too time-consuming. Here, a good estimate can be made by extrapolating the measurements using (A.1).

B

Linewidth of the $^1S_0 \rightarrow {}^3P_1$ clock transition

The atoms in the $^3P_2$ state are detected by optically pumping them to $^3P_1$ and imaging them on the ground state transition after their decay to $^1S_0$. The number of atoms that are detected in the ground state depends on the time delay between pumping to $^3P_1$ and imaging the ensemble, and, hence, the lifetime of the $^3P_1$ state is needed to calculate the number of $^3P_2$ atoms from the detected ground state population. Only very recently, the first precision measurement of the lifetime of $^3P_1$ was published. The measured value here is 425±10 µs [27]. Other previous data, derived from various experimental methods, vary considerably between the following values: 379 µs [57], 330 µs [96], 570 µs [36], 340 µs [35], 500 µs [9].

The experimental apparatus described in this thesis also makes a precision measurement of the $^3P_1$ lifetime possible. It allows convenient preparation of ensembles of $^3P_1$ atoms by optically depumping the captured $^3P_2$ atoms (either from the MOT or the magnetic trap). Since the upper (4p4p) $^3P_2$ level of the depumping transition at 430 nm decays to $^3P_1$ with a lifetime of 23 ns [57], the flux into the $^3P_1$ level abruptly terminates after applying the depumping pulse. A potential flux from the decay of the $^1D_2$ state can be prevented by waiting for some time much larger than the $^1D_2 \rightarrow {}^3P_1$ decay time of 3.3 ms [9].

Figure B.1 shows a lifetime measurement of the $^3P_1$ level. The MOT at 1978 nm was loaded for 800 ms until the light at 423 nm was shut off. After another 30 ms, a 10 µs depumping pulse was applied. The fluorescence at 657 nm was detected with a photomultiplier tube[1] and

[1] Hamamatsu R928

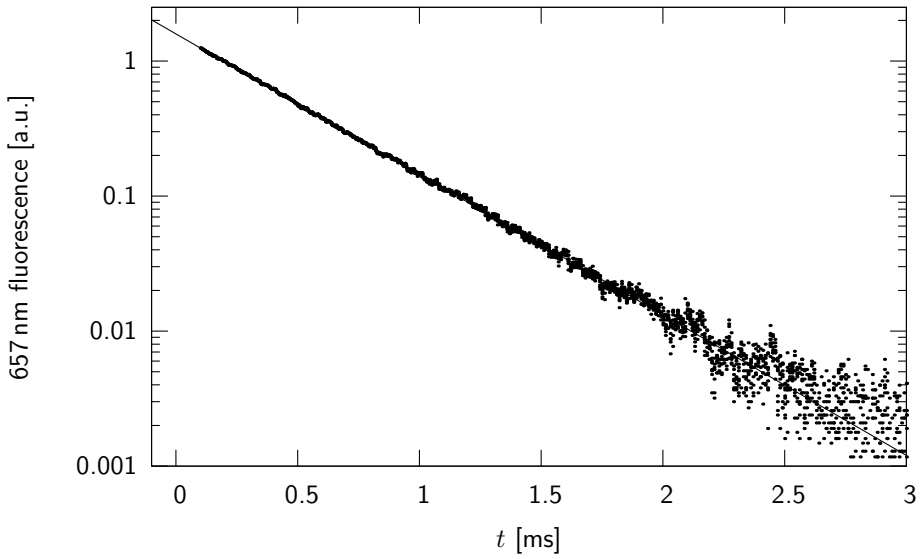

Figure B.1: Lifetime measurement of the ${}^3\mathrm{P}_1$ state.

recorded with an oscilloscope[2]. The data shown are an average over 100 measurements. For the determination of the lifetime, a total of 4900 measurements were averaged; the error given is a conservative account of the statistical uncertainties in the measurements. The lifetime is determined as

$$\tau = 417 \pm 4\,\mu\mathrm{s}.$$

The corresponding linewidth is

$$\Delta\nu = 382 \pm 4\,\mathrm{Hz}.$$

To ensure that no residual flux into the ${}^3\mathrm{P}_1$ state is considered, only the data with $t > 100\,\mu\mathrm{s}$ are evaluated (the beginning of the depumping pulse sets $t = 0$).

[2]LeCroy 400 MHz digital oscilloscope 9314C

C Correction Factors

C.1 Decay $^3\mathrm{P}_1 \rightarrow {}^1\mathrm{S}_0$: lifetime correction

When probing the population of the $^3\mathrm{P}_2$ state, the atoms are optically pumped to $^3\mathrm{P}_1$ from which they decay to the ground state where they can be detected by absorption imaging. Owing to the finite lifetime of the $^3\mathrm{P}_1$ state, the number of atoms detected in the ground state depends on the time t that is allowed between optically pumping the atoms and detecting them. The number of ground state atoms N_g is given by

$$N_g(t) = N_0(1 - e^{-t/\tau}), \tag{C.1}$$

where N_0 is the initial population of the $^3\mathrm{P}_1$ state and τ =417 µs (cf. Appendix B) is its lifetime. For all data presented in this thesis, t was set to 400 µs, hence the numbers directly observed by absorption measurement needed to be corrected by a factor of 1.62.

C.2 $1/e$ radius measurements: time of flight correction

The sample expands during the time that is allowed for optically depumping the metastable $^3\mathrm{P}_2$ atoms and detecting them in the ground state; hence the measured radii are larger than the original ones. For a thermal ensemble the velocities follow Maxwell's distribution

$$f(v)\mathrm{d}v \propto \exp\left(-\frac{mv^2}{2k_BT}\right), \tag{C.2}$$

thus a point-like ensemble that expands uniformly with $v = x/t$ exhibits a spatial distribution after some time t of

$$f(x)\mathrm{d}x \propto \exp\left(-x^2/\sigma_1^2\right), \tag{C.3}$$

with $\sigma_1^2 = 2k_BTt^2/m$. If the initial ensemble shows a Gaussian spatial density distribution with a $1/e$ radius of σ_2, then this distribution evolves according to

$$\begin{aligned} f(x)\mathrm{d}x &\propto \int \mathrm{d}x_0 \exp\left(-\frac{(x-x_0)^2}{\sigma_1^2} - \frac{x_0^2}{\sigma_2^2}\right) \\ &\propto \exp(-x^2/\sigma^2), \end{aligned} \tag{C.4}$$

with $\sigma^2 = \sigma_1^2 + \sigma_2^2$. Using (7.7) and writing the oscillation frequency ω in terms of the magnetic field curvature a, the magnetic moment μ, and the atomic mass m, the initial radius σ_2 can be calculated from the measured radius σ and the time t according to

$$\sigma_2 = \sigma\left(1 + \frac{2a\mu}{m}t^2\right)^{-\frac{1}{2}}. \tag{C.5}$$

D Software

A whole set of software is needed to run the experiment and analyze the collected data. A detailed account of the programs would be outside the scope of this thesis; this Appendix is intended to illustrate the main routines that are used in the experiment.

When running the experiment, a number of active elements in the setup has to be controlled with high precision concerning the timing. TTL signals are needed to switch the mechanical shutters and the AOMs and to provide trigger pulses for the camera and the oscilloscopes that monitor the experiment. Analog signals are needed to control the currents in the magnetic field coils and the intensity and detuning of the radio frequency that drives the AOMs. To accomplish this, we use an independent computer system[1] that is specifically designed for such a task. It consists of 32 digital I/O channels[2] and 8 analog output channels[3] that are controlled by an independent CPU (40 MHz). There is just one routine that runs on the ADwin and that sets the output voltages of the individual channels. The smallest time interval that can be used is set at 10 µs. The routine was originally written by C. Ospelkaus and was adapted to the specific hardware requirements of our ADwin. It communicates with a PC through an ethernet connection; a LabVIEW program (ExpControl.vi) on the PC is used to conveniently specify experimental sequences to be run on the ADwin.

The ExpControl.vi is a very versatile tool to control the experiment. It was originally

[1] ADwin-Pro, Processor T9, Jäger GmbH
[2] TTL output, "low" (0 V) or "high" (5 V)
[3] output range: -10 V to +10 V, 16 bit resolution

written by M. Erhard, H. Schmaljohann, and C. Ospelkaus. A number of modifications were then added to meet the specific requirements of the experiments presented here. The core functionality of the program is to let the user set arbitrary sequences that are to be executed on the ADwin. In addition, commands can be sent to GPIB devices. In an array of time slots, the user can specify the duration of the time slot in steps of 10 µs and the values of the individual digital and analog channels of the ADwin. Experimental sequences can be saved for documentation purposes and for future use.

To ease the input of the analog values, the user can modify lookup tables that translate the voltage output range of the analog channels into values relevant to the experiment like, e.g., current in the field coils or light intensity. These tables can also be used to specify non-linear ramps, e.g. for experiments that aim at reducing the ensemble temperature by adjusting the MOT parameters. The light intensity of the MOT beams can thus be ramped down in a parabolic pattern. To compensate delays in the response of, e.g., mechanical shutters, delays can be specified in the program and are automatically implemented in the timing.

An important functionality of the program is its ability to vary the value of a particular parameter (analog output voltage or duration of a time slot) in consecutive sequences. The user can specify a set of values that this parameter is to be set at. Then the routine randomly picks values from this set until all values are taken. As an example, the user could vary the time that atoms are stored in a trap before they are detected. The randomization here is important to compensate drifts (e.g. of the laser frequencies) of the setup during the measurement.

A second LabVIEW (abs_img.vi) routine is used to control the camera and store the acquired images. It is specifically adapted for acquiring absorption images of the sample according to (6.6) and (6.7). The ExpControl.vi sends three triggers to the camera to acquire the absorption, bright-field, and dark-field images. A period of 120 ms separates the trigger pulses to enable the readout of the pictures from the camera. The abs_img.vi displays all three images and the transmission image. It calculates the atom number according to (7.11), the peak density according to (6.5), and the $1/e$ radii of the sample in x and y direction. All these values are displayed immediately after the image acquisition.

The interplay of these two routines allows very convenient data acquisition. A complete set of data as needed, e.g., in trap decay measurements can be acquired, including oscilloscope traces, images of the atom cloud, and any experimental parameters that were set during the acquisition. Provided all laser systems remain in a frequency locked status, complete measurements can be recorded by starting the data acquisition and waiting until all data points are saved.

The beam transfer between the tables (cf. Section 2.4) is controlled by beam_transfer.vi. Prior to activating the stabilization, a rough adjustment of the piezo mirrors has to be done since large drifts between the tables cannot be compensated by the piezos alone. The routine lets the user select a laser beam and a piezo mirror and displays the corresponding quadrant

photodiode signal. Using the mechanical mirror mounts the beam can be aligned to hit the center of the diode. After this rough adjustment, the stabilization routine is activated.

The pressure in the vacuum chamber is monitored by a fourth routine (vacuum.vi). The two pressure gauges of the main chamber and the gauge in the fore-line part of the oven section are read out through an RS232 connection. The routine runs on a separate computer and displays the pressure vs. time diagrams of the three gauges. In addition, the pressure readings are saved (one file per day). It is important to monitor the pressure; if the coils start to heat up, the pressure in the chamber rises and some time has to be allowed for the setup to cool down again.

The data analysis of the absorption images is done by a routine (batch.vi) that allows batch processing of the acquired pictures. A set of data can be selected by the user and then analyzed by the routine. This way, a data analysis can be conveniently performed and parameters relevant to the analysis can easily be varied, like, e.g., the area in the transmission image used for the analysis. The routine extracts the following values from the absorption images: optical density D, D^2, atom number N, "center of mass" (COM) coordinates (needed for oscillation measurements), peak optical density, coordinates of peak optical density, $1/e$ radii (x and y direction), and the time stamp associated with a picture. It also recognizes and eliminates pictures that were not properly illuminated, e.g. if a laser system temporarily locked out.

A second routine (data.vi) is then used to visualize the data extracted by batch.vi and to further process the data, e.g. to extract averages of selected parameters that are then used for curve fitting.

Bibliography

[1] Gerhard Adam and Otto Hittmair, Wärmetheorie, Vieweg, Braunschweig/Wiesbaden, 1992, Kap. 8.8 Gleichgewichtsverteilung bei äußerem Kraftfeld.

[2] M. H. Anderson, J. R. Ensher, M. R. Matthews, C. E. Wieman, and E. A. Cornell, Observation of Bose-Einstein Condensation in a Dilute Atomic Vapor, Science **269** (1995), no. 0, 198.

[3] J. R. Anglin and W. Ketterle, Bose-Einstein condensation of atomic gases, Nature **416** (2002), 211.

[4] M. Arndt, M. Ben Dahan, D. Guéry-Odelin, M. W. Reynolds, and J. Dalibard, Observation of a Zero-Energy Resonance in Cs-Cs Collisions, Phys. Rev. Lett. **79** (1997), no. 4, 625.

[5] A. Ashkin, Atomic-Beam Deflection by Resonance-Radiation Pressure, Phys. Rev. Lett. **25** (1970), 1321.

[6] A. Aspect, Manipulation of neutral atoms. Experiments, Phys. Rep. **219** (1992), no. 3-6, 141.

[7] T. Bergeman, Gidon Erez, and Harold Metcalf, Magnetostatic trapping fields for neutral atoms, Phys. Rev. A **35** (1987), no. 4, 1535.

[8] T. H. Bergeman, Patrick McNicholl, Jan Kyacia, Harold Metcalf, and N. Balazs, Quantized motion of atoms in a quadrupole magnetostatic trap, J. Opt. Soc. Am. B **6** (1989), no. 11, 2249.

[9] N. Beverini, F. Giammanco, E. Maccioni, F. Strumia, and G. Vissani, Measurement of the calcium $^1P_1$-$^1D_2$ transition rate in a laser-cooled atomic beam, J. Opt. Soc. Am. B **6** (1989), no. 11, 2188.

[10] N. Beverini, E. Maccioni, and F. Strumia, g_J Factor of neutral calcium ^3P metastable levels, J. Opt. Soc. Am. B **15** (1998), no. 8, 2206.

[11] G. C. Bjorklund, M. D. Levenson, W. Lenth, and C. Ortiz, Frequency Modulation (FM) Spectroscopy: Theory of Lineshapes and Signal-to-Noise Analysis, Appl. Phys. B **32** (1983), 145.

[12] Eric D. Black, An introduction to Pound-Drever-Hall laser frequency stabilization, Am. J. Phys. **69** (1995), 79.

[13] Satyendra Bose, Plancks Gesetz und Lichtquantenhypothese, Z. Phys. **26** (1924), no. 3, 178.

[14] K. Brugger, P. Krger, X. Luo, S. Wildermuth, H. Gimpel, M. W. Klein, S. Groth, R. Folman, I. Bar-Joseph, and J. Schmiedmayer, Two-wire guides and traps with vertical bias fields on atom chips, Phys. Rev. A **72** (2005), 023607.

[15] Volker Burgarth, Ein Michelson-Lambdameter und eine Frequenzmarke für hochpräzise Wellenlängenmessungen, Master's thesis, University of Hamburg, 1998.

[16] Keith Burnett, Paul S. Julienne, Paul D. Lett, Eite Tiesinga, and Carl J. Williams, Quantum encounters of the cold kind, Nature **416** (2002), 225.

[17] Steven Chu, The manipulation of neutral particles, Rev. Mod. Phys. **70** (1998), no. 3, 685.

[18] Steven Chu, J. E. Bjorkholm, A. Ashkin, and A. Cable, Experimental Observation of Optically Trapped Atoms, Phys. Rev. Lett. **57** (1986), no. 3, 314.

[19] Steven Chu, L. Hollberg, J. E. Bjorkholm, Alex Cable, and A. Ashkin, Three-Dimensional Viscous Confinement and Cooling of Atoms by Resonance Radiation Pressure, Phys. Rev. Lett. **55** (1985), no. 1, 48.

[20] C. Cohen-Tannoudji, Laser cooling and trapping of neutral atoms: theory, Phys. Rep. **219** (1992), no. 3-6, 153.

[21] C. Cohen-Tannoudji and W.D. Phillips, New Mechanisms for Laser Cooling, Phys. Today **43** (1990), 33.

[22] C. N. Cohen-Tannoudji and W. D. Phillips, New Mechanisms for Laser Cooling, Phys. Today **43** (1990), no. 10, 33.

[23] Claude N. Cohen-Tannoudji, Manipulating atoms with photons, Rev. Mod. Phys. **70** (1998), no. 3, 707.

[24] J. Dalibard and C. Cohen-Tannoudji, Laser cooling below the Doppler limit by polarization gradients: simple theoretical-models, J. Opt. Soc. Am. B **6** (1989), no. 11, 2023.

[25] K. B. Davis, M.-O. Mewes, M. R. Andrews, N. J. van Druten, D. S. Durfee, D. M. Kurn, and W. Ketterle, Bose-Einstein Condensation in a Gas of Sodium Atoms, Phys. Rev. Lett. **75** (1995), no. 22, 3969.

[26] Kendall B. Davis, Marc-Oliver Mewes, Michael A. Joffe, Michael R. Andrews, and Wolfgang Ketterle, Evaporative Cooling of Sodium Atoms, Phys. Rev. Lett. **74** (1995), no. 26, 5202.

[27] Carsten Degenhardt, Hardo Stoehr, Christian Lisdat, Guido Wilpers, Harald Schnatz, Burghard Lipphardt, Tatiana Nazarova, Paul-Eric Pottie, Uwe Sterr, Jürgen Helmcke, and Fritz Riehle, Calcium optical frequency standard with ultracold atoms: Approaching 10^{-15} relative uncertainty, Phys. Rev. A **72** (2005), 062111.

[28] B. DeMarco and D. S. Jin, Onset of Fermi Degeneracy in a Trapped Atomic Gas, Science **285** (1999), no. 5434, 1703.

[29] Wolfgang Demtröder, Laser Spectroscopy, Springer, Berlin/Heidelberg/New York, 2003.

[30] Andrei Derevianko, Sergey G. Porsev, Svetlana Kotochigova, Eite Tiesinga, and Paul S. Julienne, Ultracold Collision Properties of Metastable Alkaline-Earth Atoms, Phys. Rev. Lett. **90** (2003), no. 6, 063002.

[31] S. A. Diddams, J. C. Bergquist, S. R. Jefferts, and C. W. Oates, Standards of Time and Frequency at the Outset of the 21st Century, Science **306** (2004), 1318.

[32] Optical dipole traps for neutral atoms, R. Grimm and M. Weidemller and Yu. B. Ovchinnikov, Adv. At. Mol. Opt. Phys.42, 95-170 (2000) **42** (2000), 95.

[33] J. Doyle, B. Friedrich, R. V. Krems, and F. Masnou-Seeuws, Editorial: Quo vadis, cold molecules?, Eur. Phys. J. D **31** (2004), no. 2, 149, See also following articles in this issue.

[34] R. W. P. Drever, J. L. Hall, F. V. Kowalski, J. Hough, G. M. Ford, A. J. Munley, and H. Ward, Laser Phase and Frequency Stabilization Using an Optical Resonator, Appl. Phys. B **31** (1983), 97.

[35] R. Drozdowski, M. Ignaciuk, J. Kwela, and J. Heldt, Radiative lifetimes of the lowest $^3P_1$ metastable states of Ca and Sr, Z. Phys. D: At., Mol. Clusters **41** (1997), no. 2, 125.

[36] R. Drozdowski, J. Kwela, and M. Walkiewicz, Lifetimes of the 4s4p ^{3}P$_1$ and 4s3d ^{1}D$_2$ states of Ca I, Z. Phys. D: At., Mol. Clusters **27** (1993), no. 4, 321.

[37] A. Einstein, Quantentheorie des einatomigen idealen Gases. Zweite Abhandlung, Sitzungber. Preuss. Akad. Wiss. **1925** (1925), 3.

[38] Tilman Esslinger, Immanuel Bloch, and Theodor W. Hänsch, Bose-Einstein condensation in a quadrupole-Ioffe-configuration trap, Phys. Rev. A **58** (1998), no. 4, R2664.

[39] Y. V. Gott, M. S. Ioffe, and V. G. Telkovsky, Some new results on confining of plasmas in a magnetic trap (in Russian), Nuclear Fusion, Proceedings of the Conference on Plasma Physics and Controlled Nuclear Fusion Research, 1961, International Atomic Energy Agency, Vienna, 1962, p. 1045.

[40] M. Greiner, C. A. Regal, and D. S. Jin, Probing the excitation spectrum of a Fermi gas in the BCS-BEC crossover regime, Phys. Rev. Lett. **94** (2005), 070403.

[41] Markus Greiner, Immanuel Bloch, Theodor W. Hänsch, and Tilman Esslinger, Magnetic transport of trapped cold atoms over a large distance, Phys. Rev. A **63** (2001), 031401(R).

[42] Markus Greiner, Olaf Mandel, Tilman Esslinger, Theodor W. Hänsch, and Immanuel Bloch, Quantum phase transition from a superfluid to a Mott insulator in a gas of ultracold atoms, Nature **415** (2002), 39.

[43] A. Griesmaier, J. Werner, S. Hensler, J. Stuhler, and T. Pfau, Bose-Einstein Condensation of Chromium, Phys. Rev. Lett. **94** (2005), 160401.

[44] J. Grünert, G. Quehl, V. Elman, and A. Hemmerich, Ultracold metastable calcium ensembles, a medium for matter wave amplification?, J. Mod. Opt. **47** (2000), no. 14/15, 2733.

[45] Jan Grünert, Ultracold metastable calcium atoms in a bichromatic magneto-optical trap, Ph.D. thesis, University of Hamburg, 2002.

[46] Jan Grünert and Andreas Hemmerich, Optimizing the production of metastable calcium atoms in a magneto-optical trap, Appl. Phys. B **73** (2001), 815.

[47] Jan Grünert and Andreas Hemmerich, Sub-Doppler magneto-optical trap for calcium, Phys. Rev. A **65** (2002), 041401(R).

[48] J. L. Hall and S. A. Lee, Interferometric real-time display of cw dye laser wavelength with sub-Doppler accuracy, Appl. Phys. Lett. **29** (1976), no. 6, 367.

[49] T. W. Hänsch and A. L. Schawlow, Cooling of Gases by Laser Radiation, Opt. Commun. **13** (1975), no. 1, 68.

[50] D. P. Hansen, J. R. Mohr, and Andreas Hemmerich, Magnetic trapping of metastable calcium atoms, Phys. Rev. A **67** (2003), 021401(R).

[51] Dirk Hansen and Andreas Hemmerich, Doppler-free spectroscopy of metastable calcium in a discharge heat pipe, Phys. Rev. A **72** (2005), 022502.

[52] S. Hensler, J. Werner, A. Griesmaier, P.O. Schmidt, A. Grlitz, T. Pfau, S. Giovanazzi, and K. Rzazewski, Dipolar relaxation in an ultra-cold gas of magnetically trapped chromium atoms, Appl. Phys. B **77** (2003), no. 8, 765.

[53] S. A. Hopkins, S. Webster, J. Arlt, P. Bance, S. Cornish, O. Maragò, and C. J. Foot, Measurement of elastic cross section for cold cesium collisions, Phys. Rev. A **61** (2000), 032707.

[54] G. M. Kavoulakis, C. J. Pethick, and H. Smith, Collisional relaxation in diffuse clouds of trapped bosons, Phys. Rev. A **61** (2000), 053603.

[55] W. Ketterle, D. S. Durfee, and D. M. Stamper-Kurn, Making, probing and understanding Bose-Einstein condensates, Proceedings of the International School of Physics - Enrico Fermi (M. Inguscio, S. Stringari, and C. E. Wieman, eds.), IOS Press, 1999, p. 67.

[56] Viatcheslav Kokoouline, Robin Santra, and Chris H. Greene, Multichannel Cold Collisions between Metastable Sr Atoms, Phys. Rev. Lett. **90** (2003), no. 25, 253201, Paper presents results on Sr; parameters for Ca: private communication.

[57] R.L. Kurucz and B. Bell, 1995 Atomic Line Data, CD–ROM No. **23**, Smithsonian Astrophysical Observatory, Cambridge, Mass., 1995, http://cfa-www.harvard.edu/amdata/ampdata/kurucz23/sekur.html.

[58] Paul D. Lett, Richard N. Watts, Christoph I. Westbrook, William D. Phillips, Phillip L. Gould, and Harold J. Metcalf, Observation of Atoms Laser Cooled below the Doppler Limit, Phys. Rev. Lett. **61** (1988), no. 2, 169.

[59] T. Loftus, J. R. Bochinski, and T. W. Mossberg, Magnetic trapping of ytterbium and the alkaline-earth metals, Phys. Rev. A **66** (2002), 013411.

[60] Andrew D. Ludlow, Martin M. Boyd, Tanya Zelevinsky, Seth M. Foreman, Sebastian Blatt, Mark Notcutt, Tetsuya Ido, and Jun Ye, Systematic Study of the ^{87}Sr Clock Transition in an Optical Lattice, Phys. Rev. Lett. **96** (2006), 033003.

[61] Ettore Majorana, Atomi orientati in campo magnetico variabile, Nuovo Cimento **9** (1932), no. 2, 43.

[62] M. R. Matthews, B. P. Anderson, P. C. Haljan, D. S. Hall, C. E. Wieman, and E. A. Cornell, Vortices in a Bose-Einstein Condensate, Phys. Rev. Lett. **83** (1999), no. 13, 2498.

[63] Harold J. Metcalf and Peter van der Straten, Laser Cooling and Trapping, Springer, New York/Berlin/Heidelberg, 1999.

[64] M.-O. Mewes, M. R. Andrews, N. J. van Druten, D. M. Kurn, D. S. Durfee, and W. Ketterle, Bose-Einstein Condensation in a Tightly Confining dc Magnetic Trap, Phys. Rev. Lett. **77** (1996), no. 3, 416.

[65] Alan L. Migdall, John V. Prodan, William D. Phillips, Thomas H. Bergeman, and Harold J. Metcalf, First Observation of Magnetically Trapped Neutral Atoms, Phys. Rev. Lett. **54** (1985), no. 24, 2596.

[66] J. Mitroy and M. W. J. Bromley, Properties of the triplet metastable states of the alkaline-earth-metal atoms, Phys. Rev. A **70** (2004), 052503.

[67] C. R. Monroe, E. A. Cornell, C. A. Sackett, C. J. Myatt, and C. E. Wieman, Measurement of Cs-Cs Elastic Scattering at $T = 30\mu$K, Phys. Rev. Lett. **70** (1993), no. 4, 414.

[68] C. J. Myatt, E. A. Burt, R. W. Ghrist, E. A. Cornell, and C. E. Wieman, Production of Two Overlapping Bose-Einstein Condensates by Sympathetic Cooling, Phys. Rev. Lett. **78** (1997), no. 4, 586.

[69] W. Neuhauser, M. Hohenstatt, P. Toschek, and H. Dehmelt, Optical-Sideband Cooling of Visible Atom Cloud Confined in Parabolic Well, Phys. Rev. Lett. **41** (1978), no. 4, 233.

[70] A. Noble and M. Kasevich, UHV optical window seal to conflat knife edge, Rev. Sci. Instrum. **65** (1994), no. 9, 3042.

[71] C. W. Oates, G. Wilpers, and L. Hollberg, Observation of large atomic-recoil-induced asymmetries in cold atom spectroscopy, Phys. Rev. A **71** (2005), 023404.

[72] Wolfgang Petrich, Michael H. Anderson, Jason R. Ensher, and Eric A. Cornell, Stable, Tightly Confining Magnetic Trap for Evaporative Cooling of Neutral Atoms, Phys. Rev. Lett. **74** (1995), no. 17, 3352.

[73] William D. Phillips, Laser cooling and trapping of neutral atoms, Rev. Mod. Phys. **70** (1998), no. 3, 721.

[74] J. Piilo, E. Lundh, and K.-A. Suominen, Radiative collisional heating at the Doppler limit for laser-cooled magnesium atoms, Phys. Rev. A **70** (2004), 013410.

[75] E. S. Polzik and H. J. Kimble, Frequency doubling with $KBNbO_3$ in an external cavity, Optics Lett. **16** (1991), no. 18, 1400.

[76] R. V. Pound, Electronic Frequency Stabilization of Microwave Resonators, Rev. Sci. Instrum. **17** (1946), no. 11, 490.

[77] David E. Pritchard, Cooling Neutral Atoms in a Magnetic Trap for Precision Spectroscopy, Phys. Rev. Lett. **51** (1983), no. 15, 1336.

[78] G. Quehl, J. Grünert, V. Elman, and A. Hemmerich, A Tunable Dual Frequency Tm:YAG Laser, Opt. Commun. **190** (2001), 303.

[79] E. L. Raab, M. Prentiss, Alex Cable, Steven Chu, and D. E. Pritchard, Trapping of Neutral Sodium Atoms with Radiation Pressure, Phys. Rev. Lett. **59** (1987), no. 23, 2631.

[80] I. I. Rabi, On the Process of Space Quantization, Phys. Rev. **49** (1936), 324.

[81] J. Reichel, Microchip traps and Bose-Einstein condensation, Apppl. Phys. B **74** (2002), no. 6, 469.

[82] L. Ricci, M. Weidemller, T. Esslinger, A. Hemmerich, C. Zimmermann, V. Vuletic, W. Knig, and T. W. Hänsch, A compact grating-stabilized diode laser system for atomic physics, Optics Commun. **117** (1995), no. 5-6, 541.

[83] Robin Santra and Chris H. Greene, Tensorial analysis of the long-range interaction between metastable alkaline-earth-metal atoms, Phys. Rev. A **67** (2003), 062713.

[84] Julian Schwinger, On Nonadiabatic Processes in Inhomogeneous Fields, Phys. Rev. **51** (1937), 648.

[85] J. Söding, D. Guéry-Odelin, P. Desbiolles, G. Ferrari, and J. Dalibard, Giant Spin Relaxation of an Ultracold Cesium Gas, Phys. Rev. Lett. **80** (1998), no. 9, 1869.

[86] P. Spoden, M. Zinner, N. Herschbach, W. J. van Drunen, W. Ertmer, and G. Birkl, Collisional Properties of Cold Spin-Polarized Metastable Neon Atoms, Phys. Rev. Lett. **94** (2005), 223201.

[87] R. J. C. Spreeuw, T. Pfau, U. Janicke, and M. Wilkens, Laser-like Scheme for Atomic-Matter Waves, Europhys. Lett. **32** (1995), no. 6, 469.

[88] J. Stuhler, A. Griesmaier, T. Koch, M. Fattori, T. Pfau, S. Giovanazzi, P. Pedri, and L. Santos, Observation of Dipole-Dipole Interaction in a Degenerate Quantum Gas, Phys. Rev. Lett. **95** (2005), 150406.

[89] Masao Takamoto and Hidetoshi Katori, Spectroscopy of the $^1S_0$ - $^3P_0$ Clock Transition of ^{87}Sr in an Optical Lattice, Phys. Rev. Lett. **91** (2003), no. 22, 223001.

[90] Yosuke Takasu, Kenichi Maki, Kaduki Komori, Tetsushi Takano, Kazuhito Honda, Mitsutaka Kumakura, Tsutomu Yabuzaki, and Yoshiro Takahashi, Spin-Singlet Bose-Einstein Condensation of Two-Electron Atoms, Phys. Rev. Lett. **91** (2003), no. 4, 040404.

[91] A. M. Thomas, S. Hopkins, S. L. Cornish, and C. J. Foot, Strong evaporative cooling towards Bose-Einstein condensation of a magnetically trapped caesium gas, J. Opt. B **5** (2003), 107.

[92] C. G. Townsend, N. H. Edwards, C. J. Cooper, K. P. Zetie, C. J. Foot, A. M. Steane, P. Szriftgiser, H. Perrin, and J. Dalibard, Phase-space density in the magneto-optical trap, Phys. Rev. A **52** (1995), no. 2, 1423.

[93] Th. Udem, S. A. Diddams, K. R. Vogel, C. W. Oates, E. A. Curtis, W. D. Lee, W. M. Itano, R. E. Drullinger, J. C. Bergquist, and L. Hollberg, Absolute Frequency Measurements of the Hg^+ and Ca Optical Clock Transitions with a Femtosecond Laser, Phys. Rev. Lett. **86** (2001), no. 22, 4996.

[94] Th. Udem, R. Holzwarth, and T.W. Hänsch, Optical frequency metrology, Nature **416** (2002), 233.

[95] Tino Weber, Jens Herbig, Michael Mark, Hanns-Christoph Nägerl, and Rudolf Grimm, Bose-Einstein Condensation of Cesium, Science **299** (2003), 232.

[96] P. G. Whitkop and J. R. Wiesenfeld, Collisional deactivation Of Ca(4p ^3P_J) by barium atoms, Chem. Phys. Lett. **69** (1980), no. 3, 457.

[97] C. Wieman and T. W. Hänsch, Doppler-Free Laser Polarization Spectroscopy, Phys. Rev. Lett. **36** (1976), 1170.

[98] D. Wineland and H. Dehmelt, Proposed 10^{14} $\Delta\nu < \nu$ Laser Fluorescence Spectroscopy on Tl^+ Mono-Ion Oscillator III, Bull. Am. Phys. Soc. **20** (1975), 637.

[99] D. J. Wineland, R. E. Drullinger, and F. L. Walls, Radiation-Pressure Cooling of Bound-Resonant Absorbers, Phys. Rev. Lett. **40** (1978), no. 25, 1639.

[100] Max Wutz, Hermann Adam, Wilhelm Walcher, and Karl Jousten, Handbuch Vakuumtechnik, Vieweg, Braunschweig/Wiesbaden, 2000.

[101] C. Zimmermann, V. Vuletic, A. Hemmerich, L. Ricci, and T. W. Hänsch, Design for a compact tunable Ti:sapphire laser, Optics Letters **20** (1995), no. 3, 297.

Publications

- **Observation of Multi-channel Collisions of Cold Metastable Calcium Atoms**
  Dirk Hansen and Andreas Hemmerich
  Phys. Rev. Lett. 96, 073003 (2006)

  The main results of this Ph.D. work are published here. Inelastic and elastic collision rates of metastable calcium atoms in a magnetic trap are presented and compared to theory.

- **Doppler-free spectroscopy of metastable calcium in a discharge heat pipe**
  Dirk Hansen and Andreas Hemmerich
  Phys. Rev. A 72, 022502 (2005)

  This paper describes the spectroscopy of metastable calcium atoms with light at 430 nm and 1978 nm. Doppler-free frequency modulation and polarization spectroscopy resolve resonances of a few 10 MHz bandwidth that are well suited for laser frequency stabilization.

- **Magnetic trapping of metastable calcium atoms**
  D.P. Hansen, J.R. Mohr, and A. Hemmerich
  Phys. Rev. A 67, 021401(R) (2003)

  In this paper, the fist experiments on magnetic trapping of metastable calcium atoms are described. All experiments were conducted with the old apparatus before moving to the new lab.

Acknowledgement

Working on an experiment in laser cooling and quantum optics is an endeavor which cannot be pursued all by oneself and the experiments conducted during the course of my doctorate work were only made possible with the help and contributions of a great many people. Foremost, I wish to thank my thesis advisor Prof. Andreas Hemmerich for his commitment to the experiment. His support and enthusiasm for physics were a main factor in the success of this project. I shared the peculiarities of cold calcium atoms and many hours in the lab with our postdoc Dr. Ciprian Zafiu and fellow Ph.D. student Janis Mohr, whom I wish good luck for writing up his thesis. Dr. Jan Grünert built a first version of the apparatus back in the old facilities of the ILP and never grew tired explaining to me all the finer details of cooling and trapping calcium atoms when I had just started. I am also very grateful to the guys working on the rubidium experiments in our group. Dr. Thilo Elsässer, Dr. Boris Nagorny, Hendrik Richter, Stephan Ritter, Julian Klinner, Malik Lindholdt, Dr. Vladimir Elman, Kai Jentson, and Arne Wickenbrock helped creating a great environment by being fun people and interested physicists. I enjoyed the time as a member of the Institute of Laser Physics; working in state of the art facilities among a larger body of dedicated people was a great experience. For doing a great job in machining numerous parts for the setup, my thank goes to Frank Jonas and Stephan Fleig and their co-workers. Silke Frömmig, Victoria Romano, Reinhard Mielk, Stephan Garbers, and Ralf Lühr helped to keep the institute running. Dieter Barlösius did excellent work in making the glass cells used for spectroscopy. For his help and patience answering my questions about electronics, I would like to thank Horst Biedermann. For proof-reading individual chapters of this thesis I wish to thank Alexander Braun, Julian Klinner, Dr. Thilo Elsässer, and Dr. Ciprian Zafiu. I am very grateful to the optics division at the Physikalisch-Technische Bundesanstalt for sharing their knowledge with me how to built high quality optical viewports. It's an honor that Prof. Riehle and Prof. Neuhauser agreed to referee my thesis and defence. Finally, I am most grateful to my parents for their love and support over all these years.